Extended treatment of the surface in adatom simulations

Studies of Yu-Shiba-Rusinov band dispersion, field-emission resonances and coherent manipulation of atomic magnets

Broekhoven, R.

Important note
To cite this publication, please use the final published version (if applicable).
Please check the document version above.

EXTENDED TREATMENT OF THE SURFACE IN ADATOM SIMULATIONS

STUDIES OF YU-SHIBA-RUSINOV BAND DISPERSION,
FIELD-EMISSION RESONANCES AND COHERENT MANIPULATION
OF ATOMIC MAGNETS

RIK BROEKHOVEN

EXTENDED TREATMENT OF THE SURFACE IN ADATOM SIMULATIONS

STUDIES OF YU-SHIBA-RUSINOV BAND DISPERSION, FIELD-EMISSION RESONANCES AND COHERENT MANIPULATION OF ATOMIC MAGNETS

EXTENDED TREATMENT OF THE SURFACE IN ADATOM SIMULATIONS

STUDIES OF YU-SHIBA-RUSINOV BAND DISPERSION, FIELD-EMISSION RESONANCES AND COHERENT MANIPULATION OF ATOMIC MAGNETS

Dissertation

for the purpose of obtaining the degree of doctor
at Delft University of Technology
by the authority of the Rector Magnificus prof. dr. ir. T.H.J.J. van der Hagen,
chair of the Board for Doctorates,
to be defended publicly on Wednesday 1 October 2025 at 10:00 o'clock

by

Rik BROEKHOVEN

Master of Science in Applied Physics, Delft University of Technology, The Netherlands
born in Oosterhout (NB), The Netherlands

This dissertation has been approved by the promotors.

Composition of the doctoral committee:

Rector Magnificus,	Chairperson
Prof.dr. A. F. Otte	Delft University of Technology, *promotor*
Dr. A. R. Akhmerov	Delft University of Technology, *promotor*
Dr. M. T. Wimmer	Delft University of Technology, *promotor*

Independent members:

Dr. J. Fernández-Rossier	International Iberian Nanotechnology Laboratory, Portugal
Dr. S. H. Phark	Seoul centre for Quantum Nanoscience, South Korea
Prof.dr. Z. Zanolli	Utrecht University
Prof.dr. Y. M. Blanter	Delft University of Technology
Prof.dr. T. van der Sar	Delft University of Technology, *reserve member*

An electronic copy of this dissertation is available at
https://repository.tudelft.nl/

CONTENTS

SUMMARY

With a scanning tunneling microscope (STM) it is possible to study single atoms, the building blocks of all materials, and structures that are build from these single atoms. For STM measurements, these atoms, though, must in general always reside on a conducting surface which affects them. This thesis is about the influence of a metal surface on measurements of various atomic structures. We present models for three specific systems. These models give insights in the limitations of STM measurements and how to possibly overcome them.

Chapter 3 is about chains of magnetic atoms on a superconductor. Here, the metal surface causes electron states to be possible that are bound in between the magnetic atoms and the superconductor. They are called Yu-Shiba-Rusinov (YSR) states. They can hybridize to form a bandstructure. We present a new method to evaluate this bandstructure based on the theory of short junctions. With this method we can compute the effective Hamiltonian of a YSR chain, from which we can find how the bandstructure changes when we change parameters of the chain like its magnetism. We only require the surface self-energy at the Fermi level as an input. We test out method by comparing it with an exact calculation and show, subsequently, with an atomistic spin-orbit coupling model that the YSR bandstructures inherits features from the Fermi surface of the metal surface.

Chapter 4 is about electrons trapped in chlorine vacancies on top of copper nitride that are further confined by the STM tip. They are called field emission resonances (FER's) and behave like artificial atoms. Measurements of the conductance differential spectra for various sizes of vacancies show a negative differential resistance. We model the system and show that the negative differential resistance originates from interaction with the copper metal surface. We model the copper with density functional theory based on plane waves.

Chapters 5 and 6 are about titanium spins on silver metal surfaces decoupled by a layer of magnesium oxide. Specifically, theses chapters are about the quantum coherence these spins can have. In chapter 5 we demonstrate how to initiate coherent flip-flop interaction between the titanium electron spin and its nucleus spin. We use the STM tip magnetic field to tune the spins and confirm this with electron spin resonance. Subsequently, we apply a DC voltage to the electron spin which polarizes both spins through spin-pumping and initiates the coherent flip-flop interaction. This interaction decreases over time as the titanium atom is constantly interaction as well with free electrons from the metal surface. We model this decoherence as well as the spin pumping and show that the models match the measurements.

Chapter 6 concerns the question whether it is possible to entangle two titanium electron spins and particularly how to detect this entanglement. This is a challenge to do with a STM as it is in general only able to probe a single spin at the same time. We present a method to entangle two spins further away from the STM tip and subsequently project

this state on a third spin that is directly underneath the STM tip and we are thus able to read out. We show that a STM operating at sufficiently low temperature should be able to perform this measurement protocol despite of the decoherence due to electrons of the underlying metal.

Finally, in chapter 7 we look ahead what kind of experiments would be in the near future for each of these systems. Here, we pay specific attention to chains of titanium spins and initiate the discussion on how the quantum decoherence time of an induced flip-flop interaction in these chains decreases with chain length.

SAMENVATTING

Met een scannende tunnel microscoop (STM) kunnen we enkele atomen bestuderen, de bouwblokken van materialen, en structuren die uit deze atomen zijn opgebouwd. Voor deze metingen bevinden de atomen zich echter altijd op een geleidende ondergrond welke de atomen beinvloedt. Dit proefschrift gaat over de invloed van een metalen ondergrond op metingen van verschillende atoomstructuren binnen een scannende tunnel microscoop. Voor een drietal specifieke systemen presenteren we modellen hoe de invloed van de metalen ondergrond te bepalen. Deze modellen geven inzicht in de limitaties van de metingen en potentieel in hoe deze op te rekken.

Hoofdstuk 3 gaat over kettingen van magnetische atomen op een supergeleidend metaal. Hier heeft de metalen ondergrond het effect dat er elektronische toestanden mogelijk zijn die gebonden zijn tussen de magnetische atomen en de supergeleider. Deze worden Yu-Shiba-Rusinov toestanden (YSR) genoemd. Ze kunnen onderling met elkaar koppelen en zo een bandstructuur opmaken. Wij presenteren een nieuwe manier om deze bandstructuur te bepalen die gebaseerd is op de theorie van korte juncties. Door middel van deze methode kunnen we de effectieve Hamiltoniaan van een YSR ketting bepalen, welke direct laat zien hoe de bandstructuur verandert wanneer we de eigenschappen van de ketting zoals zijn magnetisme veranderen. Hier is slechts de zelf-energie van het metalen oppervlak voor nodig op het Fermi niveau. We tonen aan dat onze methode werkt door het te vergelijken met een exacte berekening en laten vervolgens met een spin-baan koppeling model zien dat de YSR bandstructuur de eigenschappen overneemt van het Fermi oppervlak.

Hoofdstuk 4 gaat over elektronen die gevangen zijn in gaten in een chloor rooster op kopernitride en het uiteinde van de STM punt. Deze worden veld emissie resonanties genoemd en gedragen zich als atomen. Metingen van de geleidings differentie spectra van verschillende grootte van de gaten laten een negatieve differentiele weerstand zien. We stellen een model op voor deze elektronen en tonen aan dat de negatieve differentiele weerstand komt door de interactie met de metalen ondergrond. Hiertoe modeleren we het koper van het kopernitride door middel van dichtheidsfunctionaaltheorie gebaseerd op staande golven.

Hoofdstukken 5 en 6 gaan over titanium spins op een zilver metalen ondergrond ontkoppelt door een laag magnesium oxide. Speciek gaan ze over de quantum coherentie die deze spins kunnen hebben. Hoofdstuk 5 gaat over hoe de coherente flip-flop interactie tussen de elektronspin van titanium en de kernspin tot stand te brengen en te meten. We gebruiken het magnetische veld van de STM punt om de spins te synchroniseren via elektron spin resonantie en passen vervolgens een DC voltage toe welke de spins polariseert en zo de coherente flip-flop interactie initialiseert. Deze interactie neemt af over tijd doordat het titanium atoom ook voortdurend interactie heeft met elektronen van de metalen ondergrond. We modeleren dit zowel het verval van de flip-flop interaction als het initialisitie proces voor de flip-flop interactie en laten zien dat dit overeenkomt

met de metingen.

Hoofdstuk 6 gaat over de vraag of het mogelijk is om titantium elektron spins met elkaar te kwantum verstrengelen en vooral over hoe onomwonden vast te stellen dat dit is gelukt. Dit is een uitdaging omdat de STM is gelimiteerd doordat deze doorgaans maar een spin tegelijk kan meten. Wij presenteren een methode om twee spins verder weg van de STM punt met elkaar te verstrengelen en deze vervolgens te projecteren op een derde spin die zich recht onder de STM punt bevindt en dus uit te lezen is. We laten zien dat een STM die op voldoende lage temperatuur opereert deze meting zou moeten kunnen volbrengen ondanks de interactie met elektronen van het onderliggende metaal.

In het laatste hoofdstuk 7 kijken we naar studies die voor ieder van deze drie systemen in het vooruitzicht liggen. We besteden speciale aandacht aan spin kettingen van titanium atomen en maken een begin met het beantwoorden van de vraag hoe de quantum decoherentie tijd afneemt met de lengte van de ketting wanneer we een flip-flop interactie initialezeren door middel van een DC puls.

1

INTRODUCTION

1

1.1. PREFACE

By now, we have such a great understanding of nature and its underlying forces around us that we have been able to develop technologies for skyscrapers, airplanes, and smartphones. We often forget to realize what an enormous achievement this is. Yet, still zooming in and out to the smallest and biggest scales, nature holds some of its mysteries.

One of the reasons mysteries remain at the smallest scales is that a lot is happening at these scales. A single gram of any material contains over a billion billion particles, which all have complex interactions to finally give the material the properties we know, such as conductivity and magnetism. This makes it difficult to disentangle everything that is going on.

One powerful tool that can still do so is scanning tunneling microscopy. With the scanning tunneling microscope (STM), it is possible to build materials from the individual parts they are made of: atoms. Instead of being forced to work with the materials that are available in nature, the STM allows us to make them ourselves. This permits us to single out specific phenomena we are interested in. We can build, for example, structures starting from single iron atoms and see how magnetism as we know it manifests itself as we make the structures bigger [1].

There is, however, a catch. The structures we study cannot be floating in thin air and instead have to be deposited on or embedded in a surface. This surface, which is usually a metal, consists itself of many atoms which influence our measurements of the atomic structures. Fortunately, computer models exist that can tell us the influence of the metal.

In this thesis, motivated by recent STM-performed experiments, we build upon the existing computer models and apply them to three different systems where the surface plays an essential role, in order to better understand the respective measurements and their future possibilities. These three systems are:

- Single atomic magnets in an external magnetic field, which lose their quantum properties due to the surface they reside upon

- Yu-Shiba-Rusinov(YSR) states, resulting from the interaction between magnetic atoms and a superconductor, which can only exist because of the surface

- Field-emission resonances, i.e. electronic states that live in the vacuum near a surface, of which the current resistance is determined by the surface

1.2. THREE SYSTEMS OF INTEREST

1.2.1. SINGLE ATOMIC MAGNETS

One interesting example where the surface place a role in STM measurements is atomic magnets in an external field. Magnets are a natural candidate for storing information. We can assign a "0" to their field pointing in one direction and a "1" to their field pointing in the opposite direction to make up a "bit". But can we do better? It turns out that for sufficiently small single atomic magnets, we can store additional information in a single magnet called quantum information, the type of information of quantum computers.

Electrons have an intrinsic magnetic moment called spin. Atoms that carry magnetism, such as iron and nickel, are nothing more than atoms with electrons arranged

such that a net spin is left. Now, when we place such a single atom spin in a much bigger magnetic field, the atom spin, if free to rotate its magnetic moment, will line up with the much bigger magnetic field like a compass needle pointing north.

It becomes more interesting if we use techniques of the STM as explained in section 2.2 to force the spin to not align with the magnetic field. In this case, the atom spin starts to rotate around the direction of the magnetic field like a gyroscope. This rotation is called Larmor precession. It is completely deterministic. At every point in time, we know the phase of the rotation. This property is called coherence.

The larger the atomic spin, the more energy is required to rotate the spin away from aligning with the magnetic field. So, the coherence property is only present for spins small enough. In fact, the property ties in directly with the quantum nature of such small spins. We can use the coherence to store quantum information.

Unfortunately, the atomic magnets must reside on a surface, which, for the STM to function properly, has to be a conducting surface, so preferably a metal. The problem is that metals have free electrons, which can completely distort the spins. We then lose track of their phase and thus of their quantum information. There are ways around this. To start with, we can place a small insulating layer in-between the metal surface and our atomic magnets of interest. This decouples the magnets from the free electrons allowing it to keep its coherence over a longer time. Yet, we cannot fully decouple from the surface, so after some decoherence time the quantum information will always be lost. The time is typically in the order of 100s of nanoseconds [2].

Perhaps we can do better if we store the information in the atomic nucleus spin rather than the electron spins. The nucleus is surrounded by many electrons and is therefore less easily distorted by additional free electrons from the surface. The fact that the nucleus is less accessible makes it, however, also more difficult to store information in it in the first place. Still, this has already been achieved in other setups [3, 4]. In Ch. 5 we show how to do so in the STM setup.

Another question is whether we can change the quantum information at will. Thanks to recent advancements in STM technology, we can completely control the quantum information of a single spin. It still remains to be shown that we can also do so for two spins. In contrast to one spin, two spins can store a special kind of shared quantum information called entanglement. The nature of STM technology makes it particularly difficult to prove that we have stored entanglement. In Ch. 6 we present a proposal to nonetheless do so. Such a proposal has as a requirement that everything needs to happen within the decoherence time. So, simulating the surface properly is essential to judge whether it is feasible.

1.2.2. YU-SHIBA-RUSINOV STATES OF CLASSICAL SPINS

Another interesting example is single-atom magnets on a s-wave superconductor. Superconductors conduct electrons without resistance but also expel magnetic fields until the field reaches a critical magnitude. The Maglev trains in Japan are built upon this last principle [5]. So then what happens when the magnet is of the size of a single atom and placed on top of the superconductor? Is the field expelled or is it strong enough to penetrate and break superconductivity? And does this happen everywhere in the superconductor or only very locally around where the atomic magnet is placed? It is these questions

1

originating from curiosity that ultimately drive condensed matter research. Below, we will give an initial answer, which is far from complete. A more complete description is given in Ch. 2.

To understand the answer, it is essential to know how superconductors work. For the s-wave superconductors considered in this thesis, the 1957 theory of Bardeen, Cooper, and Schrieffer (BCS) offers a full explanation [6]. It poses that superconductors are metals, which, when cooled down below a certain critical temperature, have their conduction electrons pairing up, which would normally repel each other due to their charge. These so-called Cooper pairs are bound strongly together such that their corresponding current does not experience any resistance. Only when enough energy is put into the superconductor by heating it up or exposing it to a magnetic field, the pairs can break up again resulting in a normal metal current flow.

Knowing this, a natural follow-up question is: what happens when a superconductor carrying Cooper pairs is coupled to a normal metal conducting normal electrons? The answer to this was given by Andreev in 1964 [7]. A normal metal electron traveling towards a superconductor with an energy coinciding with the superconductor Cooper pairs creates a traveling Cooper pair in the superconductor and a deficit of an electron (hole) moving the opposite direction back into the normal metal. This hole thus carries the opposite charge of the initial electron. The total process is called Andreev reflection. It also works in the opposite direction. So, a hole incident to a superconductor creates an electron moving in the opposite direction. This means that we can trap electrons in a superconductor-normal metal-superconductor junction. Electrons of the normal metal traveling towards one of the superconductors reflect into holes traveling the opposite direction where they meet the other superconductor reflecting back into electrons and so on. We refer to these electrons as Andreev bound states as they are normally free to move but are now locally bound due to the superconductors.

This is exactly what we need to explain what happens when we place single atomic magnets on a superconductor. The electrons responsible are usually far away from the atom core and have, therefore, more freedom to move than the other electrons of the atom. They can thus form an Andreev bound state, which in this case is known as a Yu-Shiba-Rusinov (YSR) state.

We should emphasize that this description only holds for atoms with sufficiently large spin, i.e. atoms with strong Hund coupling [8]: the so-called classical atomic spins. For atoms carrying smaller spin, so-called quantum spins, the interaction between the atom electrons and the superconductor is a more complicated quantum process resembling more the screening of magnetism that can occur when spin-carrying atoms are placed on top of a normal metal known as the Kondo effect [9].

Multiple YSR states that are in close proximity to each other can also interact with each other. Electrons can move from being in a bound state with one magnetic atom to being in a bound state with the next magnetic atom. For atoms arranged in a chain, a 1-dimensional YSR lattice is formed. One reason why these chains are of particular interest is that they are proposed to have a non-trivial state of matter called a topological superconducting phase in which the electrons are split into two parts called Majorana modes residing at each of the ends of the chain and with an energy equal to the Fermi energy [10–12].

1.2.3. FIELD-EMISSION RESONANCE ARTIFICIAL ATOMS

The final system of interest is field-emission resonances. They tie in with the search for artificial atoms. Sometimes, the STM is not suitable for building up certain materials bottom-up. A possible example is Mott-insulators. In this case, an alternative can be to work with other quantum systems that behave very similarly. Instead of working with real atoms, we work with electrons confined to a confining potential, which behave as if they are part of real atoms.

A way to do so would be to have a surface with a vacancy, which can trap the electron, resulting in a near-perfect square well. They appear, for example, in chlorine layers on copper nitride. To truly confine them, we need to also add a potential in the third direction going out of the surface. The STM tip can form this potential when it hovers above the vacancy. The resulting bound electrons are called field-emission resonances.

Artificial atoms created through trapping electrons like this have a certain probability of losing these electrons over time to the environment. Ideally, this lifetime is as long as possible. The lifetime thus forms a good metric to compare different types of artificial atoms.

1.3. THIS THESIS

In this thesis, we zoom in further on the above examples: YSR states, atomic coherence on metallic surfaces, and field-emission resonances.

We start, in Ch. 2, with a more in-depth discussion of the relevant background. This includes general Hamiltonians of spins on a surface, general STM techniques, general surface scattering problems, and the theory specific to the three systems of studies.

For YSR states we look at the band structure of YSR chains. Recently, this structure has been measured using STM and it was found that it cannot be explained by simple models. We present, in Ch. 3, a new method to evaluate the YSR band structure based on the theory of short junctions. With this method, we can compute the effective Hamiltonian of a YSR chain when we only know the self-energy at the Fermi level. We benchmark the method through a single orbital model and evaluate an atomic spin-orbit model to further show its use. We find that the YSR band structure heavily depends on the Fermi surface of the metal.

For field-emission resonances, in Ch. 4, we show that the STM spectrum of field-emission resonances in chlorine vacancies on copper nitride indicates an unexpected increase in the lifetime of the resonances when we increase the bias voltage. We model the system and show through density functional theory calculation that the increasing lifetime can be attributed to the complex Fermi surface of copper.

For atomic decoherence, we present various experiments pushing the boundaries of control and show that they can be performed and modeled despite the limitations of decoherence. In Ch. 5, we demonstrate how to use the free evolution of spins to coherently address the nucleus spin through the electron spin of a Ti atom. This work is motivated by the previous success of probing the coherent evolution between Ti electron spins. We also show how we can model the corresponding evolution, combining rate equations and an equation of the Lindblad form.

Next to this, in Ch. 6, we present a way to controllably entangle two Ti spins using an STM and subsequently detect the entanglement. We first present the protocol, which is

based on the free evolution of entangled states. Subsequently, we show that the protocol is feasible in a low-temperature STM when the electron spins lose their coherence due to spin scattering with the underlying surface.

Finally, we present an outlook in Ch. 7, where we make a beginning with studying the behavior of decoherence of the free evolution of Ti spin chains that are larger than two spins.

References

[1] Loth, S., Baumann, S., Lutz, C. P., Eigler, D. & Heinrich, A. J. Bistability in atomic-scale antiferromagnets. *Science* **335**, 196–199 (2012).

[2] Yang, K. *et al.* Coherent spin manipulation of individual atoms on a surface. *Science* **366**, 509–512 (2019).

[3] Pla, J. J. *et al.* High-fidelity readout and control of a nuclear spin qubit in silicon. *Nature* **496**, 334–338 (2013).

[4] Dutt, M. G. *et al.* Quantum register based on individual electronic and nuclear spin qubits in diamond. *Science* **316**, 1312–1316 (2007).

[5] Lee, H.-W., Kim, K.-C. & Lee, J. Review of maglev train technologies. *IEEE transactions on magnetics* **42**, 1917–1925 (2006).

[6] Bardeen, J., Cooper, L. N. & Schrieffer, J. R. Theory of superconductivity. *Physical review* **108**, 1175 (1957).

[7] Pannetier, B. & Courtois, H. Andreev reflection and proximity effect. *Journal of low temperature physics* **118**, 599–615 (2000).

[8] von Oppen, F. & Franke, K. J. Yu-shiba-rusinov states in real metals. *Physical Review B* **103**, 205424 (2021).

[9] Farinacci, L. *et al.* Tuning the coupling of an individual magnetic impurity to a superconductor: quantum phase transition and transport. *Physical review letters* **121**, 196803 (2018).

[10] Choy, T.-P., Edge, J. M., Akhmerov, A. R. & Beenakker, C. W. Majorana fermions emerging from magnetic nanoparticles on a superconductor without spin-orbit coupling. *Physical Review B—Condensed Matter and Materials Physics* **84**, 195442 (2011).

[11] Pientka, F., Glazman, L. I. & Von Oppen, F. Topological superconducting phase in helical shiba chains. *Physical Review B—Condensed Matter and Materials Physics* **88**, 155420 (2013).

[12] Nadj-Perge, S. *et al.* Observation of majorana fermions in ferromagnetic atomic chains on a superconductor. *Science* **346**, 602–607 (2014).

2

EXPERIMENTAL AND THEORETICAL BACKGROUND

In this chapter, we will discuss the relevant background experiments and theory for the chapters to follow. We start with a general introduction to spins on a surface, explaining why we can model them with effective spin Hamiltonians. We continue by introducing experimental techniques of the scanning tunneling microscope to probe these spins. Finally, we zoom in on the effects of the surface by first giving a general introduction to surface scattering problems and subsequently discussing the relevant background for classical spin YSR states and coherent spins on a surface.
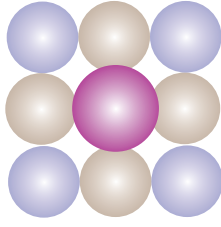
$$|z^2\rangle = |0\rangle$$

$$|xz\rangle = \frac{1}{\sqrt{2}}(|-1\rangle - |1\rangle) \qquad |yz\rangle = \frac{i}{\sqrt{2}}(|-1\rangle + |1\rangle)$$

$$|xy\rangle = \frac{i}{\sqrt{2}}(|-2\rangle - |2\rangle)$$

$$|x^2 - y^2\rangle = \frac{1}{\sqrt{2}}(|-2\rangle + |2\rangle)$$

Figure 2.1: (Partial) orbital momentum quenching for C4v symmetric spin on a surface. Under C4v symmetry, the $|xz\rangle$ and $|yz\rangle$ states are still degenerate, whereas the degeneracy of the other orbitals is lifted. As the atomic d-orbitals are equal superpositions of the orbital momentum states, each individual d-orbital has $\langle L \rangle = 0$. So, in this case, only the $|xz\rangle$ and $|yz\rangle$ states still carry some orbital momentum.

2.1. Hamiltonian of spins on a surface

Atoms behave differently on a surface than in a vacuum. This is because atoms on a surface are surrounded by an environment that is not spherically symmetric such that orbital energy level degeneracies are broken. For d-shell transition metal atoms, when deposited on a square lattice surface, the symmetry of the lattice mostly quenches the d-electron orbital momenta as illustrated by Fig. 2.1. As a result, the low energy excitation spectrum of d-shell atoms such as Ti and Mn is well described by an effective spin Hamiltonian in which all interactions with the remaining orbital momentum and the rest of the environment are small and thus included as perturbations. Interaction with the orbitals is included as a second-order perturbation of spin-orbit coupling of the form:

$$H_{\text{SOC}} = \alpha \boldsymbol{L} \cdot \boldsymbol{S}, \tag{2.1}$$

with $\boldsymbol{L}$ the orbital momentum vector and $\boldsymbol{S}$ the spin. Interactions with the surrounding crystal through the crystal field give rise to an additional anisotropy term to the effective spin Hamiltonian.

2.1.1. Zeeman term

When exposed to a magnetic field, consecutive spin levels are energy split by a Zeeman term

$$H_{\text{Zeeman}} = -\mu_B \boldsymbol{B} \cdot \bar{\boldsymbol{g}} \cdot \boldsymbol{S}, \tag{2.2}$$

where μ_B is the Bohr magneton, B the external magnetic field vector and S the total spin of the atom. $\bar{\boldsymbol{g}}$ is the g-factor tensor, which depends on the type of atom and the side the atom resides on. This is because the effective spin Hamiltonian is perturbed by the surface. This perturbation results in a modification of the effective g-factor. The B field here can have different origins. For example, in addition to an externally applied homogeneous field, a spin-polarized tip, as further introduced in Sec. 2.2.5, emits an effective B-field B_{tip}.

2.1.2. DIPOLAR COUPLING

The effective spin Hamiltonian is also affected by nearby spins. Spins, being magnetic moments, act on each other through dipolar coupling. This coupling is anisotropic and decreases cubically with increasing distance between the spins, as illustrated by Fig. 2.2b. The full Hamiltonian description is:

$$H_{ij}^{\text{dipolar}} = D_0 \left(\mathbf{S}_i \cdot \mathbf{S}_j - 3(\mathbf{S}_i \cdot \hat{\mathbf{r}}_{ij})(\mathbf{S}_j \cdot \hat{\mathbf{r}}_{ij}) \right), \tag{2.3}$$

with $\hat{\mathbf{r}}_{ij}$ the inter-atomic unit vector from atom i to atom j and D_0 the distance r_{ij}-dependent dipolar strength

$$D_0 = \frac{\mu_0 \mu_B^2 g^2}{4\pi^2 r_{ij}^3}. \tag{2.4}$$

Here, μ_0 is the magnetic permeability of the vacuum. g is approximated to be isotropic in this expression.

2.1.3. EXCHANGE COUPLING

If the spins are close enough such that the atom electron wave functions overlap, the spins couple through isotropic exchange coupling, decreasing exponentially in strength with increasing distance between the spins. This is illustrated by Fig. 2.2a. So the Hamiltonian is

$$H_{ij}^{\text{exchange}} = -J(r_{ij})\mathbf{S}_i \cdot \mathbf{S}_j \tag{2.5}$$

with J the exchange coupling depending on the distance r_{ij} through a characteristic decay length r_0 as

$$J(r_{ij}) \propto e^{-r_{ij}/r_0}. \tag{2.6}$$

Spins of which the wavefunctions do not directly overlap can still be coupled through the same Hamiltonian term when the surface mediates the interaction. The origin of this coupling to the surface is further explained in Sec. 2.6.2. Fig. 2.2 shows how the energy diagram of two spins on a surface changes due to magnetic field, dipolar coupling, and exchange coupling.

2.1.4. HYPERFINE COUPLING

Isotopes of atoms exist with a finite spin in the nucleus. In this case, there is hyperfine exchange coupling between the nucleus spin and the electron spin. There are various origins of the coupling. One of them is indirect coupling, in which the outer shell d-electrons spin wavefunction overlaps with inner shell s-electrons, causing a finite spin density, which interacts with the nucleus spin. This is the Fermi-interaction term, which is isotropic. Another origin is direct dipolar coupling between the d-electrons and the nucleus, which is anisotropic. Both are illustrated by Fig. 2.3. We can describe the total by the effective Hamiltonian

$$H_{ij}^{\text{hyperfine}} = \mathbf{S}_i \cdot \bar{\mathbf{A}}_{ij} \cdot \mathbf{I}_j. \tag{2.7}$$

$\bar{\mathbf{A}}_{ij}$ is the hyperfine coupling tensor which is in general anisotropic [1].

2
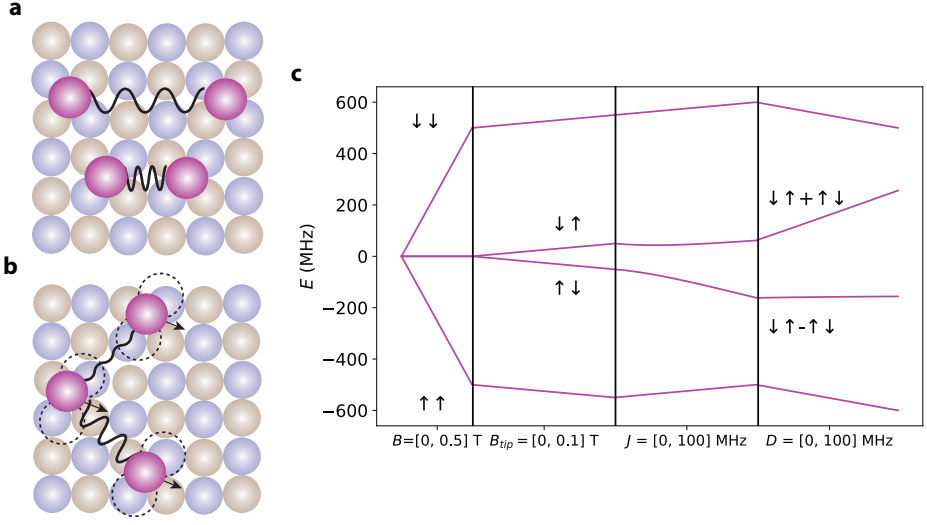
Figure 2.2: Two spin interactions on a surface (a) Schematic of exchange coupling between spins on a surface. The interaction is isotropic and increases exponentially when the spins get closer. **(b)** Schematic of dipolar coupling between spins on a surface. The interaction scales cubically and is anisotropic. It is the biggest when the dipolar field aligns with the spins. **(c)** Energy spectrum of the spin eigenstates of two spins on a surface. First, we increase the field B, causing the spins to Zeeman split. Then, we increase the tip field B_{tip}, which is only felt by one of the spin splitting ↑↓ from ↓↑. Subsequently, we introduce exchange coupling J, which causes the spins to couple and form singlet-triplet states. Finally, we add dipolar coupling, which further splits the singlet and triplet state while leaving the singlet state untouched.

2.1.5. QUADRUPOLE MOMENT

Nuclear spins larger than $\frac{1}{2}$, i.e. consisting of multiple charges, have a non-spherical charge distribution, giving rise to an electric field quadrupole moment Q. The surrounding electron cloud with field q can exert a torque eq on this moment, as illustrated by Fig. 2.3, which affects the spin of the nucleus. The corresponding effective spin Hamiltonian term is

$$H^{\text{quadrupole}} = \boldsymbol{I} \cdot \bar{\boldsymbol{Q}} \cdot \boldsymbol{I} \tag{2.8}$$

with $\bar{\boldsymbol{Q}}$ the quadrupole tensor which can be expressed in matrix form as:

$$\bar{\boldsymbol{Q}} = \frac{e^2 q Q}{4I(2I-1)} \begin{bmatrix} -(1-\eta) & 0 & 0 \\ 0 & -(1+\eta) & 0 \\ 0 & 0 & 2 \end{bmatrix} \tag{2.9}$$

with $0 < \eta < 1$ the in-plane anisotropy of the electric field gradient.

2.2. STM TECHNIQUES

2.2.1. IMAGING WITH THE STM

In order to detect such atoms on a surface we cannot use a light-based microscope as its resolution is limited by the diffraction limit, which is much larger than the atomic limit.
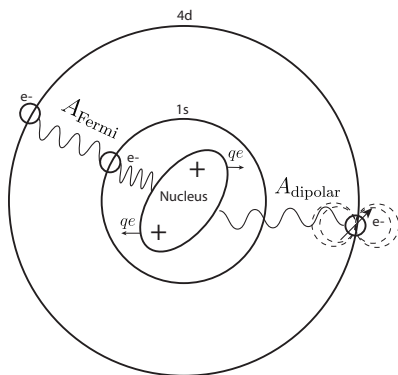
Figure 2.3: Schematic of nuclear spin interactions. If the distribution of protons deviates from being spherical, the surrounding electron cloud exerts a torque qe on the protons, causing a quadrupole term in the effective nuclear spin Hamiltonian. Next to that, surrounding electrons can dipole couple with the nucleus spin (A_{dipolar}) or super-exchange couple (A_{Fermi})

Even electron microscopes, which replace light beams with smaller wavelength electron beams, run into the diffraction limit when trying to image single atoms. The scanning tunneling microscope (STM) is not based on reflecting wavefunctions and is, therefore, not held back by the diffraction limit. Instead, it makes images by picking up currents of a conducting sample with an atomically sharp tip [2]. This tip is attached to piezo-electric crystals through which it can move in all cardinal directions with atomic precision.

The main type of measurement that we do with an STM involves tunneling currents. For these measurements, the tip is not brought in direct contact with the sample of interest but is rather hovering less than a nm above it as illustrated by Fig. 2.4a. As a result of quantum mechanics, the electrons still have a finite chance to quantum tunnel in between the tip and sample, which, when biased through a DC voltage, causes a small current to flow. As this current depends exponentially on the distance between the sample and the tip, we can measure relative differences in the height of the sample. We can do this so precisely that we can detect the presence of a single atom on the surface. It makes STM into a microscope at the atomic scale.

The STM can image in two modes: constant current and constant height mode. For the former, a feedback loop with the piezo-electric crystal causes the tip to move such that we always measure the same current. Then, the tip movement is a direct measurement of the height differences of the surface. For the latter, the tip is held at the same place such that now the measured current is a direct measurement of the height differences of the surface. Fig 2.4b shows a typical constant height measurement in which the brighter colors represent higher currents. The extrusions are the single atoms deposited on the surface. We can further decouple the atoms from the surface by adding insulating islands in between, such as layers of MgO. The island in Fig. 2.4b is such an island.

To be more precise, the current the STM measures is the difference between a stream of electrons from tip to sample and from sample to tip [3]

$$I = I_{s \to t} - I_{t \to s}, \tag{2.10}$$

$$I_{s \to t}(V) \propto \int_0^{eV} e^{-k(\omega)d} f_s(\omega - eV)(1 - f_t(\omega))\varrho_s(\omega - eV)\varrho_t(\omega)d\omega, \tag{2.11}$$

$$I_{t \to s}(V) \propto \int_0^{eV} e^{-k(\omega)d} f_t(\omega)(1 - f_s(\omega - eV))\varrho_t(\omega)\varrho_s(\omega - eV)d\omega. \tag{2.12}$$

The characteristic exponential dependence on the distance d between the sample and the tip has $k(\omega)$ as corresponding decay constant. In the Wentzel-Kramer-Brillouin (WKB) approximation, it holds that

$$k(\omega) = 2\sqrt{m_e(\Phi_t - \Phi_s - eV + \omega)}, \tag{2.13}$$

where m_e is the mass of the electron and $\Phi_{t/s}$ the work function of the tip/sample.

Furthermore, each of the two currents is a convolution of the densities of states $\varrho_{t/s}$ of the tip and sample respectively , integrated over the bias voltage V that we apply to the junction. As a result, the STM can also probe changes in the electronic configurations of both the tip and the sample. The temperature dependence of the density of states is captured by the Fermi functions $f_{t/s}$.

2.2.2. STM CONDITIONS TO IMAGE ATOMIC SPINS
The energy transitions of spins on a surface are in the order of meV. So, in order to image and study these spins in a controlled way, the temperature of the STM must be low to limit thermal excitations, and the vacuum must be high to limit interactions with surrounding particles in the STM chamber.

Low temperatures can be reached with cryogenic liquids. The STM, as used in the experiments referred to in Ch. 4 and 5, is a Unisoku USM-1300 cooled by liquid ^{3}He.

2.2.3. LATERAL AND VERTICAL ATOM MANIPULATION
Thus far, we have only discussed imaging techniques. What makes the STM more than a very advanced microscope is that the tip can also be used to make atomic structures of interest [4]. Through the tip's van der Waals force, we can drag atoms over an underlying surface called lateral manipulation. Moreover, if we apply bias pulses to the tip, we can pick up some of the atoms, such as Fe, and drop them at a specific place on the crystal lattice. This is called vertical manipulation. As the spin interactions depend on the inter-atomic distances(see 2.1.2 and 2.1.3), atom manipulation allows for large freedom in engineering the spin interactions of spin systems [5].

2.2.4. INELASTIC TUNNELING SPECTRUM (IETS)
STM currents can also directly change the state of a system of study by exciting it inelastically. Hereby, energy is transferred to the sample system through interaction with the tunneling current. If we include inelastic excitation we can write the total net current
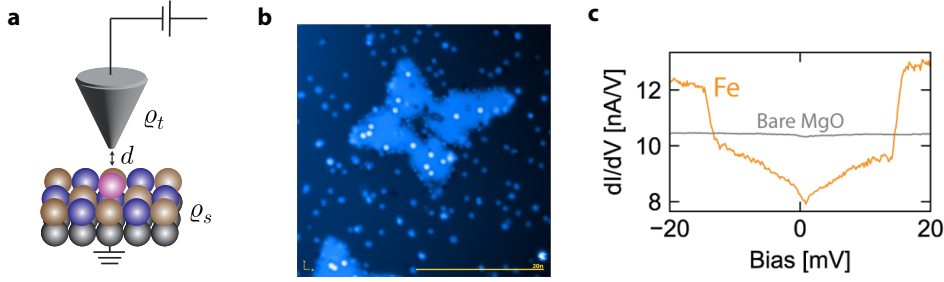
Figure 2.4: STM imaging and spectroscopy. (a) schematic of a typical Scanning tunneling microscopy set-up. ϱ_t and ϱ_s are the densities of states of the tip and the sample, and d is the distance between the STM tip and the sample. **(b)** Image in constant height mode of Fe atoms on top of MgO on Ag(110), **(c)** dI/dV spectrum of bare MgO and Fe on MgO as measured by Veldman et al. [7]

between the sample and the tip as [6]

$$I = I_{s \to t} - I_{t \to s} \tag{2.14}$$

$$I_{s \to t} = \int \sum_{i,f} |T_{if}^{s \to t}|^2 f_s(\omega - eV) \varrho_s(\omega - eV)(1 - f_t(\omega - \omega_{if})) \varrho_t(\omega - \omega_{if}) d\omega \tag{2.15}$$

$$I_{t \to s} = \int \sum_{i,f} |T_{if}^{t \to s}|^2 f_t(\omega) \varrho_t(\omega)(1 - f_s(\omega - eV - \omega_{if})) \varrho_s(\omega - eV - \omega_{if})) d\omega, \tag{2.16}$$

where the sum over i, f is over possible initial and final states of the sample system as a result of the interaction. T_{if} is the corresponding transfer matrix and ω_{if} is the corresponding energy difference. $f_{s/t}$ are the Fermi distribution functions of the sample and the tip respectively. They include the temperature broadening to the overall current. In the specific case of spin excitations, the conservation of angular momentum requires the electron responsible for the excitation to flip its spin.

The measured current increases suddenly when the bias is such that a new inelastic excitation is possible. This is best visible in the differential spectrum $\frac{dI}{dV}$ in which energy excitations show up as jumps at the voltage that produces the onset energy for the excitations. We can use the $\frac{dI}{dV}$ spectrum to tell different spinful atoms apart as they have distinct spin excitation spectra. As a example Fig. 2.4c shows a $\frac{dI}{dV}$ spectrum of an Fe atom with a step around 14 meV related to the first spin excitation.

2.2.5. SPIN-POLARIZED STM

We can change the tip in order to further change the measurement capabilities of the STM. The tip can be terminated, for example, in a spin by picking up Fe atoms, using the same technique as for vertical manipulation. The result is that ϱ_t becomes spin-dependent, allowing spin-polarized measurements. The majority spin of the tip becomes the polarization of the current. As a result, we can obtain images with spin contrast and measure the orientation of single surface spins.

With a spin-polarized tip, we can also do spin pumping. In this case, we apply a bias higher than the excitation energy as with IETS. Due to the spin polarization of the current,
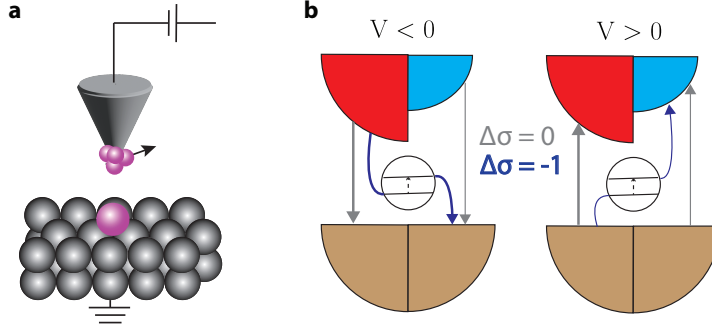
Figure 2.5: Spin polarized STM. (a) Schematic of an STM setup with a spin-polarized tip. $\varrho_{t/s}$ is the density of states of respectively the tip and the sample. d is the distance of the tunnel junction. **(b)** Schematic to explain elastic ($\Delta\sigma = 0$) and inelastic current ($\Delta\sigma = -1$) in the case of a spin-polarized tip. For a positive/negative bias V, the tip majority/minority spin dominates the elastic current. For a positive bias, due to spin selection rules, the inelastic current is higher than for a negative bias.

the excitations now have a preferred spin direction. Depending on the sign of the applied bias $\Delta s = +1$ transitions are preferred over $\Delta s = -1$ or vice versa. This is illustrated by Fig. 2.5.

2.2.6. DC PUMP-PROBE
All the STM techniques described thus far are limited in measuring time-dependent behavior. This is because, for a large signal-to-noise ratio, measurements often take much longer than the dynamics of interest. Pump-probe spectroscopy, compatible with the thus-far-described setup, provides a possible way around this limitation. Here, first, we send a DC pulse to excite the system, then there is some waiting time τ, and then we send a DC pulse to read out the system. The state at time t is obtained by time-averaging many iterations with $\tau = t$. When we subsequently sweep τ, we can measure the time-dependent dynamics as we are only limited now by the length of the DC pulses, which is in the range of ns. We can use the pump-probe technique specifically for atomic spins to study how the spin state relaxes to thermal equilibrium after a spin excitation.

2.2.7. ELECTRON SPIN RESONANCE
The techniques thus far also have limited energy resolution due to the thermal broadening as captured by the Fermi functions. To overcome this limit, one of the most recent additions to the STM toolbox is electron spin resonance (ESR). For this technique, we send a radio frequency (RF) to the STM junction, which in turn can coherently excite the sample when the frequency is in resonance with the spin excitation energy of the sample (see Fig. 2.6a). The exact mechanism behind ESR in the STM is still under debate, but what is clear is that the RF voltage (V_{RF}) results in an effective experienced oscillating field with amplitude $\Delta\boldsymbol{B} = \boldsymbol{c} V_{RF}$ which drives the spin transition. Here, $\boldsymbol{c}$ is a vector of proportionality constants with units T/V. A model Hamiltonian of the form

$$H_{\mathrm{ESR}} = \left(\boldsymbol{c} V_{RF} \sin\left(2\pi f_{\mathrm{RF}} t + \phi_{\mathrm{RF}}\right)\right) \cdot \boldsymbol{S} \tag{2.17}$$

has therefore been very successful in describing the spin excitation behavior, where S is the vector of spin operators in the x, y, and z-direction. ϕ_{RF} is a potential additional phase of the RF signal.

Under the influence of this Hamiltonian, any spin transition that can be achieved through $c V_{RF} \cdot S$ is Rabi-driven as long as the signal frequency is close enough to the energy gap of the transition.

Neglecting decoherence effects for now, the spin alternates phase coherently between the two states of the transition with Rabi frequency:

$$\Omega = \sqrt{(c_\perp V_{RF})^2 + (|f_{RF} - f_{ESR}|)^2}, \tag{2.18}$$

where f_{ESR} is the ESR energy transition and $c_\perp$ is the projection of c on the driven spin excitation. When driving perfectly on-resonance, so $f_{RF} = f_{ESR}$, the Rabi frequency $\Omega_0 = c_\perp V_{RF}$. Driving off-resonance thus leads to a larger Ω (see Fig. 2.6d).

A straightforward way to detect ESR is through a spin-polarized measurement with a DC bias. The Rabi oscillation is time-averaged out in such a measurement and results in a change in the DC bias current. Sweeping over f_{RF} at the resonance frequency the current results in a peak or a dip at the resonance frequency, depending on the sign of the bias. Part of the detection can also come from the RF signal as the changing conductance in the junction to the the spin resonance interferes with it. This is called homodyne detection and results in an asymmetric spectrum. Typical spectra for DC- and homodyne detection are shown in Fig. 2.6b and c.

The first discovery of ESR in the STM was with a tip field radiating from a spin-polarized tip and Fe atoms deposited on MgO on Ag [8]. Since then, different other substrates have been tried but to no avail. This led to the belief that the substrate is important for the mechanism. One of the prominent theories is that the substrate reacts piezo-electrically to the RF voltage, hereby changing the size of the tunnel junction periodically, resulting in a field gradient [9]. Such a mechanism would be similar to the working of micromagnets in the ESR driving of spin qubits [10]. However, the change in the size of the tunnel junction has not yet been observed. Some calculations claim that this effect should be limited and that there might be other mechanisms at play. A more general theory framework based on quantum transport showed that also variations in the tunnel barrier height next to size could lead to Eq. 2.17 and does seem to have the right order of magnitude [11, 12]. Still, as of today, any theory not including the substrate has a hard time to explain why ESR thus far has only been measured on MgO.

2.2.8. PULSED ESR FOR QUBIT OPERATIONS

Recently, the ESR technique has been used in pulses to conduct coherent operations on Ti on MgO on Ag, which act as an effective spin $\frac{1}{2}$. Treating the spin excitation as a quantum bit, we can perform any single qubit rotation with ESR pulses [13]. We can send pulses of a specific duration, to rotate the qubit with a specific angle around one of the axes, which we can call the x-axis. Changing the additional phase ϕ allows Rabi rotation about any axis in the $x - y$ plane. Then, finally, combining three specific x and y rotation pulses R with respective durations α, β and γ, we can do rotations about arbitrary axis $\hat{n}$ with duration θ [14]

$$\hat{R}_{\hat{n}}(\theta) = \hat{R}_y(\gamma)\hat{R}_x(\alpha)\hat{R}_y(\beta). \tag{2.19}$$
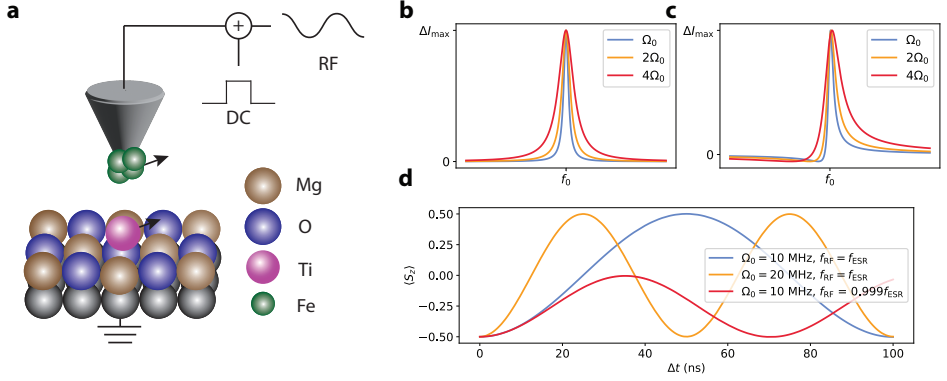
Figure 2.6: ESR-STM. (a) Schematic of electron spin resonance in a scanning tunneling microscope. The RF signal causes the driving, the DC signal causes the DC-detection, and the RF signal causes the homodyne detection. **(b)/(c)** Typical DC-measured(b)/homodyne(c) ESR resonance peak at resonance frequency f_0 for various driving strengths Ω. **(d)** Evolution of the spin expectation values of a spin $\frac{1}{2}$ as coherently driven through electron spin resonance with various driving strengths Ω and driving frequencies f.

2.2.9. Double electron-electron resonance

The working of ESR-STM might make it seem as if it is only possible to drive spins located directly underneath the tip. This is not true. Recent experiments have shown that spins further away can be driven as long as they experience an oscillating local magnetic field moment. We can achieve this by placing an additional Fe atom close to the remote atom we probe. The main driving force is still the RF voltage sent to the tip, but now this signal is mediated by the Fe atom spin, instead of by the tip field. In this way, we can build larger spin structures around the STM tip, of which we can drive each spin independently. For two spins, it is called the double electron-electron resonance(DEER) set-up. A schematic overview of this set-up as well as the typical corresponding ESR spectrum is shown in Fig. 2.7.

2.3. Surface scattering problems

When we probe systems of interest with the STM, the results are always altered by the surrounding bulk. We thus need to consider the full Hamiltonian

$$\hat{H} = \begin{pmatrix} \hat{H}_{\text{sys}} & V \\ V^\dagger & \hat{H}_{\text{surf}} \end{pmatrix} \tag{2.20}$$

as illustrated by Fig. 2.8a. Diagonalizing this Hamiltonian becomes an impossible task.

Fortunately, we can still evaluate the effective system Hamiltonian as altered by the surface through the (retarded) Greens function

$$\hat{G}(\omega) = \frac{1}{\omega - \hat{H} + i\eta}. \tag{2.21}$$

The effective Hamiltonian is the inverse of the Greens function of the system Hamiltonian,
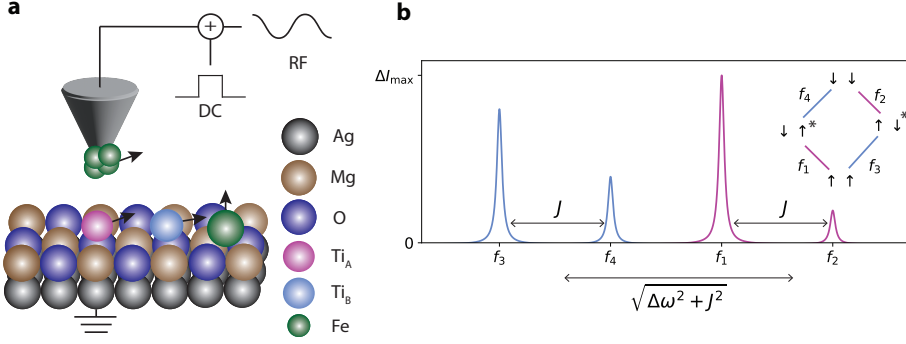
Figure 2.7: Double resonance ESR-STM. (a) Schematic of double electron-electron resonance in STM. **(b)** Schematic of resonance spectrum of two spin STM-DEER spectrum. The inset shows the corresponding energy diagram. The exchange coupling J between the Ti spins causes the peaks related to a spin-flip of each of the individual atoms to split up. This also means the eigenstates slightly deviate from ↑↓ and ↓↑, hence the ∗'s. Additionally, the resulting sets of spin are $\sqrt{\Delta\omega^2 + J^2}$ apart instead of just the difference in Zeeman splitting $\Delta\omega$.

which in turn, using the Schur complement, is equal to [15]

$$\hat{H}_{\text{eff}} = \hat{H}_{\text{sys}} + \hat{V}\hat{G}_{\text{surf}}\hat{V}^\dagger = \hat{H}_{\text{sys}} + \hat{\Sigma}(\omega), \tag{2.22}$$

where $\hat{\Sigma}(\omega)$ is the energy dependent self-energy. Because it is energy-dependent, a non-linear eigenvalue equation needs to be solved to compute the spectrum. There are ways to do so, but it is easier to plot the corresponding local density of states (LDOS) ϱ, which can be found as

$$\varrho = -\frac{1}{\pi}\text{Tr}(\text{Im}(\hat{G})) \tag{2.23}$$

The additional benefit is that this is the quantity that best matches the dI/dV spectrum of the system as measured by an STM.

Alternatively, as illustrated by Fig. 2.8b we can solve the scattering problem of the system. The surface has free electronic modes $\phi_+ e^{ik_+}$. They scatter from H_{sys} into modes propagating away again from the interface $\phi_- e^{-ik_-}$. At every real space coordinate j away from the interface, the surface wavefunction is a linear combination of these modes

$$\psi_{\text{surf}}(j) = \hat{\Phi}_+\hat{\Lambda}_+^j q_+ + \hat{\Phi}_-\hat{\Lambda}_-^j q_-, \tag{2.24}$$

where Λ is a matrix with e^{ik} on the diagonals and $\hat{\Phi}$ the matrix of ϕ.

Far from the interface, the surface approaches the bulk and the q_+ and q_- can be related through a scattering matrix $\hat{S}$. Combined, this gives a scattering problem of modes which we can solve to find Ψ_{sys} at energy ω, i.e. the spectrum [15]

$$\begin{pmatrix} \hat{H}_{\text{sys}} - \omega & \hat{V}^\dagger\hat{\Phi}_+\hat{\Lambda}_+ \\ \hat{V} & -\hat{V}\hat{\Phi}_+ \end{pmatrix}\begin{pmatrix} \hat{\Psi}_{\text{sys}} \\ \hat{S} \end{pmatrix} = \begin{pmatrix} -\hat{V}^\dagger\hat{\Phi}_-\hat{\Lambda}_- \\ \hat{V}\hat{\Phi}_- \end{pmatrix}. \tag{2.25}$$
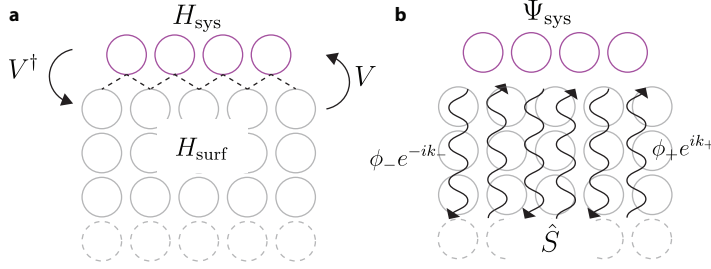
Figure 2.8: Surface scattering problems. (a) illustration of the Greens function formalism of quantum transport, **(b)** illustration of the scattering matrix formalism of quantum transport

2.4. HAMILTONIAN OF A CLASSICAL SPIN YSR STATE

One interesting scattering problem consists of spins on a superconductor. According to BCS theory, the s-wave superconductor particle energy spectrum has a gap Δ around the Fermi level for which no states are available (see the bare superconductor spectrum of Fig 2.9a). States located at energies below Δ in the metallic phase, become bunched up at the energy Δ at the superconducting phase, forming coherence peaks. This can be written in a Bogliobov-de-Gennes (BdG) Hamiltonian [16]:

$$\hat{H}_{\text{BdG}} = (-\frac{\hbar^2 \boldsymbol{\nabla}^2}{2m} - \mu + V)\tau_z + \Delta\tau_x\sigma_z. \tag{2.26}$$

A classical spin, i.e. with Strong Hund coupling, on top of an s-wave superconductor results in a Yu-Shiba-Rusinov (YSR) bound state, as s-wave electrons scatter from the spin and get trapped through Andreev reflection in the spin-superconductor junction (see the inset of Fig. 2.9a). One can model these bound states through a tight-binding scattering problem as in Eq. 2.22. This involves using

$$\begin{aligned}
\hat{H}_{\text{surf}} &= \hat{H}_{\text{BdG}}, \\
\hat{H}_{\text{sys}} &= -BS\sigma_z\tau_z, \\
\hat{V} &= -t_{\text{YSR}}\tau_z,
\end{aligned} \tag{2.27}$$

where B is the Zeeman splitting of the atomic spin S pointing in the z direction that forms the YSR state. In Fig. 2.9a we solve for the effective Hamiltonian using the framework of Istas et al. [17] and plot the corresponding LDOS ρ. The YSR state appears as a peak in the particle-hole symmetric excitation spectrum. Additionally, the coherence peaks decrease in size as the overall amount of particles must be conserved.

For an alternative model of YSR states, we can treat the spin as altering the superconductor. In that case

$$\begin{aligned}
\hat{H}_{\text{sys}} &= \hat{H}_{\text{BdG}}, \\
\hat{\Sigma}(\omega) &= t_{YSR}^*\tau_z\frac{1}{\omega - BS\sigma_z\tau_z}t_{\text{YSR}}\tau_z \\
&= (\frac{|t_{\text{YSR}}|^2\omega}{\omega^2 - B^2S^2} - \frac{BS|t_{\text{YSR}}|^2}{\omega^2 - B^2S^2}\sigma_z)\tau_z
\end{aligned} \tag{2.28}$$
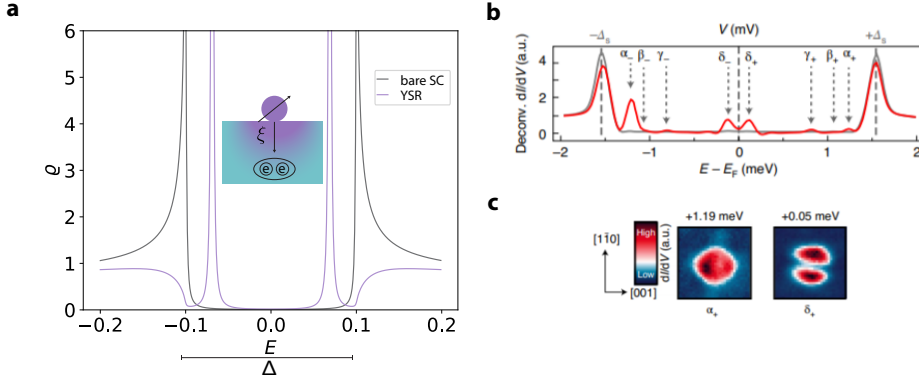
Figure 2.9: YSR states of classical spins (a) LDOS calculation of a single YSR state following Eq. 2.30 Arrows indicate shifting of the YSR states with surface coupling J. The inset shows a schematic of the effective exchange between Cooper pairs and the adatom spin, resulting in a YSR state, **(b)** dI/dV as measured by Schneider at al. for Mn on Nb(110) [19] and **(c)** corresponding spatial distribution of the YSR state wavefunctions [19]

. Taking as an additional approximation that the original spin states are deep in the gap, i.e. $B, \Delta \gg \omega$, which is equivalent to the zero-bandwidth approximation for the superconductor and the case for classical spins [18], we can reduce the $\hat{\Sigma}$ expression to

$$\hat{\Sigma}(\omega) \approx \frac{|t_{\text{YSR}}|}{B} \sigma_z \tau_z. \tag{2.29}$$

Now, defining $J \equiv \frac{|t_{\text{YSR}}|}{BS}$, we can write the total effective YSR Hamiltonian as

$$\hat{H}_{\text{eff}} = \hat{H}_{\text{BdG}} + J\sigma_z, \tag{2.30}$$

which shows that YSR states can also be seen as resulting from some effective exchange J between Cooper pairs and an atomic spin. It is an effective model that is well studied [18] and shows resemblance with Kondo spin screening as known for normal metals, though, here, for classical spins, it is not a many-body effect.

In general, even for classical spins, this is an oversimplification. All weakly bound electrons that make up the total spin of the atom can interact with the surface and form YSR states. The result is multiple in gap states with a clear orbital character reflecting the orbital wavefunction of the original atom electron. This was measured through dI/dV by, for example, Schneider et al. [19] (see Fig. 2.9b and c). Such measurements are performed with a superconducting STM tip. These tips have a much higher energy resolution than regular metal tips as ϱ_t is dominated by the superconducting coherence peaks and thus only picks up ϱ_s at the energy of the coherence peaks. This is necessary to measure the narrow YSR peaks.

2.5. YSR BANDS AND TOPOLOGICAL SUPERCONDUCTIVITY

YSR states for spin chains on superconductors hybridize into a full YSR band structure. The effective Hamiltonian in the single-orbital zero-bandwidth approximation takes the

2

form of Eq. 2.30. Over the years, these chains have received a lot of attention as the expected effective Hamiltonian is very close to the Kitaev model Hamiltonian for a *s*-wave superconductor [20]

$$\hat{H}_{\text{Kitaev}} = (-\frac{\hbar^2\nabla_x}{2m} - \mu + V(x))\tau_z + \Delta\tau_x\sigma_z + J(x)\sigma_z + i\alpha\sigma_y\nabla_x. \tag{2.31}$$

This model describes superconductors with Cooper pairs consisting of identical spins (*p*-wave pairing). The effective YSR Hamiltonian of eq. 2.30 only misses a term to break spin projection symmetry to be of the same shape. We can for example generate this term is we use a superconductor with strong spin-orbit coupling. Inversion symmetry breaking at the superconductor surface then leads to Rashba spin-orbit coupling [21]

$$\hat{H}_{\text{Rashba}} = i\alpha_{\text{R}}\sigma_y\nabla_x, \tag{2.32}$$

with Rashba strength α_{R}.

In contrast to normal *s*-wave superconductors, the $\hat{H}_{\text{Kitaev}}$ bulk dispersion undergoes a phase transition for $J > \sqrt{\mu^2 + \Delta^2}$ that is accompanied by a gap opening in the dispersion. At the same time states appear exponentially localized at the ends of the chain and pinned to the Fermi energy by particle-hole symmetry. These states are known as Majorana bound states. They are spinless, chargeless, non-abelian anyons, meaning that if we interchange them, the result is a unitary transformation more than just an overall phase factor. Moreover, due to particle-hole symmetry, they are protected against local energy perturbations, making them an interesting candidate to study quantum coherent operations [22, 23].

For the systems in STM local traces have been found of the modes [24], but it is difficult to draw conclusions from them as these traces can also belong to other states [25]. More conclusive evidence comes from global features like the opening of the bulk gap . Recent technical improvements have made it possible to observe the bulk dispersion [19, 26]. From these measurements it is clear that a gap in the dispersion, large enough to conclusively detect Majorana bound states, has not been achieved yet. It requires further study of the bulk dispersion to understand if and how this could still be done.

Even if the modes would be detected in an STM, it remains to be seen if any quantum operations can be performed on them, as this requires the interchange of the states, for which the slow STM tip as only probing possibility becomes a limiting factor.

2.6. THEORY FOR COHERENT ATOMIC SPINS
Another example of a scattering problem consists of atomic spins weakly coupled to a metal. We can achieve this through the previously described thin insulating layers such as MgO. The spins are then isolated quantum systems whose state, including the quantum phase, we can control very well by STM. As such, they are promising for quantum simulations.

2.6.1. DECOHERENCE
Unfortunately, the metal has free electrons that can scatter with the spins, causing the spins to lose their quantum phase information over time.

We can distinguish two types of processes here. First of all, electrons can inelastically scatter. Here, the electrons that scatter with the spins exchange energy with each other, causing the spins to thermally equilibrate over time with the metal. This is known as relaxation. The scattering can also be elastic. Here, the electrons that scatter do not exchange energy. They do, however, alter the phase of the spin randomly. This is known as pure dephasing.

As both are statistical processes, they require a quantum state description following the density matrix formalism. The density matrix $\hat{\rho}$ of the spin system is of size $N_{\text{sys}} \times N_{\text{sys}}$, with N_{sys} the number of eigenstates of the system. We can express it in any basis, but it is often represented in the energy basis where the states are the energy eigenstates. In this basis the diagonal entries ρ_{nn} are the populations representing a statistical possibility for the system to be in the corresponding eigenstate. On the off-diagonals ρ_{nm} are the coherences representing the phase present between the two eigenstates the term connects. $\hat{\rho}$ has a trace of 1 as the states should be normalized. Furthermore, it is Hermitian. Any effect of the surface on $\hat{\rho}$ should remain this property and, therefore , must be a trace-preserving and completely positive map.

Given these conditions, one can derive the equation describing $\hat{\rho}(t)$ as a result of any interaction with the environment:

$$\frac{d\hat{\rho}}{dt} = -\frac{i}{\hbar}[\hat{H}_{\text{sys}}, \hat{\rho}] + \sum_i \left(\hat{L}_i \hat{\rho} \hat{L}_i^\dagger - \frac{1}{2}\{\hat{L}_i^\dagger \hat{L}_i, \hat{\rho}\} \right), \tag{2.33}$$

where $[.,.]$ is the commutator and $\{.,.\}$ the anti-commutator. The first term is the unperturbed evolution by the Schrodinger equation, also known as von Neumann evolution. The second term contains Lindblad jump operators, which include all the different interactions the environment can have with the system. The whole is known as the Lindblad equation [27].

An example of such a set of Lindblad operators is

$$\hat{L}_r = \sqrt{r_{nm}}|n\rangle\langle m|, \quad n \neq m \tag{2.34}$$

The result is a jump from energy eigenstate n to energy eigenstate m with strength r_{nm}. Inserting this operator, we find that the diagonal elements of $\hat{\rho}$ become decoupled from the off-diagonal elements. The diagonal elements follow

$$\frac{d\rho_{nn}}{dt} = \sum_m \left(-r_{nm}\rho_{nn} + r_{mn}\rho_{mm} \right). \tag{2.35}$$

The set of these equations tells how the populations are changing due to the rates r_{nm} and is therefore also known as the rate equations. The off-diagonal elements follow

$$\frac{d\rho_{nm}}{dt} = -i\Delta\omega_{nm}\rho_{nm} + \frac{1}{2}(\sum_{k \neq n} r_{nk} + \sum_{k \neq m} r_{mk}), \tag{2.36}$$

where $\Delta\omega_{nm}$ is the energy difference between eigenstates n and m and represents the unperturbed quantum phase evolution following the standard time-dependent Schrödinger equation. The second term represents the loss of phase because of inelastic scattering. It is, therefore, known as non-adiabatic or inelastic decoherence. The operator in Eq.

2.34 is thus the form of any inelastic scattering process, changing the system's eigenstate probability distribution.

Another important example of a set of Lindblad operators is

$$\hat{L}_\gamma = \sqrt{\frac{\gamma_{nm}}{2}}(|n\rangle\langle n| - |m\rangle\langle m|) \tag{2.37}$$

describing a jump γ_{nm} in phase difference between eigenstates n and m. Inserting this operator, we quickly find that it only affects the off-diagonal elements of ρ as the Lindblad terms do not have any diagonal elements surviving:

$$\frac{d\rho_{nm}}{dt} = -i\Delta\omega_{nm}\rho_{nm} - \gamma_{nm}\rho_{nm}. \tag{2.38}$$

This equation encapsulates any form of pure dephasing, where the coherences decay exponentially with pure dephasing rate γ_{nm}. The Lindblad operator of Eq. 2.37 is thus the form of any elastic scattering process , keeping the system energy the same but decreasing its decoherence.

The Bloch sphere provides a useful illustration of both the elastic and the inelastic decoherence of a two-level system. Using the basis defined by the eigenstates as a computational basis , we can express any density matrix of a two-level system in Bloch sphere coordinates:

$$(r_x, r_y, r_z)_{\text{Bloch}} = (\text{Tr}(\rho\sigma_x), \text{Tr}((\rho\sigma_y), \text{Tr}(\rho\sigma_z)), \tag{2.39}$$

with Tr the matrix trace and σ the Pauli operators. The perfect superposition state then lives on the equator on the Bloch sphere and oscillates with a frequency proportional to $\Delta\omega$ of the two eigenstates. If we add inelastic decoherence, the state on the Bloch sphere spirals to the ground state as illustrated by Fig. 2.10a. If, on the other hand, we add elastic decoherence as in Fig. 2.10b, the state spirals to the exact middle of the Bloch sphere. The state then loses coherence, but the eigenstate population spread remains unchanged.

2.6.2. RELATION BETWEEN DECOHERENCE AND SURFACE SCATTERING PROBLEMS

When electron scattering is the origin of the decoherence, we can make a connection with the introduced scattering problems in section 2.3. For a free electron metal with a single atomic spin state, we can use

$$\begin{aligned}
\hat{H}_{\text{surf}} &= \sum_{s,k} \epsilon_k \hat{c}^\dagger_{s,k} \hat{c}_{s,k} \\
\hat{H}_{\text{sys}} &= \sum_s \epsilon_\sigma d^\dagger_s \hat{d}_s + U d^\dagger_\uparrow d_\uparrow d^\dagger_\downarrow d_\downarrow \\
\hat{V} &= \sum_{s,k} (V d^\dagger_s \hat{c}_{s,k} + \text{h.c.})
\end{aligned} \tag{2.40}$$

for Eq. 2.20. Here, $\hat{c}$ are the fermionic operator of the surface with ϵ_k the corresponding wavenumber k dependent energies. $\hat{d}$ are the fermionic operators of the system. U is the Coulomb interaction we must overcome to place two opposite spins in the system. This model is known as the Anderson impurity model [28].
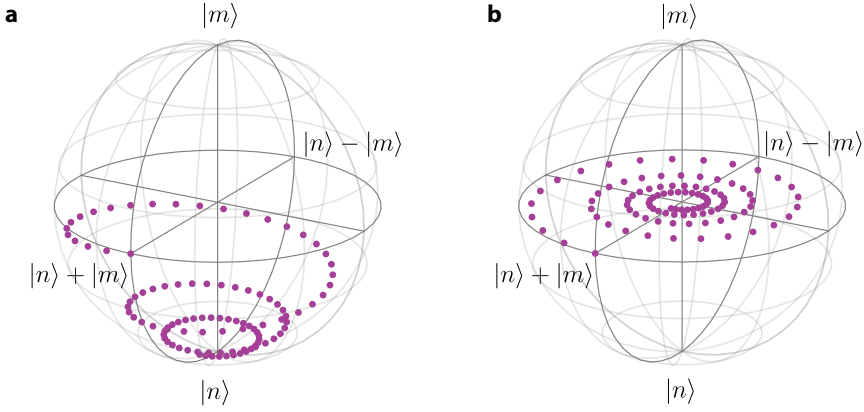
Figure 2.10: Bloch sphere schematic of relaxation and pure dephasing. (a) Schematic of relaxation to the groundstate $|n\rangle$ of the superposition state $|n+m\rangle$. As a function of time, the state spirals both inwards and down, representing, respectively, loss of energy and phase coherence. **(b)** Schematic of pure dephasing of the superposition state $|n+m\rangle$. As a function of time, the state spirals towards the center of the Bloch sphere

Schrieffer and Wolf showed in 1966, through the now well-known Schrieffer-Wolf transformation [29], that in the limit of large charging energy U the self-energy $\hat{\Sigma}$ reduces to

$$\hat{\Sigma}_{\text{Kondo}} = -\frac{J}{4} \sum_{k,k'} \Psi_{k'}^{\dagger} \vec{\sigma} \Psi_k \cdot \Psi_d^{\dagger} \vec{\sigma} \Psi_d, \tag{2.41}$$

where $J = \frac{2|V|^2 U}{\epsilon_s(\epsilon_s+U)}$, $\vec{\sigma}$ the vector of Pauli matrices and Ψ the field operators

$$\Psi_k = \begin{pmatrix} \hat{c}_{k,s} \\ \hat{c}_{k,-s} \end{pmatrix}, \; \Psi_d = \begin{pmatrix} \hat{d}_s \\ \hat{d}_{-s} \end{pmatrix} \tag{2.42}$$

This Σ_{Kondo} is known as the Kondo exchange Hamiltonian [30].

It is often written as

$$\hat{\Sigma}_{\text{Kondo}} = J\vec{S} \cdot \vec{s}, \tag{2.43}$$

where

$$\vec{s} = \sum_{\alpha} \sum_{kk',s} \hat{c}_{s,k}^{\dagger} \hat{\sigma}_{s,-s}^{\alpha} \hat{c}_{-s,k'}, \tag{2.44}$$

with α summing over x, y and z. $\vec{S}$ are the spin operators of the spin system of interest.

To understand the decoherence, we would like to know the time-dependent behavior of $\hat{H}_{\text{sys}} + \Sigma_{\text{Kondo}}$. Here, we can use that the metal interaction is weak, so $V \ll \epsilon_s$. We can thus use $J \ll \epsilon_s$ and solve for the influence of $\hat{\Sigma}_{\text{Kondo}}$ on $\hat{H}_{\text{sys}}$. Under Markov approximation (environment has no memory) and Born approximation (system and environment are separable) , this type of problem where $\hat{\Sigma}$ is of the shape $\sum_{\alpha} A^{\alpha} \otimes B^{\alpha}$ was solved by Bloch and Redfield in 1965 [31]. The resulting equation for $\hat{\rho}_{\text{sys}}$ is

$$\frac{d\rho_{nm,\text{sys}}}{dt} = -i\Delta\omega_{nm}\rho_{nm}(t) + \sum_{kl} R_{nmkj}\rho_{kj}(t), \tag{2.45}$$

2

where for Kondo interaction [32]

$$
\begin{aligned}
R_{nmkj} = \frac{J^2}{\hbar^2} \sum_\alpha \big(&-\delta_{mj} \sum_p S^\alpha_{np} S^\alpha_{pk} g_\alpha(\omega_{pk}) + S^\alpha_{nk} S^\alpha_{jm} g_\alpha(\omega_{nk}) \\
&-\delta_{nk} \sum_p S^\alpha_{jp} S^\alpha_{pm} g^*_\alpha(\omega_{pj}) + S^\alpha_{nk} S^\alpha_{jm} g^*_\alpha(\omega_{mj}) \big)
\end{aligned}
\tag{2.46}
$$

the Bloch-Redfield tensor with α again x, y and z and δ the Kronecker delta's. The g that are appearing here are the correlation functions of the environment operators B

$$
g_\alpha(\omega) = \int_0^\infty \langle s^\alpha(\tau) s^\alpha(0) \rangle e^{-i\omega_{nm}\tau} d\tau
\tag{2.47}
$$

Here, specifically, g is for free electrons and can be related to $\hat{G}_{\text{surf}}$ as defined in Eq. 2.21 [33]:

$$
g_\alpha(\omega) = \int_0^\infty \hat{G}_{\text{surf}}(\omega) f(\omega, T)(1 - f(\omega, T)) e^{-i\omega_{nm}\tau} d\tau
\tag{2.48}
$$

with $f(\omega, T)$ the Fermi distribution function. As such $\hat{H}_{\text{surf}}$ can directly be related to the time-dependent evolution of $\hat{\rho}_{\text{sys}}$.

Often, the system evolves much faster than R_{nmkj}. In this limit, the coherence and populations decouple into Eq. 2.35 with rates [32, 34]

$$
\begin{aligned}
r_{nm} &= \frac{2^2}{\hbar} \sum_\alpha \Re(g_\alpha(\omega_{mn})) |S^\alpha_{mn}|^2 \\
&= \frac{2^2}{\hbar} \frac{\omega_{nm}}{e^{\frac{\omega_{nm}}{k_B T}} - 1} \sum_\alpha |S^\alpha_{mn}|^2
\end{aligned}
\tag{2.49}
$$

and a coherence equation

$$
\frac{d\rho_{nm}}{dt} = -i(\omega_{nm} + \Delta_{nm})\rho_{nm}(t) - (\gamma^{el}_{nm} + \gamma^{inel}_{nm})\rho_{nm}(t),
\tag{2.50}
$$

which is a combination of Eq. 2.36 and Eq. 2.38, with additional energy renormalization Δ_{nm}, which cannot be captured by the Lindblad formalism. The inelastic component is thus equal to

$$
\gamma^{inel}_{nm} = \frac{1}{2} \big(\sum_{k \neq n} r_{nk} + \sum_{k \neq m} r_{mk} \big)
\tag{2.51}
$$

. The elastic decoherence or pure dephasing relates to g as

$$
\begin{aligned}
\gamma^{el}_{nm} &= \frac{1}{\hbar^2} \sum_\alpha \Re\big(g_\alpha(0)\big) (S^\alpha_{mm} - S^\alpha_{nn}) \\
&= \frac{1}{\hbar^2} \sum_\alpha k_B T (S^\alpha_{mm} - S^\alpha_{nn})
\end{aligned}
\tag{2.52}
$$

All in all, we thus see that we can express decoherence as a result of the scattering with free electrons in an equation, which, except for a renormalization of energies, fits the standard Lindblad shape.

	Standing wavefunctions	Atomic wavefunctions
Pseudo-potential	Quantum Espresso [35]	OpenMx [36]
Full potential		KKR [37]

Table 2.1: Limited overview of available DFT methods

2.7. DENSITY FUNCTIONAL THEORY FOR FIELD EMISSION RESONANCES

In the above examples, a suitable phenomenological or effective model could be used to describe the physics of the surface. This is not always the case. Often, the surface Hamiltonian has many degrees of freedom, which all need to be included to evaluate the influence of the surface. An example is field emission resonances on Cu_2N. We thus need to start from first principles: the separate electronic wavefunctions. A way to do so is density functional theory (DFT), in which the ground state of the surface is found self-consistently in mean-field theory by varying the electron density until the energy of the system is minimized. Various theories exist. They differ in their initial guess of the electronic wavefunctions and their description of the atomic potentials by which the wavefunctions are bound.

Regarding the former, some theories start from standing wavefunctions, and others start from atomistic wavefunctions. Regarding the latter, some theories use the full atomic potential, but with a cut-off at a specific distance from the core. Other theories use pseudo-potentials, which do not need a cut-off but approximate the potential far from the core. We present a limited overview of the available methods in table 2.1.

REFERENCES

[1] Farinacci[†], L., Veldman[†], L. M., Willke, P. & Otte, S. Experimental determination of a single atom ground state orbital through hyperfine anisotropy. *Nano Letters* **22**, 8470–8474 (2022).

[2] Binnig, G., Rohrer, H., Gerber, C. & Weibel, E. Surface studies by scanning tunneling microscopy. *Physical review letters* **49**, 57 (1982).

[3] Tersoff, J. & Hamann, D. R. Theory of the scanning tunneling microscope. *Physical Review B* **31**, 805 (1985).

[4] Eigler, D. M. & Schweizer, E. K. Positioning single atoms with a scanning tunnelling microscope. *Nature* **344**, 524–526 (1990).

[5] Yang, K. *et al.* Engineering the eigenstates of coupled spin-1/2 atoms on a surface. *Physical Review Letters* **119**, 227206 (2017).

[6] Ternes, M. Spin excitations and correlations in scanning tunneling spectroscopy. *New Journal of Physics* **17**, 063016 (2015).

[7] Veldman, L. Coherent dynamics of atomic spins on a surface (2024).

2

[8]   Baumann, S. *et al.* Electron paramagnetic resonance of individual atoms on a surface. *Science* **350**, 417–420 (2015).

[9]   Seifert, T. S. *et al.* Longitudinal and transverse electron paramagnetic resonance in a scanning tunneling microscope. *Science advances* **6**, eabc5511 (2020).

[10] Pioro-Ladriere, M., Tokura, Y., Obata, T., Kubo, T. & Tarucha, S. Micromagnets for coherent control of spin-charge qubit in lateral quantum dots. *Applied physics letters* **90** (2007).

[11] Delgado, F. & Lorente, N. A theoretical review on the single-impurity electron spin resonance on surfaces. *Progress in Surface Science* **96**, 100625 (2021).

[12] Reina Gálvez, J., Wolf, C., Delgado, F. & Lorente, N. Cotunneling mechanism for all-electrical electron spin resonance of single adsorbed atoms. *Physical Review B* **100**, 035411 (2019).

[13] Wang, Y. *et al.* Universal quantum control of an atomic spin qubit on a surface. *npj Quantum Information* **9**, 48 (2023).

[14] Nielsen, M. A. & Chuang, I. L. *Quantum computation and quantum information* (Cambridge university press, 2010).

[15] Waintal, X. *et al.* Computational quantum transport. *arXiv preprint arXiv:2407.16257* (2024).

[16] Bogoliubov, N. On the theory of superfluidity. *J. Phys* **11**, 23 (1947).

[17] Istas, M., Groth, C. & Waintal, X. Pushing the limit of quantum transport simulations. *Physical Review Research* **1** (2019).

[18] Pientka, F., Glazman, L. I. & Von Oppen, F. Topological superconducting phase in helical shiba chains. *Physical Review B—Condensed Matter and Materials Physics* **88**, 155420 (2013).

[19] Schneider, L. *et al.* Topological shiba bands in artificial spin chains on superconductors. *Nature Physics* **17**, 943–948 (2021).

[20] Sato, M. & Ando, Y. Topological superconductors: a review. *Reports on Progress in Physics* **80**, 076501 (2017).

[21] Bihlmayer, G., Noël, P., Vyalikh, D. V., Chulkov, E. V. & Manchon, A. Rashba-like physics in condensed matter. *Nature Reviews Physics* **4**, 642–659 (2022).

[22] Kitaev, A. Y. Fault-tolerant quantum computation by anyons. *Annals of physics* **303**, 2–30 (2003).

[23] Stern, A. & Lindner, N. H. Topological quantum computation—from basic concepts to first experiments. *Science* **339**, 1179–1184 (2013).

[24] Nadj-Perge, S. *et al.* Observation of majorana fermions in ferromagnetic atomic chains on a superconductor. *Science* **346**, 602–607 (2014).

[25] Jeon, S. *et al.* Distinguishing a majorana zero mode using spin-resolved measurements. *Science* **358**, 772–776 (2017).

[26] Schneider, L. *et al.* Probing the topologically trivial nature of end states in antiferromagnetic atomic chains on superconductors. *Nature Communications* **14**, 2742 (2023).

[27] Lindblad, G. On the generators of quantum dynamical semigroups. *Communications in mathematical physics* **48**, 119–130 (1976).

[28] Anderson, P. & Clogston, A. Antiferromagnetic contribution to the polarization of free electrons by inner shell spins. *Bulletin of the American Physical Society* **6**, 124 (1961).

[29] Schrieffer, J. R. & Wolff, P. A. Relation between the anderson and kondo hamiltonians. *Physical Review* **149**, 491 (1966).

[30] Kondo, J. Anomalous hall effect and magnetoresistance of ferromagnetic metals. *Progress of Theoretical Physics* **27**, 772–792 (1962).

[31] Redfield, A. G. The theory of relaxation processes. In *Advances in Magnetic and Optical Resonance*, vol. 1, 1–32 (Elsevier, 1965).

[32] Delgado, F. & Fernández-Rossier, J. Spin decoherence of magnetic atoms on surfaces. *Progress in Surface Science* **92**, 40–82 (2017).

[33] Datta, S. *Electronic transport in mesoscopic systems* (Cambridge university press, 1997).

[34] Cohen-Tannoudji, C., Dupont-Roc, J. & Grynberg, G. *Atom-photon interactions: basic processes and applications* (John Wiley & Sons, 1998).

[35] Giannozzi, P. *et al.* Quantum espresso: a modular and open-source software project for quantum simulations of materials. *Journal of physics: Condensed matter* **21**, 395502 (2009).

[36] Ozaki, T. *et al.* User's manual of openmx ver. 3.8 (2016).

[37] Mavropoulos, P. & Papanikolaou, N. The korringa-kohn-rostoker (kkr) green function method i. electronic structure of periodic systems. *Computational Nanoscience: Do It Yourself* **31**, 131–158 (2006).

3

SHORT JUNCTION THEORY FOR DISPERSION OF A YU-SHIBA-RUSINOV CHAIN

The drop hollows out the rock
By frequent falling, not by force

Latin proverb

Rik Broekhoven, Kostas Vilkelis, Michael Wimmer, Antonio Manesco, Anton Akhmerov

Chains of magnetic atoms on s-wave superconductors have Yu-Shiba-Rusinov(YSR) bound states, which hybridize into a bandstructure. STM experiments show this bandstructure can only be described by models with an orbital based approach like density functional theory (DFT). DFT-only methods are, however, computationally expensive.

Here, we present a method based on the method of short junctions to evaluate the effective Hamiltonian of a YSR chain, when only the metal self-energy at the Fermi level is known. It can be used to study the YSR bandstructure as a function of chain parameters such as magnetization.

We benchmark our method with a finite size exact diagonalization of a single orbital model and subsequently use it to evaluate the bandstructure of a atomistic spin-orbit model. Next to the expected Rashba spin-orbit splitting, we find that the YSR bandstructure inherits features of the metal Fermi surface which can only be captured by models with an orbital approach.

3.1. INTRODUCTION

Magnetic atoms on *s*-wave superconductors give rise to Yu-Shiba-Rusinov (YSR) bound states living in the gap of the superconductor. When the atoms are arranged in a chain, the corresponding YSR states can hybridize into YSR bands. Such bands are proposed to become topological superconductors with Majorana zero modes if the spin symmetry is sufficiently broken to cause a topological phase transition. [1–3]. A possible origin of spin symmetry breaking is Rashba spin-orbit coupling, which originates from atomic spin-orbit coupling in the superconductor. As a result of the topological phase transition a gap opens up in the YSR dispersion.

In the past, many scanning tunneling microscopy (STM) experiments have been performed on these systems to observe the presence of Majorana zero modes [4, 5]. However, unambiguously probing Majorana zero modes is difficult. Therefore, a new generation of experiments used quasiparticle interference to reconstruct the band structure and verify, based on it, whether the chain has become a topological superconductor [6, 7]. In contrast to the expectation, the measured YSR dispersion for Mn chains on Nb(110) does not have a gap [6]. Moreover, the dispersion shows multiple YSR bands with each their own orbital character.

The additional details observed in experimental works motivated revisiting the theoretical description of these systems with orbital based approaches, such as density functional theory (DFT) [8, 9]. With this method, it is possible to evaluate the full in-gap dispersion, including all relevant orbitals of the chain. Studying how the dispersion of atomistic models changes with parameters allows for engineering the closing and reopening of the gap.

However, DFT-only methods are computationally demanding, as they include many degrees of freedom and require dense in-gap energy scans to evaluate the YSR dispersion. On top of that, these methods are completely *ab initio*. Thus, they do not allow for changing parameters, such as the magnetization of the chain, after a calculation has finished.

Here, we present a method compatible with *ab initio* calculations to evaluate the effective Hamiltonian of translational invariant chains. We use scattering theory in the short junction limit to combine the self-energy of the superconductor with the chain Hamiltonian. The in-gap spectrum depends only on the self-energy at the Fermi level. So we only require the self-energy at a single energy. Moreover, we deliberately eliminate modes of the superconductor that do not couple with the chain and hereby further decrease the computational costs of our method. The method works for both orthogonal and non-orthogonal basis sets.

We benchmark our method by showing that its eigenvalues coincide with simulations of finite-size systems much larger than the coherence length. We subsequently analyze a model with *s*- and *p*-orbitals for the superconductor coupled to a single spin. Starting from atomistic spin-orbit coupling, we observe Rashba splitting at the metalic surface, which opens up a gap in the YSR dispersion. Moreover, we observe that the dispersion inherits features of the metal's Fermi surface, which are not captured by standard toy models of YSR chains. Finally, we change the magnetization in the evaluated effective Hamiltonian to study the expected topological quantum phase transition.
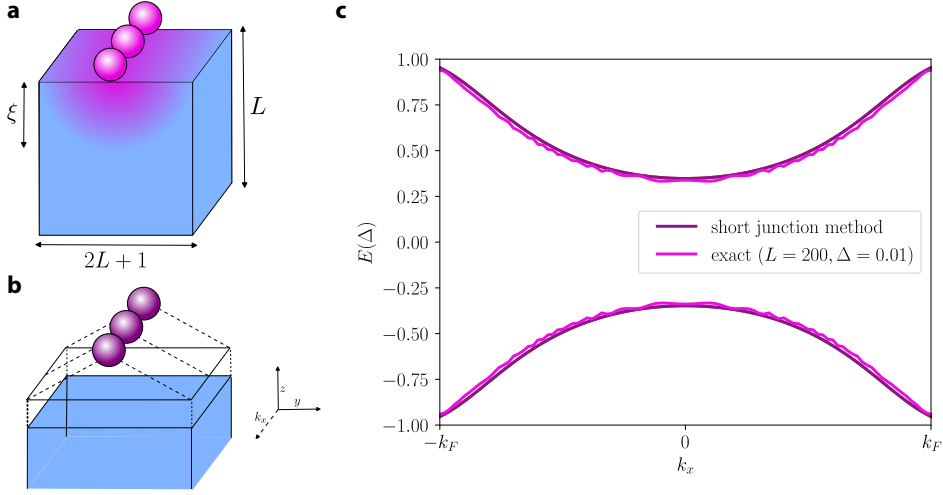
Figure 3.1: Short junction method. Comparison of the dispersion relations of **(a)** a ferromagnetic infinite chain on a finite size superconductor with length L and **(b)** a ferromagnetic infinite chain in the short junction limit coupled through virtual leads to a semi-infinite superconductor, **(c)** shows the 1D dispersions for the model as defined by Eq. 3.32 $\Delta = 0.01\,t$, $\mu = 0.5\,t$ evaluated for geometry **(a)** and using the short junction method for geometry **(b)**.

3.2. METHOD

We start from a tight-binding Hamiltonian of a chain of magnetic atoms on an s-wave superconductor with H_l the Hamiltonian of the superconducting lead, H_c the Hamiltonian of the chain and V_{cl} the hopping between the lead and the chain. We terminate the superconductor in the z-direction and take the chain to extend in the x-direction. The Hamiltonian terms can then be further expressed as

$$H = H_l + H_c + V_{cl} \tag{3.1}$$

$$H_l = \sum_{x,y=-\infty}^{\infty} \left(\sum_{z=-\infty}^{-1} H_0^l |x,y,z\rangle \langle x,y,z| + H_0^s |x,y,0\rangle \langle x,y,0| \right. \tag{3.2}$$

$$+ \sum_{z=-\infty}^{0} \left(V_x^l |x-1,y,z\rangle \langle x,y,z| \right.$$

$$+ V_y^l |x,y-1,z\rangle \langle x,y,z|]$$

$$\left. + V_z^l |x,y,z-1\rangle \langle x,y,z| + h.c.) \right),$$

$$H_c = \sum_{x=-\infty}^{\infty} H_0^c |x,0,1\rangle \langle x,0,1|, \tag{3.3}$$

$$V_{cl} = \sum_{x=-\infty}^{\infty} (V |x,0,0\rangle \langle x,0,1| + h.c.). \tag{3.4}$$

Here, x, y, z are the spatial positions on a square lattice and $H_0^{c/l/s}$ is the onsite Hamiltonian of, respectively, the chain, the superconductor lead, and the lead unit cell of the surface termination. As a result of unpaired electrons at the surface $H_0^s \neq H_0^l$. $V_{x/y/z}^l$ is the hopping of the lead along each spatial direction. Finally, V is the hopping between a surface cell of the superconductor and an atom of the chain.

The YSR bound state wave functions Ψ_{YSR} are the states of the superconductor that scatter with the chain back to itself. We can divide the states of the superconductor in the propagating quasi-particle modes moving towards the chain (ϕ_{in}) and the modes propagating away from the chain (ϕ_{out}). At the position of the surface termination, the state of the superconductor can thus be written as [10]

$$\psi_s = q^{\text{in}}\phi_{s,\text{in}} + q^{\text{out}}\phi_{s,\text{out}}, \tag{3.5}$$

with q^{in} and q^{out} the amplitudes of respectively the incoming and outgoing modes. We furthermore define s as the unitary scattering matrix relating the normal metal part of q^{in} to q^{out}

$$q^{\text{out}} = s q^{\text{in}}. \tag{3.6}$$

r_A is the corresponding Andreev reflection matrix for the superconducting modes. The YSR bound state condition in the Bogilobov-de-Gennes (BdG) quasi-particle mode basis then is[11]

$$\alpha(E)\begin{pmatrix} s & 0 \\ 0 & s^T \end{pmatrix}\begin{pmatrix} 0 & r_A \\ r_A & 0 \end{pmatrix}\Psi_{YSR} = E\Psi_{YSR}. \tag{3.7}$$

This equation is under the additional Andreev approximation that the Fermi wavelength λ_F is much smaller than the coherence length ξ. This means that wavefunction matching at the normal superconductor interface becomes an energy-dependent factor $\alpha(E)$ [12].

3.2.1. SHORT JUNCTION LIMIT
The accumulated dynamical phase in the impurity is negligible because typical coherence lengths $\xi \sim 100$nm are much larger than the impurity site ($a \sim 1$ Å). Therefore, short-junction approximation applies, and the Andreev spectrum of Eq. 3.7 then simplifies to[11]:

$$AA^{\dagger}\Psi_{YSR} = \left(\frac{E}{\Delta}\right)^2 \Psi_{YSR}, \tag{3.8}$$

with $A = \frac{1}{2}(r_A s - s^T r_A)$. Note that the energy E scales with Δ, meaning that all in-gap states are gap-independent in this limit. Assuming perfect Andreev reflection, so r_A diagonal in the electron-hole block with scalars $|r_A| = 1$, the Andreev reflection drops out of the spectrum and the only unknown is the energy-independent normal metal scattering s.

3.2.2. VIRTUAL LEADS: MODE REDUCTION
Because the superconductor has a large Fermi surface, the total transmission between the superconductor and the impurity is bounded by the number of orbitals in the impurity. Therefore, we simplify the normal state scattering problem by decomposing it into a scattering matrix from the impurity chain to the surface cell (s_c) and a scattering matrix from the surface cell to the lead (s_s). Each describes scattering with current conserving virtual

leads at the superconductor-chain interface (see Fig. 3.1). We single value decompose the superconductor-chain hopping $V = U_A U_B^\dagger$ into a hopping U_A belonging to s_c and a hopping U_B belonging to s_s. We have freedom in choosing the U_A and U_B but pick it such that all the non-trivial degrees of freedom of the hopping appear in U_B. We arrive at

$$V = IV_c^\dagger, \tag{3.9}$$

where V_c is now of shape $N_c \times M$ and I is of shape $N_l \times M$ with $N_{c/s}$ the size of $H_{c/s}$ and M of rank V.

When we furthermore consider V_c to be approximately time-reversal symmetric (TRS), we find that the full scattering problem of s_s becomes time-reversal symmetric, making it skew-symmetric $s_s = -s_s^T$. We can now do the following cosine-sine decomposition [13] respecting skew-symmetry:

$$s_s = \begin{pmatrix} U_{vl} & 0 \\ \hline 0 & U_s \end{pmatrix} \begin{pmatrix} \tilde{r} \otimes \sigma_y & \tilde{t} \otimes \sigma_y & 0 \\ \hline -\tilde{t} \otimes \sigma_y & \tilde{r} \otimes \sigma_y & 0 \\ 0 & 0 & I \otimes \sigma_y \end{pmatrix} \begin{pmatrix} U_{vl} & 0 \\ \hline 0 & U_s \end{pmatrix}^T, \tag{3.10}$$

where $\tilde{r}$, $\tilde{t}$ are diagonal real-valued matrices that quantify reflectance/transmission at the virtual/physical lead interface and U_{vl} and U_s unitary matrices. Note that if we apply U_s to the spectrum as in Eq. 3.8 we find

$$\begin{aligned} A &= U_s(s - s^T)U_s^T \\ AA^\dagger &= U_s^T(s - s^T)(s - s^T)^\dagger U_s^*, \end{aligned} \tag{3.11}$$

where for the last equality we use that U is unitary. Using that the spectrum does not change by unitary transform and $U_s^T U_s^* = I$ we can now see that U_s drops out of the spectrum. This is a direct consequence of the lead fully respecting time-reversal symmetry. We can thus evaluate $\tilde{s}$ and treat it as s. We evaluate $\tilde{s}$ by making use of current conservation. The modes of the lead and chain scattering problems must be the same. As a result, we can combine the two scattering problems by solving the corresponding Dyson equation. We find

$$s = (\begin{pmatrix} \tilde{r} & 0 \\ 0 & I \end{pmatrix} - \begin{pmatrix} \tilde{t}((\tilde{s}_c \otimes \sigma_y)^{-1} - \tilde{r})^{-1}\tilde{t} & 0 \\ 0 & 0 \end{pmatrix}) \otimes \sigma_y, \tag{3.12}$$

where $s_c = U_{vl}(\tilde{s}_c \otimes \sigma_y)U_{vl}^T$.

The only non-trivial eigenvalues (norm < 1) are in the first block meaning that, as suspected, the computation can be significantly reduced to be of the size of the norm of V. We thus reduce the scattering matrix to

$$\begin{aligned} s_{\text{red}} &= (\tilde{r} - \tilde{t}((\sigma_y \otimes \tilde{s}_c)^{-1} - \tilde{r})^{-1}\tilde{t}) \otimes \sigma_y \\ &= (\tilde{r} - \tilde{t}U_{vl}^T(s_c^{-1} - r_{vl})U_{vl}\tilde{t}) \otimes \sigma_y. \end{aligned} \tag{3.13}$$

Because $\tilde{t} = \sqrt{1 - \tilde{r}^2}'$ and the reflection at the virtual lead r can be decomposed as $U_{vl}\tilde{r}_{vl}U_{vl}^T$ the only remaining unknowns are r_{vl} and s_c.

3.2.3. VIRTUAL LEADS: SEPARATE SCATTERING PROBLEMS

We can solve for r_{vl} and s_c by evaluating the corresponding scattering problems explicitly in the basis $(\bar{\psi}_c, \bar{\psi}_l)$ we defined by V_c:

$$\bar{\psi}_c = \psi_c \tag{3.14}$$

$$\bar{\psi}_s = V_c^\dagger \psi_s, \tag{3.15}$$

where $\psi_{c/s}$ are the orbital wavefunctions of the chain and metal lead, respectively. The scattering matrices couple the in and out going modes $\bar{\phi}_{c/s,\text{in/out}}$ of $\bar{\psi}_{c/s}$ together as

$$\bar{\psi}_{c/s} = \bar{\phi}_{c/s,\text{out}} s_c - \bar{\phi}_{c/s,\text{in}} \tag{3.16}$$

$$\bar{\psi}_{c/s} = \bar{\phi}_{c/s,\text{in}} r_{vl} - \bar{\phi}_{c/s,\text{out}}. \tag{3.17}$$

These modes are the virtual modes of the virtual leads. They must obey current conservation and time-reversal symmetry. In this basis the current expectation value becomes

$$\langle \psi | I | \psi \rangle = \langle \psi | \begin{pmatrix} -iV & 0 \\ 0 & iV \end{pmatrix} | \psi \rangle = \begin{pmatrix} \bar{\psi}_c & \bar{\psi}_s \end{pmatrix} \sigma_y \begin{pmatrix} \bar{\psi}_c \\ \bar{\psi}_s \end{pmatrix}. \tag{3.18}$$

Virtual modes that obey time-reversal symmetry and current conservation are then

$$\bar{\phi}_{c,\text{in}} = \frac{1}{\sqrt{2}}, \qquad \bar{\phi}_{s,\text{in}} = -\frac{i}{\sqrt{2}} \tag{3.19}$$

$$\bar{\phi}_{c,\text{out}} = \frac{i\sigma_y}{\sqrt{2}}, \qquad \bar{\phi}_{s,\text{out}} = \frac{\sigma_y}{\sqrt{2}}. \tag{3.20}$$

Here, the σ_y are to respect TRS. We then arrive at the following two scattering equations

$$\begin{pmatrix} H_0^c & i\sigma_y \\ -1 & \sigma_y \end{pmatrix} \begin{pmatrix} \psi_c \\ s_c \end{pmatrix} = \begin{pmatrix} 1 \\ -i \end{pmatrix} \tag{3.21}$$

$$\begin{pmatrix} H_0^{s,\text{eff}} & -V_c \\ -V_c^\dagger & 1 \end{pmatrix} \begin{pmatrix} \psi_s \\ r_{vl} \end{pmatrix} = \begin{pmatrix} V_c \sigma_y \\ i\sigma_y \end{pmatrix}, \tag{3.22}$$

, where in the latter equation $H_{s,\text{eff}}$ is the effective superconductor surface cell Hamiltonian as a result of the bulk of the superconductor.

We can solve these equations and find Fisher-Lee relationships for s_c and r_{vl}: [10]

$$s_c = i\sigma_y (1 + iH_c)^{-1}(1 - iH_c) \tag{3.23}$$

$$r_{vl} = -i\sigma_y (1 + i\Sigma_0))^{-1}(1 - i\Sigma_0), \tag{3.24}$$

. Here, we have substituted the Fermi level normal metal self-energy Σ_0 as we can write it as

$$\Sigma_0 = V_c (H_0^{s,\text{eff}})^{-1} V_c^\dagger = V_c G_0 V_c^\dagger. \tag{3.25}$$

G_0 is the Fermi level Greens function at the position of the surface termination. We can obtain G_0 and thus Σ_0 from solving a standard scattering problem of a Hamiltonian coupled to a lead.

3.2.4. SCATTERING THEORY FOR SURFACE PHYSICS

In order to ensure that the system we model is much larger than the coherence length, Σ_0 has to be the self-energy of the full translational invariant metal [14]. We start with evaluating the Fermi level Green's function G_0 of the metal surface consisting of H_l and surface termination of the metal H_s. Because of the translational invariance of the metal in two of the three coordinates, we can recognize this problem as a 1D lead $H_l(k_x, k_y, z)$ coupled to a scattering region $H_s(k_x, k_y, z = 0)$. Choosing z to be the direction breaking translational invariance, we can evaluate

$$H_l(k_x, k_y, z) = \int_{-\infty}^{\infty} \int_{-\infty}^{\infty} H_l(x, y, z) e^{i(k_x x + k_y y)} dx dy. \tag{3.26}$$

We can solve the corresponding 1D scattering problem using *kwant* [15] to find $G_0(k_x, k_y, z = 0)$. The self-energy of the metal at the position of the chain is then equal to the Shor complement of the metal lead:

$$\Sigma_0(k_x, y = 0, z = 0) = \int_{-\pi}^{\pi} V(k_x, k_y) G_0(k_x, k_y, z = 0) V(k_x, k_y)^{\dagger} dk_y, \tag{3.27}$$

with V the non-translational invariant hopping in the y-direction between the metal and the chain.

Knowing Σ_0, we can solve for s_c and r_{vl} in eq. 3.24 and eq. 3.23, insert their result in eq. 3.13 to find the overall scattering matrix, and finally solve the short junction eq. 3.8 for the YSR dispersion.

3.2.5. NON-ORTHOGONAL BASIS

We now generalize our method to non-orthogonal basis sets to deal with Hamiltonians derived from *ab initio* calculations. It is defined by an overlap matrix not equal to the identity $D_{ij} = \langle \phi_i | | \phi_j \rangle$ as well as a transformation P to a corresponding orthogonal basis ψ:

$$\psi_i = \sum_j P_{ij}^* \phi_i. \tag{3.28}$$

Transformation from an operator M in the orthogonal basis to an operator $\tilde{M}$ in the non-orthogonal basis follows in general

$$\tilde{M} = DP^{\dagger} MPD \tag{3.29}$$

The corresponding operator eigenvalue equation is

$$\tilde{M}\psi = ED\phi. \tag{3.30}$$

In the current presented method, there are two places where we might expect a change when there is a non-orthogonal overlap matrix. First of all in the short junction part. This part is based on solving the scattering problems of Eq. 3.21 and 3.22 in the basis as defined by Eq. 3.18. Inserting the non-orthogonal equivalent of the current operator in the current expectation equation we arrive at

$$\langle \phi | DP^{\dagger} IPD | \phi \rangle = \langle \phi | \begin{pmatrix} -i\tilde{V} & 0 \\ 0 & i\tilde{V} \end{pmatrix} | \phi \rangle = \begin{pmatrix} \phi_c & \phi_l \end{pmatrix} \sigma_y \begin{pmatrix} \phi_c \\ \phi_l \end{pmatrix}, \tag{3.31}$$

where we can again decompose the hopping as Eq. 3.9. As this equation takes the same shape as for an orthogonal basis the same holds for the scattering problems and their corresponding Fisher-Lee relations ships Eq. 3.23 and 3.24. The short junction part thus stays the same.

The other part where the orthogonal basis might be different is the evaluation of the self-energy at the Fermi level. It is found by solving the Greens function of the lead in the non-orthogonal basis. The corresponding eigenvalue equation follows Eq. 3.30 which for $E = 0$ takes the same shape of the orthogonal basis. So also the self-energy at Fermi can be calculated in the same manner as in section 3.2.4.

We conclude that in the regime where the short junction method holds the YSR dispersion is approximately independent of the overlap matrix D.

3.3. SINGLE ORBITAL MODEL

We demonstrate the working of the method using a single orbital model of YSR dispersion. We model the lead as

$$
\begin{aligned}
H_0^l = H_0^s &= \mu\sigma_0 \\
V_{x/y/z}^l &= -t\sigma_0,
\end{aligned}
\tag{3.32}
$$

where σ are the Pauli matrices, t is the hopping and μ the onsite potential. For the surface termination, we use the same Hamiltonian. We model the chain as well as a tight-binding system but now with a Zeeman term B for the spins:

$$
H_0^c = \mu_c\sigma_0 + B\sigma_z.
\tag{3.33}
$$

The chain and bulk are coupled with a simple single-order hopping

$$
V = -t_c\sigma_0.
\tag{3.34}
$$

We find the corresponding effective Hamiltonian and plot the dispersion relation in Fig. 3.1c. We compare the result with the dispersion coming from the exact diagonalization of a finite geometry of size $L = 200$ in y- and z-direction, which is still translational invariant along the direction of the chain. In order to ensure that we can apply the short junction theory, we use a BdG gap of $0.01t$ for this exact calculation, which corresponds to a gap of 1 meV for typical $t = 0.1$ eV. We can see that the dispersion coming from the short junction method follows the same trend as the dispersion coming from the finite-size system, while being more smooth. Our method thus agrees with the exact solution while not having additional finite-size effects.

3.3.1. SCALING WITH GAP SIZE

We furthermore compare the YSR eigenenergies of finite-size calculations E_{finite} to the short junction method $E_{\text{short junction}}$ in Fig. 3.2(a) as a function of L/ξ. We observe a non-monotonic behavior of $\epsilon = |E_{\text{finite}}(k = 0) - E_{\text{short junction}}(k = 0)|/\Delta$ when $\xi \gg L$ due to finite-size effects. Moreover, Andreev approximation breaks when $\xi \lesssim \lambda_F$, resulting in larger ϵ. Away from these two extreme cases, we observe a monotonic behavior of
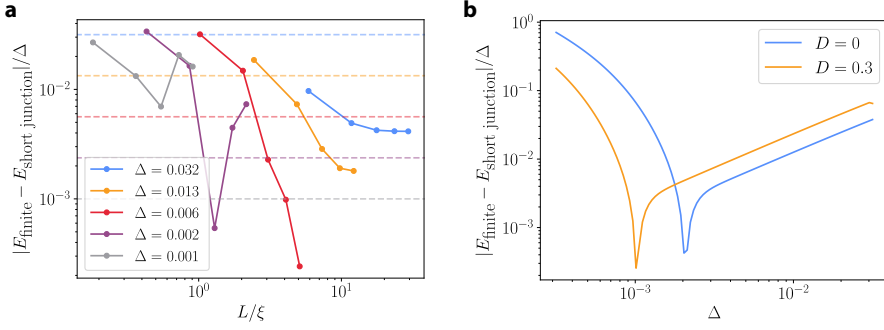
Figure 3.2: Benchmark of the short junction method. (a) Δ scaled norm of the difference between YSR energies obtained using the short junction method and those obtained using diagonalization of a finite system Hamiltonian with increasing length L from 50 to 200 and parameters $\mu = 0.5$, $\mu_c = 0$, $t_c = 1$, and $B = 1$ all expressed in the hopping t. All is evaluated for $k = 0$ and plotted logarithmically for various Δ. Dotted lines is the expected error $\Delta/2\mu$ of the short junction method, **(b)** Δ scaled norm of the difference between YSR energies obtained using the 2D short junction method and those obtained using 2D finite size calculation of length $L = 2000$ plotted next to norm of the energy difference of short junction method with the same finite size calculation but then with overlap $D^t = 0.3$. All are plotted logarithmically such that the expected linear scaling of the difference is visible.

ϵ. Finally, because the lowest-order correction to short-junction approximation is $\sim \Delta^2/2\mu$, we conclude that the short-junction approximation performs better than finite-size calculations as long as Andreev approximation holds.

3.3.2. NON-ORTHOGONAL BASIS

Finally, we test that the short junction method is approximately independent of non-orthogonal overlap D of the eigenstates as was concluded in section 3.2.5. In order to mostly disentangle the effect of an overlap from finite size effects, we need to simulate larger finite structures. This would become too computationally expensive for 3D structures. So, we perform this test on a 2D model. The 2D model is the same as Eq. 3.32 but then without the y-direction, i.e. the direction perpendicular to the chain, and with an additional hopping term $D^V_{x,z}$ coming from the overlap with D^t the magnitude of the corresponding overlap:

$$
\begin{aligned}
H_{l,\,2D} = H_{s,\,2D} &= \mu\sigma_0, \\
V^{l,\,2D}_{x,z} &= -t\sigma_0 \\
D^V_{x,z} &= D^t\sigma_0
\end{aligned}
\tag{3.35}
$$

The integral of Eq. 3.27 is removed for the overall computational scheme. The overlap contribution is linear in energy (3.30) so the additional error due to finite overlap scales in first order as $D^t\frac{\Delta^2}{2\mu}$.

We demonstrate the scaling of the error again with $k = 0$. The difference now has three contributions: the Andreev approximation error, the error because of finite D^t, and the remaining general finite size error, $F(E,\Delta)$, for small Δ. In total it can be written as $\epsilon \propto (c_1 E\frac{\Delta^2}{2\mu} + c_2 D^t E\frac{\Delta^2}{2\mu} + F(\Delta, E))$. We expect the error thus to scale linearly with Δ and to

shift along the Δ axis with D^t in the region where $F(\Delta, E)$ is negligible. Fig. 3.2B confirms this expectation. For $\xi \lesssim L$ the logarithmic error ϵ/Δ between the short junction method and finite size calculations of size $L = 2000$ scales linearly and shifts with D^t. For $L \lesssim \xi$, ξ becomes too big, leading to additional contribution of $F(E, \Delta)$. As a result ϵ stops to scale linearly here. Still, as expected, ϵ shifts approximately along Δ with D^t.

Overall, the error remains of the size of the Andreev approximation error. It is thus indeed justified to neglect the influence of finite D.

3.4. ATOMIC SOC

As a next showcase of our method, we examine a model with s and p orbitals and atomistic spin-orbit coupling in the p-orbitals. We use

$$H_{\text{soc}} = \alpha \boldsymbol{L} \cdot \boldsymbol{\sigma} \tag{3.36}$$

as Hamiltonian for atomistic spin-orbit coupling. Here, $\boldsymbol{\sigma}$ are the Pauli matrices and $\boldsymbol{L}$ are the orbital momentum operators for orbital momentum equal to 1. A natural basis to express them is in the eigenvalues m_L of the projection on z. We prefer the p-orbital basis however as that diagonalizes the other terms of the tight-binding Hamiltonian. The unitary that relates the two bases is

$$U_{\text{soc}} = \begin{array}{c|ccc} & m_L = 1 & m_L = 0 & m_L = -1 \\ \hline p_x & -i & 0 & -i \\ p_y & 1 & 0 & -1 \\ p_z & 0 & 1 & 0 \end{array} \quad . \tag{3.37}$$

We furthermore include a general onsite term, direct hopping between same oriented p-orbitals and sp-hopping to mix the p-orbitals. The total bulk Hamiltonian then is

$$\begin{aligned} H_0^l &= \sum_l \mu \sigma_0 + U_{\text{soc}} H_{\text{soc}} U_{\text{soc}}^\dagger, \\ H_0^s &= \sum_l (\mu + \Delta\mu)\sigma_0 + U_{\text{soc}} H_{\text{soc}} U_{\text{soc}}^\dagger, \\ V_a^l &= (-t_{p_a,p_a} - t_{p_a,s} + t_{s,p_a})\sigma_0, \end{aligned} \tag{3.38}$$

with $a = x$, y, z and μ_l and t_{l_1,l_2} respectively the onsite term and hopping for orbitals s, p_x, p_y and p_z. We have also used that all p-orbitals are anti-symmetric so sp- and ps-hopping have a sign difference. To correctly simulate the termination of the surface, H_s must be of the same shape as H_l but with surface potential $\mu + \Delta\mu$ representing the surface excess of electrons.

The termination of the surface combined with sp-hopping causes the orbitals at the surface to mix. The result is a non-zero angular momentum at the surface. H_{soc} can couple to this angular momentum, which in turn leads to Rashba splitting at the surface[16, 17].

$$H_{\text{Rashba}} = i\alpha_R \mathbf{k} \times \boldsymbol{\sigma} \tag{3.39}$$

In Fig. 3.3A we plot on a logarithmic color scale the surface spin contrast of the k_x-dependent density of states as achieved through

$$\mathscr{S}_y = \text{Tr}\left[S_y \text{Im}\left(G(k_x, k_y) \right) \right] \tag{3.40}$$

where S_y is the spin 1/2 operator to rotate the spin to y so that according to eE. 3.39 any Rashba splitting must be visible in k_x. We can indeed see that the splitting is only present in the x part of the spectrum. We thus conclude that we are able to simulate Rashba spin-orbit coupling starting from bulk spin-orbit coupling.

We combine this result with a chain as defined by Eq. 3.33 and use

$$V = -t_{p_z,s}\sigma_0 \tag{3.41}$$

as hopping, because the overlap with the p_z-orbital is the biggest. 3.3B shows the corresponding YSR dispersion as a function of α and B. When we increase B there is a quantum phase transition with the gap closed at $k = 0$ for $B = 0.48$. Other Fermi crossings are present for $\alpha = 0$ but are gapped out as expected for finite α. We can thus correctly capture bulk physics (H_{soc}) in the YSR dispersion.

Note as well that already for this simple model with s and p-orbitals the expected YSR dispersion is highly non-trivial showing features in the range of just a few k points. It is a direct result of the non-trivial surface spin density of the Fermi surface. We thus conclude that the YSR dispersion in general absorbs the complexity of the bulk Fermi surface meaning that a correct treatment of the bulk is necessary to model YSR dispersion. Toy models do not capture these features.
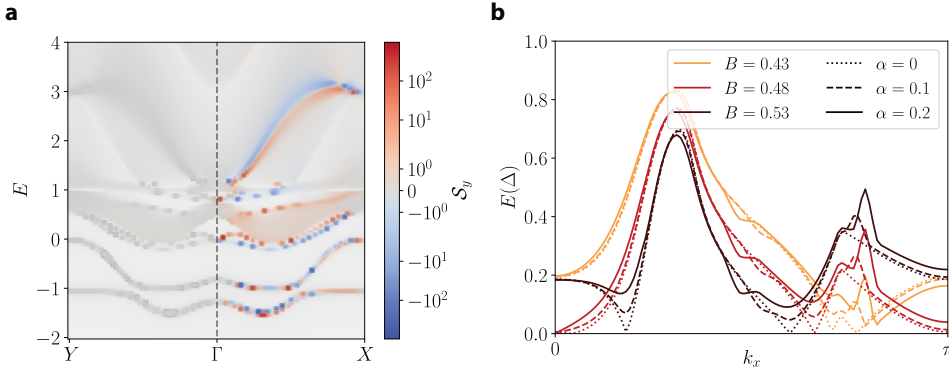
Figure 3.3: Atomistic spin-orbit coupling. (a) Logarithmic difference between y-projected surface spin density of states of the atomistic spin-orbit model with $\alpha = 0.2$, $\mu_c = 0$, $\mu = -1$, $\Delta\mu = 2$ and $t_c = 1$ all in units of t. **(b)** In-gap YSR dispersion as a function of atomic spin-orbit of the bulk α and field B. We choose the values of B such that a quantum phase transition is visible for $B = 0.48$. Furthermore, we use $t_c = 1$.

3.5. CONCLUSIONS

We have presented a method to evaluate the dispersion of YSR states based on the theory of short junctions. The theory is guaranteed to not suffer from finite size effects, interfaces well with *ab initio* calculations as it works for a non-orthogonal basis, and allows for changing of parameters without the need for additional *ab initio* calculations. On top of that, the method only needs the self-energy at the Fermi level to evaluate the full in-gap band structure.

The method outperforms finite size calculations in terms of accuracy as expected for systems that are smaller than the coherence length. As the method is based on Andreev approximation it does have an error scaling as $\frac{\Delta^2}{2\mu}$, but for realistic gap sizes this error is negligible.

Our method can also capture the presence of Rashba splitting at the surface for a model with atomic spin-orbit coupling and $s-$ and p-orbitals. The corresponding YSR dispersion has features that do not appear in dispersions coming from toy models. This shows that the dispersion of YSR chains in general depends heavily on the complexity of the Fermi surface of the metal the chains are placed upon.

The presented method is expected to be particularly fruitful when coupled with *ab initio* calculations to study YSR dispersion when many orbitals are involved.

3.6. CODE AND DATA AVAILABILITY

All research data and code supporting the findings described in this chapter are available in 4TU.ResearchData at: DOI 10.4121/c773957e-b628-4962-817a-9a213bdf06db.

3.7. AUTHOR CONTRIBUTIONS

AA and MW initiated and supervised the project. KV and AA developed the short junction theory and accompanying code. RB, KV and AM developed the Green's function part of the code. RB and AM performed the simulations. RB wrote the paper, with input from all authors.

REFERENCES

[1] Choy, T.-P., Edge, J. M., Akhmerov, A. R. & Beenakker, C. W. Majorana fermions emerging from magnetic nanoparticles on a superconductor without spin-orbit coupling. *Physical Review B—Condensed Matter and Materials Physics* **84**, 195442 (2011).

[2] Pientka, F., Glazman, L. I. & Von Oppen, F. Topological superconducting phase in helical shiba chains. *Physical Review B—Condensed Matter and Materials Physics* **88**, 155420 (2013).

[3] Nadj-Perge, S. *et al.* Observation of majorana fermions in ferromagnetic atomic chains on a superconductor. *Science* **346**, 602–607 (2014).

[4] Jeon, S. *et al.* Distinguishing a majorana zero mode using spin-resolved measurements. *Science* **358**, 772–776 (2017).

[5] Schneider, L. *et al.* Precursors of majorana modes and their length-dependent energy oscillations probed at both ends of atomic shiba chains. *Nature nanotechnology* **17**, 384–389 (2022).

[6] Schneider, L. *et al.* Topological shiba bands in artificial spin chains on superconductors. *Nature Physics* **17**, 943–948 (2021).

[7] Schneider, L. *et al.* Probing the topologically trivial nature of end states in antifer-romagnetic atomic chains on superconductors. *Nature Communications* **14**, 2742 (2023).

[8] Nyári, B. *et al.* Relativistic first-principles theory of yu-shiba-rusinov states applied to mn adatoms and mn dimers on nb (110). *Physical Review B* **104**, 235426 (2021).

[9] Crawford, D. *et al.* Majorana modes with side features in magnet-superconductor hybrid systems. *npj Quantum Materials* **7**, 117 (2022).

[10] Waintal, X. *et al.* Computational quantum transport. *arXiv preprint arXiv:2407.16257* (2024).

[11] van Heck, B., Mi, S. & Akhmerov, A. R. Single fermion manipulation via supercon-ducting phase differences in multiterminal josephson junctions. *Phys. Rev. B* **90**, 155450 (2014).

[12] Beenakker, C. Universal limit of critical-current fluctuations in mesoscopic joseph-son junctions. *Physical review letters* **67**, 3836 (1991).

[13] Beenakker, C. W. J. Random-matrix theory of quantum transport. *Reviews of Modern Physics* **69**, 731–808 (1997).

[14] Istas, M., Groth, C. & Waintal, X. Pushing the limit of quantum transport simulations. *Physical Review Research* **1** (2019).

[15] Groth, C. W., Wimmer, M., Akhmerov, A. R. & Waintal, X. Kwant: a software package for quantum transport. *New Journal of Physics* **16**, 063065 (2014).

[16] Skolasinski, R. Topology, magnetism, and spin-orbit: A band structure study of semiconducting nanodevices (2018).

[17] Bihlmayer, G., Noël, P., Vyalikh, D. V., Chulkov, E. V. & Manchon, A. Rashba-like physics in condensed matter. *Nature Reviews Physics* **4**, 642–659 (2022).

3

4

LIFETIME OF CONFINED VACUUM RESONANCES

Rasa Rejali, Laetitia Farinacci, David Coffey, **Rik Broekhoven**, Jeremie Gobeil, Yaroslav. M. Blanter and Sander Otte

Atomically engineered artificial lattices are a useful tool for simulating complex quantum phenomena, but have so far been limited to the study of Hamiltonians where electron-electron interactions do not play a role—but it's precisely the regime in which these interactions do matter where computational times lend simulations a critical advantage over numerical methods. Here, we propose a new platform for constructing artificial matter that relies on the confinement of field-emission resonances, a class of vacuum-localized discretized electronic states. We use atom manipulation of surface vacancies in a chlorine-terminated Cu(100) surface to reveal square patches of the underlying metal, thereby creating atomically precise potential wells that host particle-in-a-box modes. By adjusting the dimensions of the confining potential, we can access states with different quantum numbers, making these patches attractive candidates as quantum dots or artificial atoms. We demonstrate that the lifetime of electrons in these engineered states can be extended and tuned through modification of the confining potential, either via atomic assembly or by changing the tip-sample distance. We also demonstrate control over a finite range of state-filling, a parameter which plays a key role in the evolution of quantum many-body states. We model the transport through the localized state to disentangle and quantify the lifetime-limiting processes, illustrating the critical dependency of the electron lifetime on the properties of the underlying bulk band structure. The interplay with the bulk bands gives rise to negative differential resistance.

4.1. INTRODUCTION

Artificial lattices serve as quantum simulators for realizing and studying fundamental properties of real materials, with the advantage that the relevant interactions can be precisely controlled. While different experimental approaches, such as using ultra-cold atoms [2], optical lattices [3, 4], or trapped ions [5], have been successfully implemented in the study of artificially constructed systems, atom manipulation casts the scanning tunneling microscope (STM) as a particularly appealing platform: the scanning probe framework uniquely allows for creating and characterizing the electronic properties of 2D artificial matter on the atomic scale [6]. Typically, atomic impurities are patterned to construct a potential landscape that mimics a specific physical system, with the aim of studying model Hamiltonians. This approach has led to the realization of a wide range of novel states in, for instance, Dirac materials, like the Lieb lattice [7, 8] and artificial graphene [9, 10], as well as higher order topological insulators [11, 12], among others [13–17]. These studies offer rare insight into the parameters that govern the electronic behaviour of these systems, but are restricted by the short electron lifetime of the constituent artificial atoms to the limiting case in which electron-electron interactions do not play a role. Additionally, short electron lifetimes limit the available energy resolution; the most popular STM approach so far, which relies on confining surface states, lacks flexibility in tuning this parameter [18–20].

Here, we explore a new platform for realizing artificial lattices, based on confining field-emission resonances (FERs): a class of quantized electronic states localized in the vacuum, between the surface and the probe tip, that arise in the high bias regime, i.e. exceeding the sample work function. We show that confining potentials can be engineered to enable the study of states with different orbital character [10, 21, 22], with precise control over the energy and quantum numbers of the states. We study the electron lifetime of these states, and demonstrate that we can finely tune it—and consequently, to some extent, the average occupation—by adjusting the tip-height or patch dimensions. The ability to tune the lifetime and occupation of artificial atoms is a critical first step towards simulating many-body quantum states driven by electron-electron interactions. We also observe specific voltage-current characteristics, namely negative differential resistance, which are analogous to those of resonant tunneling diodes [23], making the confined FERs also suitable to possible applications in creating customizable, atomic scale diodes.

4.2. EXPERIMENTAL METHOD

We use atom manipulation of single vacancies in the chlorine-terminated Cu(100) surface to engineer lateral confinement of field emission resonances. By coordinating chlorine vacancies— which are easily manipulable and thus suited to large scale atomic assembly [7, 14–16, 24]—adjacent to each other, we construct patches of exposed copper, surrounded by areas of homogeneous, monolayer chlorine coverage (Fig. 4.1a). The bare and chlorinated Cu(100) surfaces host FERs at bias voltages exceeding the local work function, at 4.6 V [25] and 5.7 V [26], respectively. These resonances can be readily modelled with a one-dimensional potential in the out-of-plane direction (Fig. 4.1, see 4.8.2 for details). The work function difference between the two surfaces results in a shift in the measured resonance energies (Fig. 4.1c), in accordance with previous studies [27–30].

Spectroscopy acquired at the center of the 7 × 7 patch (dimensions defined in unit cells of the chlorine lattice) exhibits additional resonances, in comparison to the bare and chlorinated Cu(100) surfaces (Fig. 4.1c). As shown in Fig. 4.1d, these additional resonances belong to a series of sub-resonances following each primary FER, and can in fact be resolved for each primary FER, up to and including the the fourth primary resonance. We use the principal quantum number n_z to describe the primary FERs. Note that the additional modes are only observed above the energy of the first resonance on bare Cu(100) (Fig. 4.1c). The full in-plane structure of the confined modes for the larger patches is best visualised by differential conductance maps taken at voltages corresponding to the sub-resonances of the first FER on the 7 × 7 patch, as shown in Fig. 4.1e. The observed states can be recognised as two-dimensional particle-in-a-box modes, with quantum numbers n_x and n_y, and can be accurately reproduced by the eigenstates of a finite potential well [31]. Similar to previous works [22], the nodal patterns of the first three modes are analogous to the orbitals of an two-dimensional atom, with the first state corresponding to the s-like state, and the second to the p-like, and subsequently the d-like state. Finally, we note that the energy of the FERs depends on the patch size: as the patch size is increased, the FER energy shifts down, tending toward the limit of bare Cu(100). All in all, the assembled patches can be seen as atomically precise potential wells, wherein the energy, spacing, and order of the states can be tuned by adjusting the shape and size of the confining potential. We note that the single vacancy [7, 14–16] stands out as an exception, as the necessary change in the local work function cannot take place on such small length-scales: as such, the vacancy acts as a scattering center, rather than a confinement potential.

4.3. LOWEST ENERGY FER LIFETIME

In order to characterize the electron lifetime, we consider the transport through these confined states: two electron baths, one on the tip side and another on the sample side, act as decoherent sources, the contributions of which we can disentangle by investigating the evolution of the differential conductance spectra as a function of conductance set-point, as shown in Fig. 4.2a. With increasing conductance setpoint, we observe a slight shift in the energy of the FERs, which is explained by the increased out-of-plane confinement (Fig. 4.1b), as well as the appearance of negative differential resistance (NDR). The appearance of NDR at high conductance setpoints gives us qualitative insight into the coupling of the resonances with the substrate and tip.

We consider a transport model describing the resonant tunneling of independent electrons from (to) the tip and sample through a level localized between the two potential barriers ([31] and 4.2a, inset). In this framework, the current through a single resonance is given by:

$$I_i = \frac{2 G_Q \hbar}{e} \frac{\Gamma_t^i(z, V) \Gamma_s^i(z, V)}{\Gamma_t^i(z, V) + \Gamma_s^i(z, V)} \left(\frac{\pi}{2} + \tan^{-1}\left(\frac{2(eV - E_i(z, V))}{\hbar(\Gamma_t^i(z, V) + \Gamma_s^i(z, V))} \right) \right), \tag{4.1}$$

where the quantum of conductance is $G_Q = e^2/(\pi\hbar)$, Γ_t^i and Γ_s^i are, respectively, the tip and sample decay rates for the ith resonance, and E_i its energy, whose shift with bias voltage we will initially neglect for simplicity. In general, the tip and sample decay rates
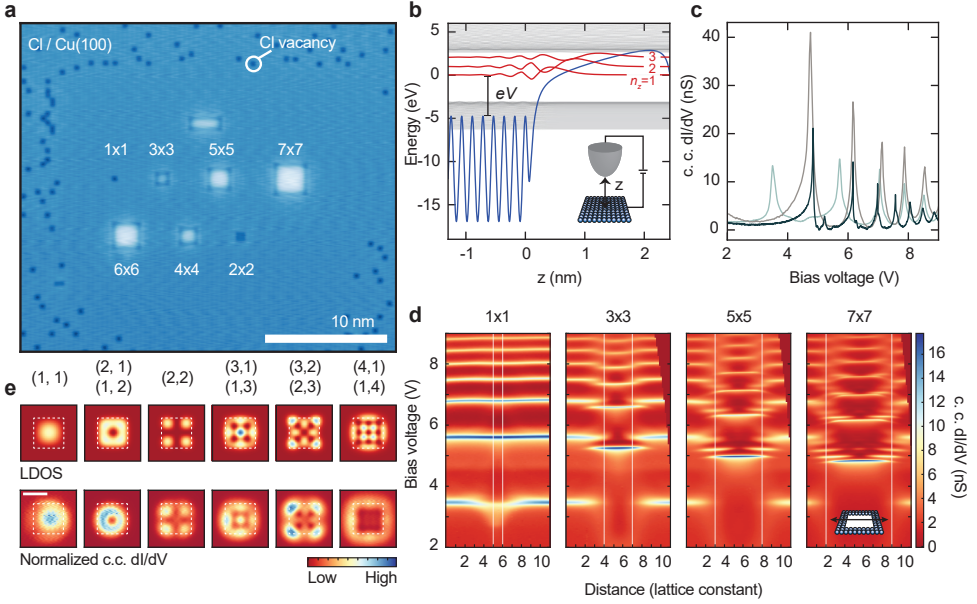
Figure 4.1: Confinement of field-emission resonances. (**a**) STM constant-current topography (600 mV, 300 pA) of square, atomically assembled patches of Cl vacancies, with sizes indicated in unit cells. (**b**) Potential landscape (blue) between sample (left) and tip (right) for a finite bias voltage V. Amongst the wave functions (grey) calculated for this potential, are the first three field-emission resonances (red). Inset: schematic of the tip-sample junction. (**c**) Constant-current differential conductance spectra acquired for bare Cu(100) (grey, 250 pA current setpoint), the chlorine monolayer (turquoise, 100 pA), and the center of the 7 × 7 patch (black, 100 pA). The first peak on the chlorine monolayer (3.5 V), being below the surface work function, corresponds to an image-potential state. (**d**) Stacked constant-current (100 pA) differential conductance spectra taken along a line crossing the center of each patch (shown in inset), with the corresponding patch size indicated (top). A correction is applied to the data to rectify the asymmetry of the tip electric field [31] White lines indicate the patch boundaries. (**e**) Calculated LDOS of the particle-in-a-box states ($|\Psi|^2$), obtained using a finite well model (top row). Normalized [32] constant-current (100 pA) differential conductance maps acquired for the 7 × 7 patch at the resonance energies of the first principal FER ($n_z = 1$, $(n_x, n_y) = (1, 1)$) and the following sub-resonances. White squares delineate the spatial extent of the simulated potential well (top row) and the physical patch (bottom row).

are both distance and voltage dependent. For the former, this dependence is derived by considering the transmission through the tunnel barrier. The sample decay rate, however, encapsulates an effective barrier that depends on the surface band-structure, and the relationship between Γ_s and V is non-trivial; we approximate this dependence as either constant or linear, depending on the width of the voltage window we consider. The differential conductance, in turn, can be obtained by differentiating the current with respect to voltage, and contains terms that scale with the derivatives of the decay rates and the energy of the resonance [31].

We can gain quantitative insight into the tip and sample decay rates by focusing strictly on the first principal FER (Fig. 4.2b inset): this allows us to drastically reduce the number of free variables to a single resonance, and consequently to meaningfully account for the

effects of the changing level E_0; additionally, we simplify $\Gamma_s(V)$ to a constant in the narrow voltage range around the resonance. By fitting the measured differential conductance at each conductance setpoint to our model, we can extract a value for the tip and sample decay rates as function of conductance setpoint (Fig. 4.2b and c).

In Fig. 4.2b, we see that Γ_s increases with conductance setpoint, which can be related to the FER wave function: in general, decay to the bulk is governed by the overlap of the vacuum-localized state to the substrate, which is in turn determined via the penetration of the state into the bulk, the evanescent tail of the bulk states into the vacuum, and the diminished electronic screening in the area between the surface and the vacuum [33, 34]. Bringing the tip closer causes a redistribution of the weight of the wave function toward the surface, rendering the scattering channels to the bulk more efficient [35], leading to an increase in Γ_s. More precisely, we consider that the sample decay rate should scale linearly with the wave function overlap of the FER with the sample [33], and for simplicity we assume its increase to be inversely proportional to the tip-sample distance. Given the exponential dependence of current with distance, we thus expect an inverse logarithmic dependence of the sample decay rate on the conductance setpoint. The fit in Fig. 4.2b shows this simple relation describes the change in Γ_s appropriately.

The evolution of the tip decay rate with conductance setpoint is straightforward: this rate should scale exponentially with the tip-sample distance, meaning it should be linear with the conductance setpoint and intercept with the origin, as we see in Fig. 4.2c. Importantly, the changes in the decay rates impact the overall occupation of the state. The occupation is determined by the ratio of the tip decay rate to total decay rate $\Gamma_s + \Gamma_t$, meaning that the occupation of the state can be tuned via the tip-height, as shown in Fig. 4.2c: the occupation linearly increases with the conductance setpoint. In effect, this means that the competing factors determining the time-average occupation—the rate of tunneling electrons versus the increase in the lifetime-limiting rate, Γ_s—results in the state filling increasing as the tip is brought closer.

4.4. HIGHER ENERGY FER LIFETIMES

We now extend our scope to account for transport through the higher energy states—around 5.6 V ($n_z = 1$, $(n_x, n_y) = (2, 1), (1, 2)$) and 6 V ($(3, 1), (1, 3)$), respectively. To do so, we assume the resonances are independent, i.e. that the total current is determined by the sum of the currents I_i through each resonance; additionally, we explicitly account for the voltage-dependence of $\Gamma_s(V)$ as linear to first approximation. As seen in Fig. 4.2b (inset), our model successfully reproduces the key features of the measured differential conductance over the entire voltage range, with, in particular, the presence of NDR between ∼ 5.6 to 6 V. In this window, we find $d\Gamma_s/dV < 0$. In fact, we find it is necessary to have a decreasing sample decay rate with increasing voltage to engender NDR, indicating once again that the decay path to the sample crucially depends on the electronic wave function of the FER.

While the decay rates can be tuned by changing the out-of-plane confinement of the wave function, the in-plane confinement plays the dominant role in setting an upper bound on the lifetime. Typically, field-emission resonances are delocalized (Bloch-like) in the directions parallel to the surface and thus form bands [36]. In that case, the electron lifetime is affected by interband scattering, wherein the excited electron escapes
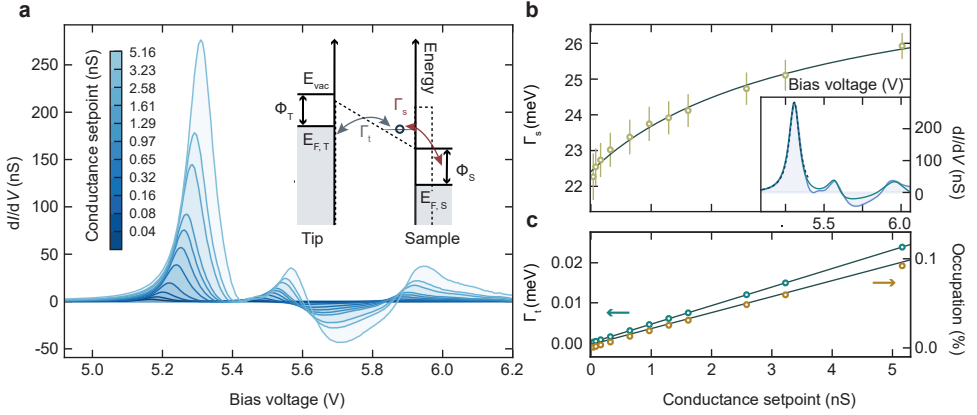
Figure 4.2: Extracting tip and sample decay rates. (**a**) Constant-height differential conductance spectra obtained at the center of the 5 × 5 patch for a range of conductance setpoints ((250 pA → 32 nA), 6.2 V). Inset: schematic of the double-barrier potential (dotted line) implemented in the rate equations, with the decay rates to the tip and sample, Γ_t and Γ_s, indicated. (**b**) Inset: constant-height differential conductance (light blue, shaded) acquired at the center of the 5 × 5 patch (32 nA, 6.2 V). Calculated dIdV using a resonant tunneling model for a single level (navy, dotted line) or several, independent levels (green solid line). (**b**), (**c**) Sample (b, yellow circles) and tip (c, green circles) decay rates extracted for the first principal resonance as a function of conductance setpoint, fitted (solid grey line) to an inverse natural logarithm and a line, respectively. The tip decay rate is evaluated at the energy of the peak of the first principal field emission resonance. (**c**) Average occupation versus conductance setpoint (orange circles), and the corresponding linear fit (solid grey line).

into the metal (sample or tip), or scatters with an electron in a different band; and intraband scattering, in which case the electron changes velocity [33, 37]. We can expect the introduction of lateral localization to affect decay through these channels in two opposing ways: the increased confinement causes the bands to split into quantized states, strongly attenuating intraband decay, while the simultaneous broadening of the k-space distribution increases the available interband decay paths to the bulk. We assess the degree to which the in-plane confinement precisely affects the lifetime by investigating the transport characteristics of different sized patches.

Performing the same conductance-dependent measurements, we see a marked change in the relative strength of the NDR based on the dimensions of the confining patch, as shown in Fig. 4.3a. The relative NDR strength, which we define as the ratio of negative area to the total area under the differential conductance spectrum, stays fairly constant as a function of conductance setpoint for patches of larger size, such as the 7 × 7 and 5 × 5. In contrast, the smallest patch (2 × 2) does not exhibit any NDR at low conductance setpoints; at a conductance setpoint of ~0.5 nS, the relative NDR strength becomes non-zero and monotonically increases thereafter. The same general trend holds for the 3 × 3: exponentially increasing NDR strength with increasing conductance setpoint. In fact, the NDR is directly related to the change in the sample decay rate as a function of voltage, and we can see this variance in Γ_s in the strength and conductance-dependent behaviour of the NDR for the different patches.

As before, to quantify the change in the sample decay rate, we extract Γ_s by fitting equation (4.1) to the first principal FER of each patch, for a discrete range of conductance
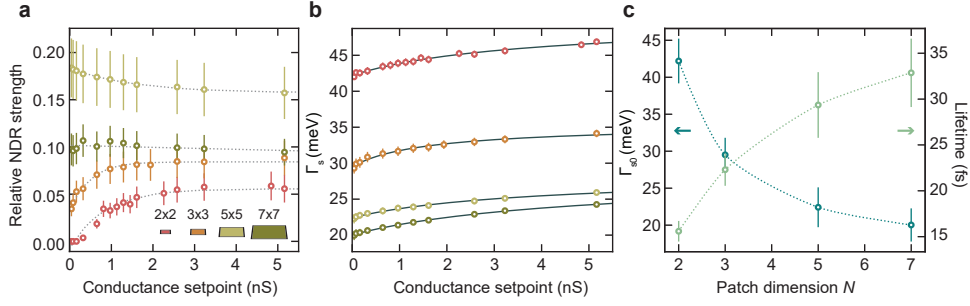
Figure 4.3: Tuning of the lifetime. (**a**) Relative strength of the negative differential resistance as a function of conductance setpoint, for patches of various size. Colors correspond to illustration in the inset. Dotted lines are guides to the eye. (**b**) Conductance-dependence of the sample decay rate for corresponding patch sizes, fitted to an inverse natural logarithmic function (grey solid lines). (**c**) Extrapolated value of the sample decay rate for zero setpoint conductance (blue circles), and the corresponding lifetime (green circles) for each patch size. Dotted lines are guides to eye.

setpoints (Fig. 4.3b). We see that both the magnitude of the sample decay rate, and its rate of change over this conductance setpoint range, vary according to patch size. The electrons localized above the smallest patch experience the largest sample decay rates, meaning scattering to the bulk becomes more efficient due to the increased spatial confinement.

The lifetime of these localized electrons, τ, is determined by the tip and sample decay rates, such that $\tau^{-1} = \Gamma_s^{-1} + \Gamma_t^{-1}$. The tip contribution exponentially tends to zero as a function of the tip-sample distance, meaning the intrinsic lifetime (at zero conductance setpoint, namely when the tip is infinitely far away) is determined by the sample decay rate at zero conductance. Approximating the lifetime by the linewidth of the resonance is not valid here, as the potential in the out-of-plane direction changes as we perform spectroscopy, leading to a changing resonance energy as a function of the applied voltage that artificially broadens the peak.

As shown in Fig. 4.3c, the extracted lifetimes monotonically increase as a function of patch size up to $N = 7$, the maximum patch dimension studied in this work. Notably, the lifetime for the confined states is roughly 2-4 times longer than the lifetime of the first resonance on bare Cu(100), extracted using the same method and in fair agreement with previously reported values [31]. This also indicates that there must be a patch size with an optimally long lifetime, after which τ begins decreasing with patch size, tending toward the freely-propagating Cu(100) limit. Indeed, the degree to which the confinement prohibits the different decay paths at play is ultimately a delicate balance: the smaller the patch, the fewer states available for scattering between different resonances, but the larger the k-space overlap with the bulk states. Notably, the lifetime-limiting rate for all the patches shown here is Γ_s, which in our case is approximately three orders of magnitude larger than the tip decay rate Γ_t (Fig. 4.2c).

4.5. MODEL OF THE NEGATIVE DIFFERENTIAL RESISTANCE

To better determine the role of the in- and out-of-plane confinement on the lifetime, we investigate the spectral weight of the localized resonances in k-space and compare this to the bulk band structure of copper. We calculate the wave function Ψ, which we assume to be separable, in the directions parallel and perpendicular to the (100) direction to obtain the corresponding k-space distribution. First, we consider the out-of-plane direction, where the confinement is set by the tip-sample distance and the applied voltage. We restrict our focus to the calculated wave-function, $\Psi(z)$, for the first principal FER and the resulting Fourier transform, $\Psi(k_\perp)$, shown in Fig. 4.4a. The $k_\perp$ values with a significant spectral weight span the entirety of the first Brillouin zone (BZ) (± 1.75 Å).

Along the in-plane directions, we consider the wave functions $\Psi(x)$ and $\Psi(y)$ corresponding to the first ($(1,1)$) particle-in-a-box mode for the 3×3 and 7×7 patches (Fig. 4.4b and c). As expected, the $k_\parallel$-space distribution widens as the patch size decreases. Furthermore, as shown in Fig. 4.4c, this broadening also takes place when the quantum numbers (n_x, n_y) of the in-plane mode increase. This is due to changes in the apparent barrier height: compare, for instance, the first and second particle-in-a-box modes—since the latter lies at higher energy than the former, it experiences a shallower finite well. Such considerations allow us to visualize how the factors considered so far—such as the tip-sample distance, the lateral extent of the patch, the apparent height of the in-plane barrier—impact the distribution of the state in k-space, and consequently its overlap with the bulk states.

To better illustrate this, we consider the band structure of bulk copper along the high symmetry lines [38], specifically at the experimental energies of the particle-in-a-box modes (Fig. 4.4d). The lifetime of the confined electrons depends directly on, and is limited by, the number of bulk states available for direct tunneling—the more bands we cross at the energy of the resonance, with k-values falling within $\Psi(k)$, the shorter the lifetime to first order. In this energy range, we cross several bulk bands along the high symmetry lines (X → W, W → L, L → Γ, Γ → K); however, the efficiency of these decay paths is scaled by the spectral weight of $\Psi(k)$ at the crossing points. In other words, the efficiency of the decay paths is scaled by the probability of having an electron with the right momentum for direct tunneling into that bulk state.

Accordingly, in Fig. 4.4e and f, we consider the intensity of the k-space wave function along various cross-sections of the first BZ (Fig. 4.4d, inset). Interestingly, the highest spectral weight is along the Γ → X direction—across both the lateral (Fig. 4.4e) and vertical (Fig. 4.4f) cross-sections—relative to the other high symmetry lines; however, this direction does not present any band crossing along the high symmetry lines at the energy of the resonances. In fact, $\Psi(k)$ carries little, if any, spectral weight along the other directions where it does cross the bulk bands. This is illustrated in Fig.s 4.4e and f, where we see that $\Psi(k)$ has practically zero intensity along the energy isosurfaces (at 5 V and 6 V) of bulk Cu, calculated using density functional theory (DFT) (see 4.8.4 for details). This is quite remarkable: although the lateral confinement of the states introduces direct tunneling paths to the bulk that are not present for the laterally freely-propagating case, we can consider the contribution to be minimal in this case. Additionally, the added confinement acts to largely hinder the role of intraband inelastic scattering, as the available states for scattering are substantially reduced: the FERs no longer form bands, but are rather quan-

tized and well-separated in energy, according to the physical dimensions of the patch. These two effects ultimately amount to a considerable enhancement of the lifetime of the confined states.

These considerations also shed light on the dependence of the sample decay rate Γ_s with bias voltage—which, as we previously found, is critical in engendering NDR. Namely: with increasing voltage, the localized resonance is pushed to higher energies, causing a shift in the crossing points with the bulk bands. In turn, this shift translates into the decay channels being scaled by a slightly different spectral weight. To illustrate this effect, we can consider the crossing along the $\Gamma \to K$ direction: as the bias increases, the FER shifts up in energy, meaning that the crossing point for the lower band moves away from the Γ point, closer to the K point. Fig. 4.4e and f show that this shift is accompanied by a decrease in the spectral weight of $\Psi(k)$, meaning the total overlap between the localized state and the bulk bands decreases. The emergence of the upper band around ~4.5V, however, further complicates the picture, illustrating that the overall rate of change of the decay rate is hard to estimate. However, by qualitatively considering the evolution of the k-space overlap, we can already grasp the complexity of the dependence of Γ_s on the bias voltage.

To get a quantitative estimate of the change in the sample decay rate, we calculate the weighted k-space wave function overlap for each DFT-calculated crossing point throughout the entire BZ, and relate that to a dimensionless sample-decay rate via Fermi's golden rule (Fig. 4.4g, see section 4.8.3 for details). For this, we consider the calculated k-space wave function of the 5×5 patch for the first $(1,1)$, second $(2,1)$, $(1,2)$, and fourth $(3,1)$, $(1,3)$ particle-in-a-box modes—the only states with non-zero intensity at the center of the patch (see Fig. 4.1d and 4.2a). As shown in Fig. 4.4g, we see that the calculated sample decay rate for all three states monotonically decreases, i.e. that the overlap of $\Psi(k)$ with the bulk bands decreases with increasing voltage, so that $d\Gamma_s/dV$ is negative—the ratio of this rate of change to the intercept is in good agreement with our quantitative results from the double barrier model (Fig. 4.2). The sample decay rate associated with each state is strictly only applicable in the voltage range in which that state is measured, roughly delineated in Fig. 4.4g by the shaded areas. All in all, we can confidently attribute the NDR to the effects of the bulk band structure. Additionally, we should also note that the NDR is consistently observed with different tips, and is not observed for laterally propagating FERs [31, 39, 40], which do not have direct tunneling paths to the bulk available to them.

4.6. CONCLUSION

By laterally confining field-emission resonances through atomic assembly of single chlorine vacancies, we present a new platform for creating artificial atoms. We demonstrate control over the lifetime and occupation of these artificial atoms by adjusting the confining potential, implemented via modification of the tip-sample distance or the lateral dimensions of the patch. The ability to tune the occupation is a key parameter of control in the study of quantum many-body states that evolve as a function of the state filling. We show that the lifetime of field-emission resonances, unlike that of surface states, can be prolonged via lateral confinement, up to nearly four times the freely-propagating case. This extension of the lifetime enhances the available energy resolution, and, in conjunc-
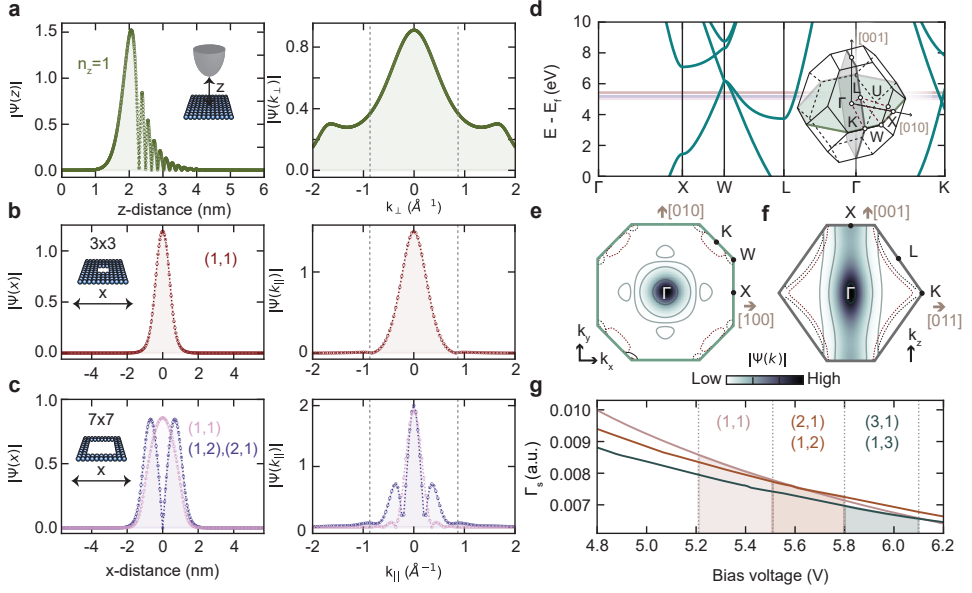
Figure 4.4: Distribution in *k*-space. (**a**) Calculated out-of-plane component of the real space wave function $|\psi(z)|$ for the first principal FER $n_z = 0$ (left), and the corresponding Fourier transform (right), at tip-sample distance $z = 2.4$ nm. (**b**), (**c**) Calculated in-plane component of the real space wave function (left) for the (**b**) 3×3 (**c**) and 7×7 patches, showing the first $(n_x, n_y) = (1, 1)$ ((**b**), red; (**c**), pink) and second $(1, 2), (2, 1)$ ((**c**), purple) modes, with the corresponding Fourier transforms (right). Dotted lines indicate $\pm \pi / a$ bounds. (**d**) Bulk band structure of Cu along high symmetry lines, with the experimental resonance energy of the $(1, 1)$ state for the 3×3 (red) and 7×7 (pink), as well as the $(1, 2)/(2, 1)$ state of the latter (purple), denoted by solid lines. Inset: schematic of the first Brillouin zone of Cu. (**e**, **f**) Intensity of the 3×3 wave function in *k*-space across Brillouin zone slices indicated in inset of (**d**). Solid contour lines delineate an order of magnitude change in the intensity. Corresponding DFT-calculated constant-energy isolines shown for bulk Cu bands, taken 5 V (black line) and 6 V (red line) above the Fermi level. (**g**) Calculated sample decay rate as a function of bias voltage, shown for the first three resonances probed in the center of a 5×5 patch, corresponding to the $(1, 1)$ (mauve line), $(2, 1)/(1, 2)$ (brown line), and $(3, 1)/(1, 3)$ (grey line) modes. The shaded areas correspond to the voltage range in which the respective modes are typically measured, delineating Γ_s in that range.

tion with control over the state filling, is a first step towards studying electron-electron interactions with artificial lattices. Further prolonging the lifetime to approach a state occupation of 1 for reasonable setpoint currents can be pursued via several avenues: such as finding an underlying bulk crystal that hosts FER bands closer to the Fermi energy, or one that is semi-conducting or even insulating. These considerations make confined vacuum resonances a promising platform for creating and studying artificial lattices.

4.7. EXPERIMENTAL METHODS

Sample preparation and experimentation were performed in ultrahigh vacuum systems with a base pressure of 10^{-10} mbar (Unisoku USM1300s, SPECS Joule-Thompson-SPM). The Cu(100) crystal was cleaned via repeated cycles of argon sputter at 1 kV and annealing to 600° C. The chlorinated copper surface was prepared by thermal evaporation

(2-3 minutes) of anhydrous $CuCl_2$ powder heated to $300°$ C onto a warm Cu(100) crystal. The crystal was heated to $150°$ C for ~ 10 minutes before and after deposition [24]. The coverage and sample quality were verified via LEED (where possible) and STM. Atom manipulation of chlorine vacancies was implemented using a procedure previously outlined [24]. Differential conductance measurements were performed using standard lock-in detection techniques.

## 4.8. SURFACE TRANSPORT SIMULATION DETAILS

4.8.1. MODELLING THE IN-PLANE CONFINEMENT

The engineered lateral confinement of the field emission resonances, which physically arises from the work function difference between the bare and chlorinated Cu(100) surfaces, can be simply modelled using a finite, slanted square potential well. The depth of the potential well is set by the work function difference $\Delta\phi = 1.1 \pm 0.1$ eV between the two surfaces [26]. It is also possible to estimate $\Delta\phi$ from the energy shift of the first field-emission resonance on each surface [29, 30]; this method also yields a difference of roughly 1 V (see Fig. 4.1c). Since the work function change cannot occur with an infinitely sharp slope, we assume the potential well is slanted: we consider that the slope is set by $\Delta\phi$, as well as by the Fermi wavelength of the tunneling electrons, which is roughly 1.5 units cells at 5V.

We calculate the expected energy of the observed resonances by numerically solving the Schrödinger equation [41] for this potential; this gives us the energy spacing between the main and sub resonances. The total potential landscape, which also has an out-of-plane component, described by the trapezoidal potential barrier at the tip-sample junction, is separable, meaning the eigenenergies for each direction can be simply added. For ease of comparison between the energies calculated for the in-plane confinement and those measured, we subtract the out-of-plane component by defining the energy axis relative to the energy of the first field-emission resonance. As shown in Fig. 4.5, the comparison between the energies extracted from the measured constant-height dI/dV to those obtained numerically is fair. Note that the third in-plane confinement mode is absent in the measured dI/dV spectrum obtained at the center of the patch, as this point corresponds to the intersection of the two nodal planes for the $(n_x, n_y) = (2, 2)$ state. As such, we also compare the results of the calculations to the energies of the constant-current dI/dV maps shown in Fig. 4.1e, we have good agreement.

4.8.2. MODELLING THE OUT-OF-PLANE CONFINEMENT

The field emission resonances are modelled with a one-dimensional potential [42, 43]. The sample potential ($z \leq 0$) is taken to be periodic in the bulk, with a periodicity set by $a/2$, the distance between two atomic layers in the out-of-plane direction, where a is the lattice constant. The potential beyond the surface atomic layer is modelled with a potential well ($0 \leq z \leq z_1$) and subsequently, an exponential decay of the potential towards the tip vacuum level. ($z_1 \leq z \leq z_{im}$). To account for the tip (at z_{tip}) [42], we add the linear potential, $V_{lin}(z)$, between the tip and sample ($z_1 \leq z \leq z_{tip}$), caused by the applied voltage, and account for the contact potential by including the tip (ϕ_t) and sample work functions (ϕ_s). The long-range image potential, $V_{im}(z)$, which accommodates multiple images in
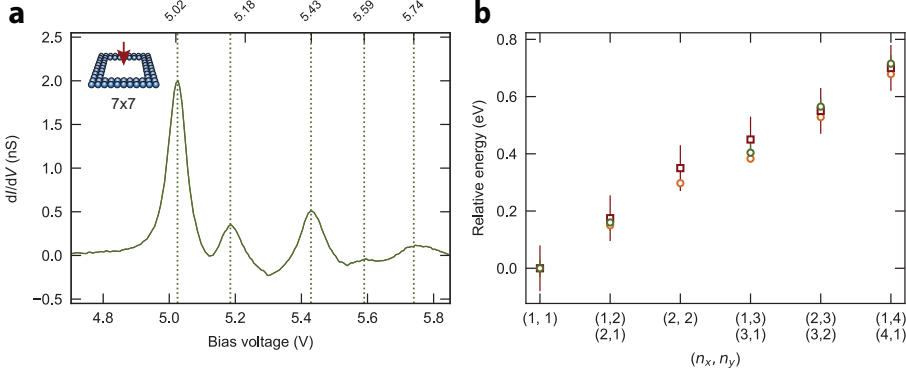
Figure 4.5: Comparison of calculated and measured eigenenergies of the particle-in-a-box states of the laterally confined field-emission resonances. (**a**) Constant-height differential conductance spectrum (conductance set-point at 250 pA/6.2 V) acquired at the center of the 7 × 7 patch, as indicated in the inset. Dotted lines indicate the energy of the first main resonance (5.02V) and the following sub-resonances. (**b**) Resonance energies extracted from point spectroscopy performed at the center of the 7 × 7 patch (green circles); we compare this to the energies of the constant-current (100 pA) differential conductance maps (red squares) shown in Fig. 1e of the main text, as well as the energy calculated for each state using a finite potential well model (orange circles). In each case, we define the energy axis relative to the energy of the first field-emission resonance.

both tip and sample, is also included, giving rise to the following total potential (Fig. 4.6) across the tip-sample junction:

$$
V(z) = \begin{cases}
A_{10} + A_1 \cos\left(\frac{2\pi}{\bar{a}}\right) & z \leq 0 \\
A_{20} + A_2 \cos(\beta z) & 0 \leq z \leq z_1 \\
V_{\text{lin}}(z) + A_3 \exp(-\alpha(z - z_1)) & z_1 \leq z \leq z_{\text{im}} \\
V_{\text{lin}}(z) - V_{\text{im}}(z) & z_{\text{im}} \leq z \leq z_{\text{tip}},
\end{cases}
\tag{4.2}
$$

where

$$
V_{\text{lin}}(z) = E_{f,s} + s(eV + \phi_t) + (1 - s)\phi_s,
\tag{4.3}
$$

given $E_{f,s}$ is the sample Fermi energy, and $s = (z - z_1)/(z_{\text{tip}} - z_1)$. We chose to define the potential relative to the tip Fermi level, meaning $E_{f,s} = -eV_{\text{bias}}$. Additionally, we can define the image potential as:

$$
V_{\text{im}}(z) = \left(1 - \exp(-\lambda(z - z_{\text{im}}))\right) \frac{e^2 \left(2\Psi(1) - \Psi(\eta) - \Psi(1 - \eta)\right)}{16\pi\epsilon_0 \left(z_{\text{im}}^{\text{tip}} - z_{\text{im}}\right)},
\tag{4.4}
$$

where $\eta = (z - z_{\text{im}})/(z_{\text{im}}^{\text{tip}} - z_{\text{im}})$, e the electron charge, ϵ_0 the vacuum permittivity, and Ψ is the digamma function.

For a terminated metal surface, the parameters A_1 and A_{10} determine the width and position of the surface-projected band gap, respectively, whereas the parameters A_2 and β reproduce the experimental values of the binding energies of the image stakes in the absence of the tip. We set $A_{10} = -eV_{\text{bias}} - A_1$, as we chose the tip vacuum level as our reference, and assign A_1, A_{20}, A_2, β, and $z_1 = 5\pi/(4\beta)$ to their corresponding values
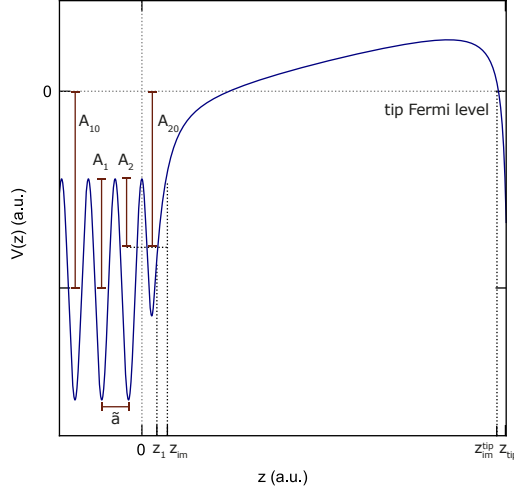
Figure 4.6: Potential used to calculate the energies and the wavefunctions of the field-emission resonances.
$(A_1, A_{10}, \bar{a})$ are the model parameters to reproduce the bulk band gap and $(A_2$ and $z_{tip})$ the model parameters to reproduce the experimental binding energies.

previously determined for a terminated Cu(100) surface, in the absence of the tip [43]. By forcing the potential and its derivative to be continuous everywhere (except at the tip position, z_{tip}), we can analytically determine the values for the remaining parameters (A_3, α, λ, z_{im}) in terms of already known parameters.

$$A_{20} = A_{10} + A_1 - A_2$$
$$A_3 = A_{20} + A_2 \cos(\beta z_1) - V_{lin}(z_1)$$
$$\alpha = \frac{eV_{bias} + \phi_t - \phi_s}{A_3(z_{tip} - z_1)} + \frac{\beta A_2}{A_3} \sin(\beta z_1)$$
$$\lambda = 2\alpha$$
$$z_{im} = \frac{-1}{\alpha} \ln\left(\frac{-\lambda e^2}{16\pi\epsilon_0 A_3}\right) + z_1$$

We note that the tip image plane is not well defined in the above potential (and hard to estimate from experiment); we assign $z_{im}^{tip} \approx z_{tip} - 0.3$ Å. Solving the time-independent Schrödinger equation [41] using this potential (equation 4.2) results in the calculated wave-functions shown in the Figs. 4.1 and 4.4.

4.8.3. ESTIMATING THE SAMPLE DECAY RATE
To first order, the sample decay rate for each field emission resonance follows Fermi's golden rule:

$$\Gamma_s = \frac{2\pi}{\hbar} |\langle f | H' | i \rangle|^2 \rho_{E_f}. \tag{4.5}$$

The initial state $|i\rangle = \sum_{\mathbf{k}} \psi(\mathbf{k}) |\mathbf{k}\rangle \otimes |0\rangle$ denotes a filled FER with k-space distribution $\psi(\mathbf{k})$, and Cu in the ground-state; and the final state $|f\rangle = |0\rangle \otimes |\mathbf{k}'\rangle$ indicating an unfilled FER and the Cu in first excited state, at the energy of the FER. Note that we have introduced the notation $|\mathbf{k}\rangle = \hat{c}_{\mathbf{k}}^{\dagger} |0\rangle$, with $\hat{c}_{\mathbf{k}}^{\dagger}$ the fermionic creation operator for quasi momentum $\mathbf{k} = (k_x, k_y, k_z)$.

Since the decay is dominated by elastic scattering, the Hamiltonian connecting the initial and final states can be written as $H' = \sum_{\mathbf{k}} J \hat{c}_{\mathbf{k}'}^{\dagger} \hat{c}_{\mathbf{k}}$. Here, J is the coupling between the FER and sample; we assume J does not vary with $\mathbf{k}$. Finally, the density of states of the bulk sample is denoted by $\rho_{E_f} = \frac{1}{\mathcal{V}} \sum_m \delta(E_f - \epsilon_{m\mathbf{k}})$, with $\mathcal{V}$ the volume, m the Cu band index and $\epsilon_{m\mathbf{k}}$ the corresponding dispersion. When we substitute this in the above expression for the sample decay rate, we find:

$$\Gamma_s(V) = \frac{2\pi}{\hbar} \sum_{\mathbf{k}'} |\langle \mathbf{k}'| \langle 0| J \sum_{\mathbf{k}\mathbf{k}'} c_{\mathbf{k}'}^{\dagger} c_{\mathbf{k}} |0\rangle \sum_{\mathbf{k}} \psi(\mathbf{k}) |\mathbf{k}\rangle |^2 \frac{1}{\mathcal{V}} \sum_m \delta(E_i(V) - \epsilon_{m\mathbf{k}}) \tag{4.6}$$

$$= \frac{2\pi}{\hbar} J^2 \sum_{\mathbf{k}} |\psi(\mathbf{k})|^2 \frac{1}{\mathcal{V}} \sum_m \delta(E_i(V) - \epsilon_{m\mathbf{k}}) \tag{4.7}$$

$$\propto \int_{BZ} d\mathbf{k} |\psi(\mathbf{k})|^2 \sum_m \delta(E_i(V) - \epsilon_{m\mathbf{k}}), \tag{4.8}$$

where the proportionality comes from the constant $\frac{J^2}{2\pi\hbar}$. This expression can be simply understood as the overlap in k-space between the Cu band structure and the bound state, at the resonance energy of the latter. This energy depends on bias according to [31]:

$$E_i(V) = \beta_i (eV)^{2/3}. \tag{4.9}$$

Here, we approximate the tip and sample work functions to be the same. We can determine β_i by assuming that the center of the resonance (measured via differential conductance spectroscopy) is equal to E_i at that bias V (see Fig. 4.2). Additionally, we assume the FER k-space distribution $\psi(\mathbf{k})$ remains approximately constant while the applied bias or tip-sample distance is changing. We can then evaluate the integral numerically using the Blöchl tetrahedron method for Brillouin zone (BZ) integration [44], as implemented in dfttools [45], with the Cu dispersion coming from DFT, and the FER wave function as calculated in sections 4.8.1 and 4.8.2. We note that prior to integration, we fold the part of the wave functions with finite weight outside the first BZ back onto the first BZ.

4.8.4. DENSITY FUNCTIONAL THEORY (DFT) CALCULATIONS

To calculate the bulk band structure of Cu, we use plane-wave density-functional theory with a standard ultrasoft scalar relativistic pseudopotential and PBE exchange correlation functional, as implemented in the Quantum ESPRESSO package [46]. Plane wave energy cutoffs were set to 120/1080 Ry (wave function/density). We initialised the atoms on a FCC lattice with lattice constant 3.61 Å. Self-consistent calculation was done on a 4x4x4 k-point grid and followed by non self-consistent Gamma-point Brillouin zone sampling on a 32x32x32 k-point grid. The visualization of constant-energy surface cuts was done with FermiSurfer [47].

4.9. DATA AVAILABILITY

4.10. ACKNOWLEDGEMENTS

4.11. AUTHOR CONTRIBUTIONS

RR conceived the paper. RR, LF, and JG conducted the experiments. RR, LF and YB did the analytic derivations and RB the DFT calculations. All authors contributed to the discussion and the writing of the manuscript.

4

REFERENCES

[1] Rejali, R. *et al.* Confined vacuum resonances as artificial atoms with tunable lifetime. *ACS nano* **16**, 11251–11258 (2022).

[2] Bloch, I., Dalibard, J. & Nascimbène, S. Quantum simulations with ultracold quantum gases. *Nature Physics* **8**, 267–276 (2012).

[3] Bloch, I. Ultracold quantum gases in optical lattices. *Nature Physics* **1**, 23–30 (2005).

[4] Gross, C. & Bloch, I. Quantum simulations with ultracold atoms in optical lattices. *Science* **357**, 995–1001 (2017).

[5] Blatt, R. & Roos, C. F. Quantum simulations with trapped ions. *Nature Physics* **8**, 277–284 (2012).

[6] Khajetoorians, A. A., Wegner, D., Otte, A. F. & Swart, I. Creating designer quantum states of matter atom-by-atom. *Nature Reviews Physics* **1**, 703–715 (2019).

[7] Drost, R., Ojanen, T., Harju, A. & Liljeroth, P. Topological states in engineered atomic lattices. *Nature Physics* **13**, 668–671 (2017).

[8] Slot, M. R. *et al.* Experimental realization and characterization of an electronic Lieb lattice. *Nature Physics* **13**, 672–676 (2017).

[9] Gomes, K. K., Mar, W., Ko, W., Guinea, F. & Manoharan, H. C. Designer Dirac fermions and topological phases in molecular graphene. *Nature* **483**, 306–310 (2012).

[10] Gardenier, T. S. *et al.* p orbital flat band and Dirac cone in the electronic honeycomb lattice. *ACS Nano* **14**, 13638–13644 (2020).

[11] Kempkes, S. N. *et al.* Robust zero-energy modes in an electronic higher-order topological insulator. *Nature Materials* **18**, 1292–1297 (2019).

[12] Freeney, S. E., van den Broeke, J. J., Harsveld van der Veen, A. J. J., Swart, I. & Morais Smith, C. Edge-dependent topology in kekulé lattices. *Phys. Rev. Lett.* **124**, 236404 (2020).

[13] Kempkes, S. N. *et al.* Design and characterization of electrons in a fractal geometry. *Nature Physics* **15**, 127–131 (2019).

[14] Huda, M. N., Kezilebieke, S., Ojanen, T., Drost, R. & Liljeroth, P. Tuneable topological domain wall states in engineered atomic chains. *npj Quantum Materials* **5**, 17 (2020).

[15] Huda, M. N., Kezilebieke, S. & Liljeroth, P. Designer flat bands in quasi-one-dimensional atomic lattices. *Phys. Rev. Research* **2**, 043426 (2020).

[16] Girovsky, J. *et al.* Emergence of quasiparticle Bloch states in artificial crystals crafted atom-by-atom. *SciPost Physics* **2**, 020 (2017).

[17] Collins, L. C., Witte, T. G., Silverman, R., Green, D. B. & Gomes, K. K. Imaging quasiperiodic electronic states in a synthetic penrose tiling. *Nature Communications* **8**, 15961 (2017).

[18] Braun, K.-F. & Rieder, K.-H. Engineering electronic lifetimes in artificial atomic structures. *Phys. Rev. Lett.* **88**, 096801 (2002).

[19] Jensen, H., Kröger, J., Berndt, R. & Crampin, S. Electron dynamics in vacancy islands: Scanning tunneling spectroscopy on Ag(111). *Phys. Rev. B* **71**, 155417 (2005).

[20] Kliewer, J., Berndt, R. & Crampin, S. Scanning tunnelling spectroscopy of electron resonators. *New Journal of Physics* **3**, 22–22 (2001).

[21] Slot, M. R. *et al.* *p*-band engineering in artificial electronic lattices. *Phys. Rev. X* **9**, 011009 (2019).

[22] Freeney, S., Borman, S., Harteveld, J. & Swart, I. Coupling quantum corrals to form artificial molecules. *SciPost Phys.* **9**, 85 (2020).

[23] Sun, J. P., Haddad, G., Mazumder, P. & Schulman, J. Resonant tunneling diodes: models and properties. *Proceedings of the IEEE* **86**, 641–660 (1998).

[24] Kalff, F. E. *et al.* A kilobyte rewritable atomic memory. *Nature Nanotechnology* **11**, 926–929 (2016).

[25] Gartland, P. O., Berge, S. & Slagsvold, B. J. Photoelectric work function of a copper single crystal for the (100), (110), (111), and (112) faces. *Phys. Rev. Lett.* **28**, 738–739 (1972).

[26] Westphal, D. & Goldmann, A. Chlorine adsorption on copper: II. photoemission from Cu(001)c(2 × 2)-Cl and Cu(111)($\sqrt{3} \times \sqrt{3}$)R30°-Cl. *Surface Science* **131**, 113–138 (1983).

[27] Ruffieux, P. *et al.* Mapping the electronic surface potential of nanostructured surfaces. *Phys. Rev. Lett.* **102**, 086807 (2009).

[28] Jung, T., Mo, Y. W. & Himpsel, F. J. Identification of metals in scanning tunneling microscopy via image states. *Phys. Rev. Lett.* **74**, 1641–1644 (1995).

[29] Pivetta, M., Patthey, F. m. c., Stengel, M., Baldereschi, A. & Schneider, W.-D. Local work function Moiré pattern on ultrathin ionic films: NaCl on Ag(100). *Phys. Rev. B* **72**, 115404 (2005).

[30] Ploigt, H.-C., Brun, C., Pivetta, M., Patthey, F. m. c. & Schneider, W.-D. Local work function changes determined by field emission resonances: NaCl/Ag(100). *Phys. Rev. B* **76**, 195404 (2007).

[31] Rejali, R. *et al.* Supplementary: Confined vacuum resonances as artificial atoms with tunable lifetime. *ACS nano* **16**, 11251–11258 (2022).

[32] Rejali, R., Farinacci, L. & Otte, S. Normalization procedure for obtaining the local density of states from high-bias scanning tunneling spectroscopy. *arXiv preprint* (2022).

[33] Berthold, W. *et al.* Momentum-resolved lifetimes of image-potential states on Cu(100). *Phys. Rev. Lett.* **88**, 056805 (2002).

[34] Echenique, P., Pitarke, J., Chulkov, E. & Rubio, A. Theory of inelastic lifetimes of low-energy electrons in metals. *Chemical Physics* **251**, 1–35 (2000).

[35] Crampin, S. Lifetimes of stark-shifted image states. *Phys. Rev. Lett.* **95**, 046801 (2005).

[36] Wahl, P., Schneider, M. A., Diekhöner, L., Vogelgesang, R. & Kern, K. Quantum coherence of image-potential states. *Phys. Rev. Lett.* **91**, 106802 (2003).

[37] Echenique, P. *et al.* Decay of electronic excitations at metal surfaces. *Surface Science Reports* **52**, 219–317 (2004).

[38] Burdick, G. A. Energy band structure of copper. *Phys. Rev.* **129**, 138–150 (1963).

[39] Pascual, J. I. *et al.* Role of the electric field in surface electron dynamics above the vacuum level. *Phys. Rev. B* **75**, 165326 (2007).

[40] Stepanow, S. *et al.* Localization, splitting, and mixing of field emission resonances induced by alkali metal clusters on Cu(100). *Phys. Rev. B* **83**, 115101 (2011).

[41] Groth, C. W., Wimmer, M., Akhmerov, A. R. & Waintal, X. Kwant: a software package for quantum transport. *New Journal of Physics* **16**, 063065 (2014).

[42] Limot, L., Maroutian, T., Johansson, P. & Berndt, R. Surface-state stark shift in a scanning tunneling microscope. *Phys. Rev. Lett.* **91**, 196801 (2003).

[43] Chulkov, E., Silkin, V. & Echenique, P. Image potential states on metal surfaces: binding energies and wave functions. *Surface Science* **437**, 330–352 (1999).

[44] Blöchl, P. E., Jepsen, O. & Andersen, O. K. Improved tetrahedron method for brillouin-zone integrations. *Phys. Rev. B* **49**, 16223–16233 (1994).

4

[45] Pulkin, A. dfttools – parse, process and plot data from solid state and quantum chemistry applications. Zenodo, DOI: 10.5281/zenodo.6397700 (2022).

[46] Giannozzi, P. *et al.* Advanced capabilities for materials modelling with quantum espresso. *Journal of Physics: Condensed Matter* **29**, 465901 (2017).

[47] Kawamura, M. Fermisurfer: Fermi-surface viewer providing multiple representation schemes. *Computer Physics Communications* **239**, 197–203 (2019).

4

5

COHERENT SPIN DYNAMICS BETWEEN ELECTRON AND NUCLEUS WITHIN A SINGLE ATOM

Lukas M. Veldman, Evert W. Stolte, Mark P. Canavan, **Rik Broekhoven**, Phillip Willke,
Laetitia Farinacci and Sander Otte

The nuclear spin, being much more isolated from the environment than its electronic counterpart, presents opportunities for quantum experiments with prolonged coherence times. Electron spin resonance (ESR) combined with scanning tunneling microscopy (STM) provides a bottom-up platform to study the fundamental properties of nuclear spins of single atoms on a surface. However, access to the time evolution of nuclear spins remained a challenge.

Here, we present an experiment resolving the nanosecond coherent dynamics of a hyperfine-driven flip-flop interaction between the spin of an individual nucleus and that of an orbiting electron. We use the unique local controllability of the magnetic field emanating from the STM probe tip to bring the electron and nuclear spins in tune, as evidenced by a set of avoided level crossings in ESR-STM. Subsequently, we polarize both spins through scattering of tunneling electrons and measure the resulting free evolution of the coupled spin system using a DC pump-probe scheme. The latter reveals a complex pattern of multiple interfering coherent oscillations, providing unique insight into hyperfine physics on a single atom level.

5.1. Introduction

Nuclear spins have shown great promise as building blocks for quantum information in molecular spin qubits [1, 2], NV centers[3, 4], and donors in silicon[5]. They also are an excellent resource for quantum simulation[6], magnetic sensing[7, 8] and spintronics[9], and are potentially scalable via engineered molecular and atomic networks[10, 11] Their key advantage arises from their longer coherence times compared to their electron spin counterpart[12], though the intricacies of the decoherence channels depend on the exact interaction with the environment which is hard to control in ensemble averaging techniques. Scanning tunneling microscopy (STM) constitutes an excellent means of investigation here, as it permits to address individual electron spins in electron spin resonance (ESR) experiments with sub-nanometer resolution[13, 14], offering atomically precise information on their environment[15, 16], and providing a pathway towards coherent control of the spins states[17, 18]. In recent years, interactions involving the nuclear spin were measured indirectly by probing the hyperfine coupling in ESR-STM between the nucleus and the surrounding electrons[19]. In addition, the nuclear spin of individual Cu atoms could be polarized via spin pumping induced by the spin-polarized tunneling current[20]. However, accessing the coherent dynamics involving the nucleus remained challenging, due to its weak coupling to the tunneling electrons.

In this work, we show the free, coherent evolution between the nuclear spin and the electron spin in a single hydrogenated titanium atom. By fine-tuning the electronic Zeeman energy using the local field of the probe tip[21], we identify a parameter space where electronic and nuclear spin states hybridize. In a second step, we probe the free coherent evolution of the coupled system by electric DC pump-probe experiments[22]. Here, we reveal an emerging beating pattern, that originates from multiple quantum oscillations with different frequencies at the points of hybridization.

5.2. System of study

We use a commercial low-temperature STM equipped with high frequency cabling to send both RF signals and nanosecond DC pulses down to the tip. The sample system consists of Ti atoms deposited on bilayer MgO islands grown on Ag(100), that become hydrogenated by residual hydrogen[15, 16]. For all measurements, we use spin-polarized tips that are created by picking up co-deposited Fe atoms onto the tip apex. We study individual Ti adsorbed onto the oxygen sites of MgO – well-isolated from neighboring spins using atom manipulation (see Fig. 5.1a) – which exhibit an effective electron spin $\widehat{\mathbf{S}}$ with magnitude $S = \frac{1}{2}$ [15] and an anisotropic g-factor $\mathbf{g}$ [16]. Throughout this work, we focus on ^{47}Ti isotopes, which carry a nuclear spin $\widehat{\mathbf{I}}$ with magnitude $I = \frac{5}{2}$. Along the principal axes of the crystal field (x, y, z) with z out of plane, the system is described by the following Hamiltonian:

$$\widehat{\mathcal{H}} = \sum_{i=x,y,z} \left(\mu_B g_i \left(B_{ext,\, i} + B_{tip,\, i} \right) \widehat{S}_i + A_i \widehat{S}_i \widehat{I}_i + Q_i \widehat{I}_i^2 \right), \tag{5.1}$$

where μ_B is the Bohr magneton, and $\mathbf{A}$ and $\mathbf{Q}$ (see Sec. 5.7.1)[19] are the hyperfine coupling and quadrupole contributions, respectively. The first term describes the Zeeman energy of the electron spin with contributions from both the external $\mathbf{B}_{ext}$ and the tip-
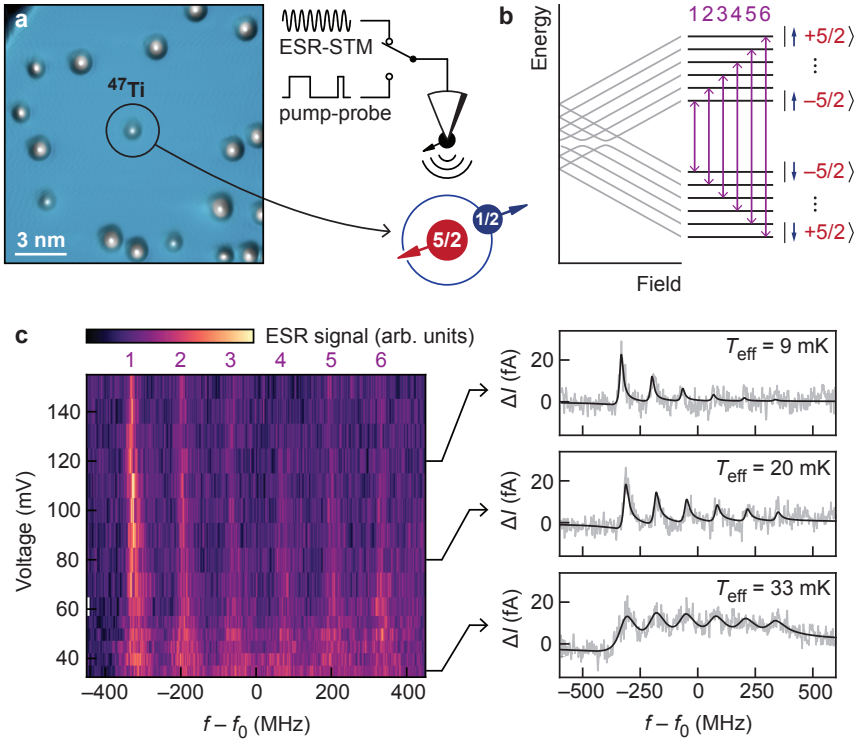
Figure 5.1: Single atom nuclear polarization. (a) STM topography of the single ^{47}TiH studied in this work. A schematic drawing shows the magnetic STM tip above the electron spin (blue) and nuclear spin (red) of the single atom. **(b)** Energy diagram of the spin states of a single ^{47}TiH. In the high field regime, the eigenstates resemble Zeeman product states. ESR transitions (green arrows) can be driven between states with equal nuclear spin. **(c)** ESR-STM measurements at different applied DC bias (T = 1.5 K, B_{ext} = 1.5 T, V_{RF} = 25 mV, I_{set} = 2.5 pA, f_0 = 11.5 − 12.56 GHz). Line traces at 35 mV, 80 mV and 120 mV are shown with fits using six Fano lineshapes scaled by the Boltzmann factor in order to extract an effective temperature.

induced magnetic field $\mathbf{B}_{tip}$. We neglect the effect of either of these fields on the nuclear spin, since their contributions are small compared to the other terms. In Fig. 5.1b we show the general behavior of the interplay between the hyperfine coupling and an external magnetic field. In the low field regime, the hyperfine coupling energy dominates and the system displays avoided crossings between the different energy levels indicating superposition states. In the high field regime, we retrieve the Zeeman spin states as eigenstates.

5.3. STATE INITIALIZATION VIA SPIN PUMPING

We start our investigation by applying a magnetic field of 1.5 T, which is large compared to the hyperfine interaction, in order to drive ESR transitions between the individual spin states of a ^{47}Ti atom. Similar to measurements of Ti on a bridge binding site of MgO [23, 24], we find a large anisotropy in the hyperfine coupling $\mathbf{A}$ = [11, 11, 128] ± 2 MHz.

Since we aim for a regime in which the hyperfine interaction competes with the Zeeman splitting of the electron, the experiments are performed with an out-of-plane magnetic field.

For certain magnetic tips , we observe that the hyperfine-split ESR peaks have different intensities, which indicates a strong polarization of the nuclear spin. This effect is well known in bulk NMR techniques as hyperpolarization[25, 26] and has been observed before on the atomic scale for single Cu atoms on MgO[20]. The phenomenon is explained by taking into account inelastic spin scattering events between the tunneling electrons and electron spin which are transmitted to the nucleus via the hyperfine flip-flop interaction. As shown in Fig. 5.1c, we find that the polarization is strongly dependent on the applied bias voltage while measuring at constant current. We believe that this may be due to the bias-dependent efficiency of the spin scattering channels involved, but a more complex mechanism involving the Ti orbital excitation[16] or Pauli spin blockade[27] may be at play. We find that the effective temperature of the nuclear spin population drops below 10 mK at voltages larger than 100 mV, more than two orders of magnitude lower than the actual experimental temperature of 1.5 K. While the effect of nuclear spin pumping has been observed for Cu on MgO[6], we here utilize it to overcome a major limitation: in previous ESR-STM experiments, the frequency ranges investigated were chosen to be compatible with sufficient spin population contrast set by the Boltzmann distribution at the experimental temperature. Finally, we point out that high bias voltages are key for efficient nuclear spin pumping, which – with few exceptions[28] – has usually not been used in previous experiments involving Ti on MgO.

5.4. TUNING ELECTRON-NUCLEAR SPIN ENTANGLEMENT

Owing to the spin pumping we can investigate a much lower frequency regime, down to ~50 MHz, in which the level of entanglement between the electron and nuclear spins can be tuned. In Fig. 5.2a, we show the different calculated contributions to the energy diagram of a ^{47}Ti in a low-field regime. For the calculations we use $\mathbf{A}$ = [10,10,130] MHz and $\mathbf{Q}$ = [1.5,1.5,-3] MHz in accordance with the measurements performed in a vector field (see Sec. 5.7.1). When the total electronic Zeeman energy – due to the external and tip magnetic field – is comparable to the hyperfine splitting, multiple avoided level crossings occur in the spectrum. The number of avoided crossings has increased compared to Fig. 5.1b which is due to a misalignment between the external field and the tip field. More precisely, an additional avoided crossing appears around B_{tip} = 23 mT, involving a superposition of states that differ only in the electron spin projection, while the nuclear spin is the same. This electron-only hybridization will be of importance below.

We identify these tuning points in our experiment by performing ESR measurements in the low field regime using an external field of merely 20 mT (Fig. 5.2b). Here, in order to fine-tune the coupled spin system, we vary the tip-induced magnetic field by changing the DC voltage while keeping the current constant. This effectively tunes the junction conductance G. At relatively large tip fields ($G \geq 20$ pS) multiple ESR peaks are visible in addition to several very sharp (~3 MHz) NMR type resonances around 60 MHz. Below $G \approx 20$ pS, the ESR and NMR transitions start to mix and overlap, accompanied by a redistribution of their intensities as shown in the close-up measurements in Fig. 5.2c. This is consistent with the presence of avoided level crossings between the energy
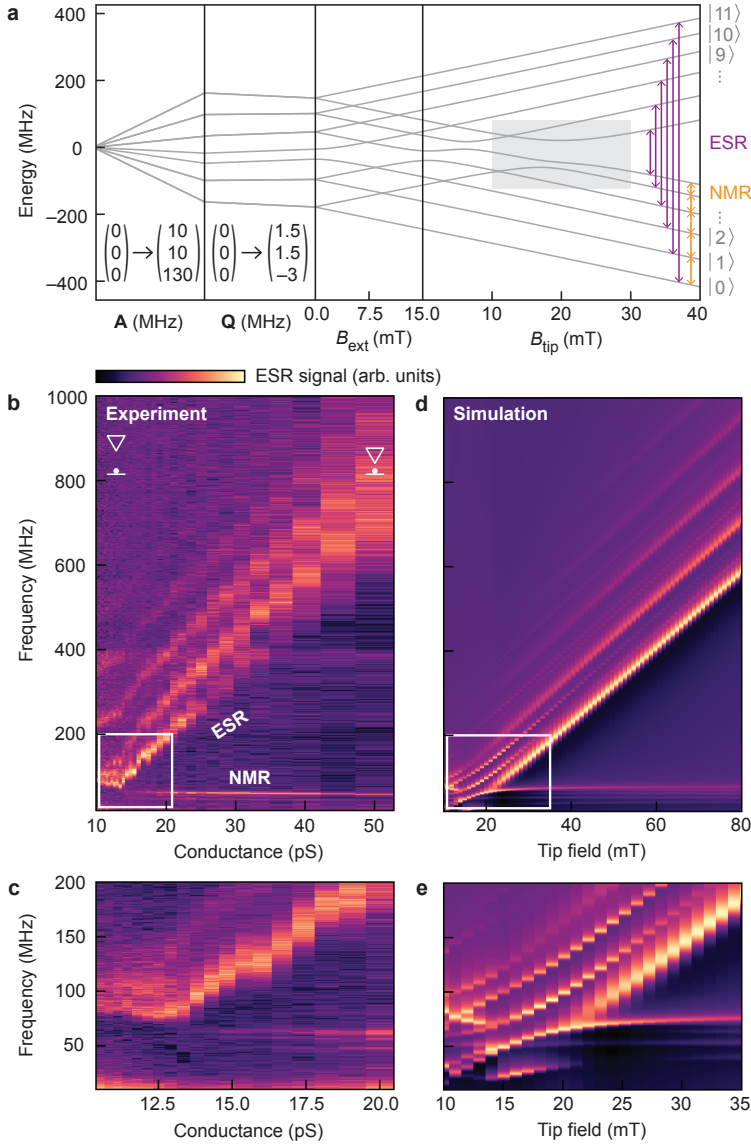
Figure 5.2: ESR and NMR-type measurements in the low-field regime. (a) Energy diagram of the atomic eigenstates as a function of hyperfine coupling, quadrupole moment, external and tip-induced magnetic field. **(b)** ESR-STM measurements showing ESR and NMR-type transitions ($T = 400$ mK, $B_{ext} = 20$ mT, $V_{RF} = 40$ mV, $I_{set} = 2$ pA). The bottom close-up is a separate dataset showing the splitting of the NMR transitions and a curve upwards of the bottom ESR transition signaling the avoided level crossing. **(c)** Simulations of the ESR-STM measurements (see 5.7.2 for details).

levels, as expected from Fig. 5.2a and modelled in Figs. 5.2d and E. In Fig. 5.2c, we also observe that the NMR type resonances are split into multiple peaks. We attribute this to the quadrupole interaction that slightly shifts the energy of each nuclear spin state[19]
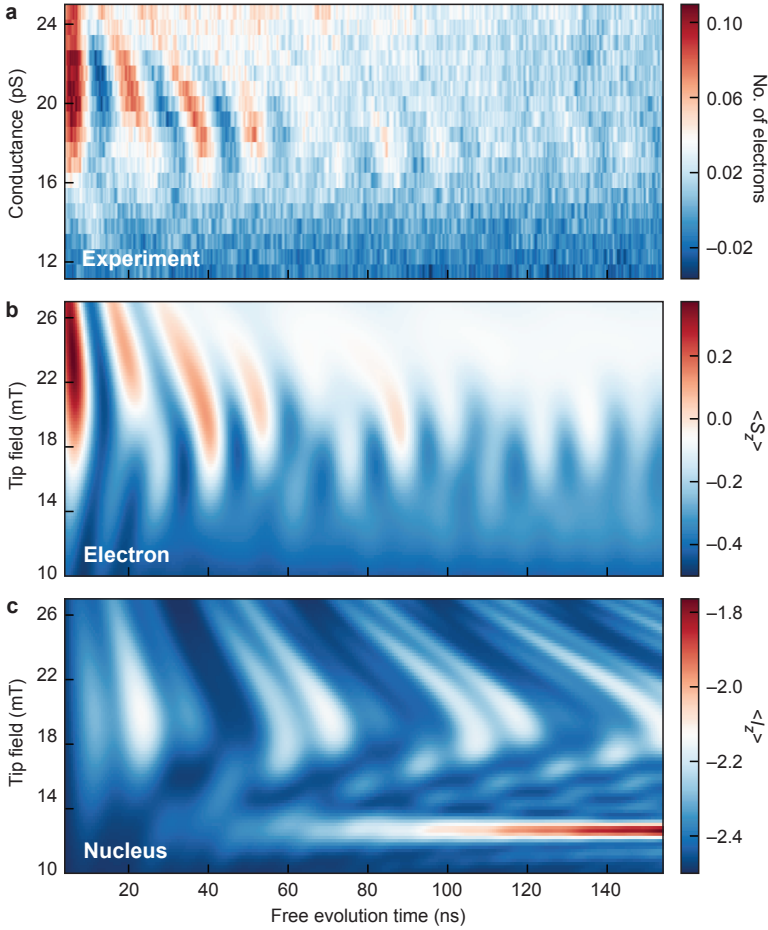
Figure 5.3: Free evolution measurements and Lindblad simulations. (a) Pump-probe data for different tip-atom distances set by the junction conductance (V_{set} = 130 mV, T = 400 mK, B_{ext} = 15 mT). **(b)** Lindblad simulation of the free time evolution of the electron spin when initialized to $|\downarrow, -\frac{5}{2}\rangle$. **(c)** Corresponding Lindblad simulation of the free time evolution of the nuclear spin. The calculations also show the onset of an additional oscillation in the nuclear spin at around 13 mT. However, since the period is an order of magnitude longer than the coherence time of the electron spin, it is not visible in our measurements.

For the simulations we consider both ESR and NMR transitions with separately scaled intensities (see 5.7.2).

5.5. PROBING COHERENT SPIN DYNAMICS

Having identified 10 to 20 pS as the appropriate tip-atom distances for inducing super-position states, we perform DC pump-probe experiments to explore the coupled spin dynamics. In order to increase signal amplitudes, we decrease the external field to 15 mT so that the superposition states are induced at closer tip-atom distances while using

the same microtip. We use a two-pulse pumping sequence to initialize both electron and nuclear spin states. During the pump pulses, spin polarized electrons cause spin-flip excitations in the atom by scattering with the atom's electron spin [29]. Due to the hyperfine coupling, the excitations will also affect the nuclear spin, polarizing it in the same direction[20]. Consequently, the combined system will be projected to a Zeeman state, $|\downarrow, -5/2\rangle$ which is not necessarily a stationary eigenstate of the Hamiltonian of Eq. 1. To probe any dynamics that might occur after the pump pulses, we then let the system evolve freely during a waiting time after which the electron spin is read out by a 5 ns probe pulse. By varying the waiting time over the course of many iterations, the dynamic evolution of the electron spin is measured[8].

Using this pulse scheme we observe electron spin dynamics that, as shown in Fig. 5.3a, depend on the tip magnetic field. When the STM tip is close (i.e., at large conductance values) we observe fast, low-amplitude oscillations that become slower and stronger as the tip is retracted. This is the expected behavior when the system moves through an avoided crossing[22]. However, around $G = 17$ pS a beating pattern appears due to interference with a second frequency. At this point, the dynamics also appear to be longer lived compared to the single frequency oscillation. Upon further retraction of the tip, below $G = 15$ pS, no spin dynamics are detected anymore. The observed dynamics occur at slightly higher conductance values compared to the detected avoided crossing measured using ESR in Fig. 5.2. We attribute this difference to both the slightly lower external field used for the pump-probe measurements as well as the absence of a DC bias voltage in the pump-probe experiment, which has been shown to shift the electron energy levels[28].

Figs. 5.3b and C show the simulated time evolution of the S_z and I_z expectation values for the electron and the nuclear spin, respectively. The calculations are performed considering the Hamiltonian shown in equation (1) and using the Liouville-von Neumann equation starting from the $|\downarrow, -5/2\rangle$ state[30]. We find excellent agreement between the data from the experiment and the electronic spin calculations, with, in particular, a beating pattern that arises when the electron and nucleus states are entangled. While the electron shows an interference pattern, the simulation shows that the dynamics of nuclear spin are dominated by a ~40 ns oscillation.

To understand the origin of the different oscillations, we further analyze the composition of the three eigenstates forming the avoided crossings: states $|4\rangle$, $|5\rangle$ and $|6\rangle$. In Fig. 5.4a, we show an enhanced view of the relevant region of the eigenstate energies marked by the grey box in Fig. 5.2a. We then take two exemplary traces from the pump-probe data presented in Fig. 5.3a and match the frequencies present in the spin dynamics to the energy splitting between the eigenstates. From the composition of the eigenstates at these particular tip-field amplitudes we derive the nature of the different dynamics (see Sec. 5.7.3).

At a relatively large setpoint conductance of 21.5 pS, the pump-probe data fitted in Fig. 5.4c show a single damped sinusoid of roughly 75 MHz. This frequency matches both the energy of the lowest ESR transition measured at the avoided crossing point in Fig. 5.2b as well as the calculated energy splitting between states $|5\rangle$ and $|6\rangle$ at the relatively large tip field of roughly 24 mT (rightmost dotted line in Fig 5.4a). At this field, states $|5\rangle$ and $|6\rangle$ are split in energy by the in-plane component of the tip field and approximate the spin superposition states $|\uparrow, -5/2\rangle \pm |\downarrow, -5/2\rangle$. Therefore, the reduced density matrix
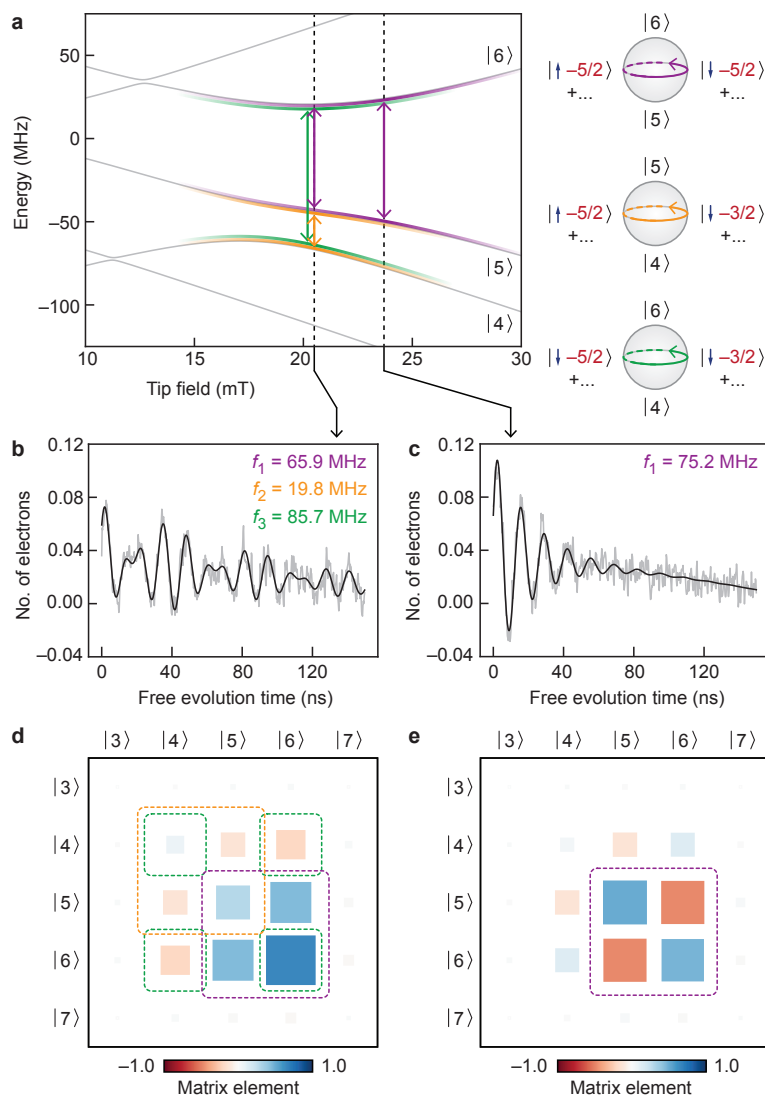
Figure 5.4: Origin of the beating pattern. (a) Zoom-in on the relevant avoided level crossings of Fig. 2a. The Bloch spheres illustrate the dominating dynamics arising from the superpositions of the corresponding states. **(b)** Fit to a line trace from the pump-probe data from Fig. 3a showing a beating pattern (G = 17.7 pS). The pattern arises from two dominating frequencies and their sum frequency. **(c)** Fit to a line trace from the pump-probe data from Fig. 3a showing a single frequency oscillation (G = 21.5 pS). **(d)** Reduced density matrix of the initial state $|\downarrow, -\frac{5}{2}\rangle$ at 20.5 mT tip field. **(e)** Reduced density matrix of the initial state $|\downarrow, -\frac{5}{2}\rangle$ at 23.7 mT tip field.

of the initial state $|\downarrow, -5/2\rangle$, shown in Fig. 5.4E, is dominated by coherences in the subspace between states $|5\rangle$ and $|6\rangle$. We can thus attribute the dominant frequency in the dynamics to a Larmor precession of the electron spin due to the in-plane component

of the tip field as depicted in the top Bloch sphere in Fig. 5.4a.

In contrast, at a setpoint conductance of 17.7 pS, we need three damped sinusoids to fit the data shown in Fig. 5.4b: two independent frequencies, 65.9 MHz and 19.8 MHz as well as their sum. These frequencies match the energy splitting between the three states $|4\rangle$, $|5\rangle$ and $|6\rangle$ at roughly 20 mT (leftmost dotted line in Fig 5.4a). The reduced density matrix of the initial state at this field, shown in Fig. 5.4d, show finite coherences between all three states. This means that in addition to the Larmor contribution described above, there are two additional terms. One is a flip-flop dynamic between electron and nucleus as the subspace between states $|4\rangle$ and $|5\rangle$ is dominated by $|\uparrow, -5/2\rangle \pm |\downarrow, -3/2\rangle$ (middle Bloch sphere in Fig. 5.4a). The other is an oscillation of the nuclear spin as the subspace between states $|4\rangle$ and $|6\rangle$ is dominated by $|\downarrow, -5/2\rangle \pm |\downarrow, -3/2\rangle$ (bottom Bloch sphere in Fig. 5.4a).

The reduced coupling of the nuclear spin to the environment, compared to the dynamics of only the electron spin, is expected to result in an enhanced coherence time[8, 31, 32]. Indeed, fits to the data shown in Fig. 5.4b result in an effective coherence time of 84 ± 5 ns, whereas the oscillation in Fig. 5.4c has an effective coherence time of only 22 ± 1 ns. However, we point out that this is only a lower limit to the intrinsic coherence time of the combined electron-nucleus spin system. We believe that the main source of spin decoherence in our experiment is fluctuations of the magnetic field emanating from the tip caused by mechanical vibrations in the setup on the sub-picometer scale. The observed changes in coherence time may in part result from a decreased sensitivity to this magnetic tip field noise since the energy levels in Fig. 5.4a diverge less at 21 mT than at 23 mT, akin to a clock-transition[33, 34]. We expect that eliminating these vibrations may result in longer coherence times in pump-probe measurements.

5.6. Discussion

Developing single atom quantum information processing requires thorough understanding of the underlying electron and nuclear spin dynamics. This demands initialization, tuning and readout tailored on the atomic length scale. Using pump-probe spectroscopy, we revealed the collective coherent dynamics of the internal spin dynamics inside a single atom. The magnetized STM tip functioned in this work as a control knob to locally tune the nature of these dynamics. This technique has the potential to be extended to a great variety of on-surface atomic or molecular spin system. Moreover, the prospect of STM for engineering bottom-up atomic designer assemblies can provide an integral atomic-scale understanding into the fundamentals of complex coherent spin dynamics.

5.7. Simulation details

5.7.1. Hamiltonian parameters

The Hamiltonian used to calculate the eigenstates of the Ti spin system as well as the energies of the ESR transitions and the coherent evolution dynamics is presented in Eq. 5.1. In table 5.1 we summarize the parameters used to calculated the eigenstates of the system.
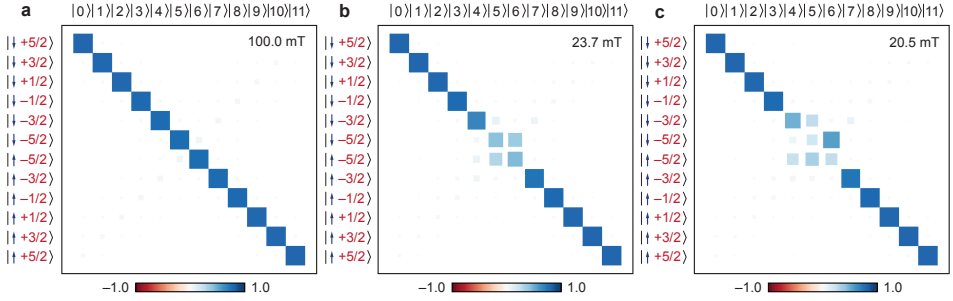
Figure 5.5: Energy eigenstates. All are expressed in the probability amplitudes of the Zeeman product states and calculated for an external field of 15 mT. **(a)** at a tip field of 100 mT, the energy eigenstates almost perfectly resemble the Zeeman product states. **(b)** at the avoided crossing of 23.7 mT studied in the main text, states 5 and 6 become superpositions of the Zeeman product states. **(c)** at the avoided of 20.5 mT states 4, 5 and 6 become superpositions of the Zeeman product states.

$A(x, y, z)$	$Q(x, y, z)$	B_{ext}	B_{tip}
(10, 10, 130) MHz	(1.5, 1.5, -3) MHz	0.015 to 1.5 T	0 to 35 mT

Table 5.1: Hamiltonian parameters

In Fig. 5.5 we plot the probability amplitude of the energy eigenstates in the basis of the Zeeman product states: $|\langle s, n|\psi\rangle|^2$, s and n being the z-components of the electron and nuclear spins, respectively. There, we can clearly see the influence of the tip field on the energy eigenstates. At large fields (panel a), the Zeeman energy dominates over the hyperfine coupling and the energy eigenstates coincide with the Zeeman basis states. When we lower the applied tip field, the hyperfine coupling starts to compete with the Zeeman energy and we observe avoided crossings between the energy eigenstates as a function of applied field (also Fig. 5.2a). In panel B of Fig. 5.5, we show the eigenstates at the first avoided crossing of 23.7 mT tip field. There, energy eigenstates $|5\rangle$ and $|6\rangle$, form superpositions of two Zeeman product states $|\uparrow, -5/2\rangle$ and $|\downarrow, -5/2\rangle$. At 20.5 mT tip field (panel C), we find a more complex situation where states $|4\rangle$, $|5\rangle$ and $|6\rangle$ form different superpositions of the Zeeman basis states $|\uparrow, -5/2\rangle$, $|\downarrow, -3/2\rangle$ and $|\downarrow, -5/2\rangle$.

5.7.2. Simulations of ESR results

ESR simulations were done by generating Fano functions for each possible spin transition between two eigenstates. The eigenstates were calculated using the Hamiltonian presented in the main text, using the experimental external field of 20 mT out of plane. The amplitude I_{nm} of a transition between states $|m\rangle$ and $|n\rangle$ was calculated by:

$$I_{nm} \propto (|V_{nm}^{ESR}|^2 + p|V_{nm}^{NMR}|^2)\Delta P_{nm}\{\mathbf{B}_{tip} \cdot (\langle n|\hat{\mathbf{S}}|n\rangle - \langle m|\hat{\mathbf{S}}|m\rangle)\}. \qquad (5.2)$$

This amplitude consists of three components. The part between curly brackets is the readout strength, which scales with the difference in expectation value of each spin between the two states, projected onto the measurement axis. The first part corresponds

to the driving amplitude between the two states. To achieve a result that matches the experiment we distinguish here between ESR and NMR type transitions and add them with a separate scaling factor p. The two different driving terms are modelled by [35]:

$$\begin{aligned} V_{nm}^{ESR} &= \langle n | \nabla \mathbf{B}_{tip} \cdot \widehat{\mathbf{S}} | m \rangle \\ V_{nm}^{NMR} &= \langle n | \nabla \mathbf{B}_{tip} \cdot \widehat{\mathbf{I}} | m \rangle \end{aligned} \tag{5.3}$$

We found the simulations to match the experimental results best when using a ratio $p = 10$. This difference in driving amplitudes may be explained by the nuclear spin having significant longer relaxation and coherence times than the electron spin, since as in eq. S3 of Ref. [35] in the weak driving limit the ESR signal scales with $T_1 T_2$ of the driven spin transition.

The population difference ΔP_{nm} is calculated by finding the steady state solution to the time dependent rate equations for the coupled spin system connected to a spin polarised bath (tip, t) and a spin average bath (sample, s)[36]:

$$\frac{dP_n(\tau)}{d\tau} = \sum_m r_{nm} P_m(\tau) - r_{mn} P_n(\tau). \tag{5.4}$$

Here, in general, the rates r include all possible spin scattering processes between the free electrons of the two baths and the coupled spin system. However, since the nuclear spin is weakly coupled to the environment compared to the electron spin, we neglect all direct scattering processes with the nuclear spin. Moreover, tip-tip scattering events are neglected as the experimental tip-sample distances are comparatively large. This leaves only the following electron spin scattering rates

$$r_{nm} = r_{nm}^{s \to s} + r_{nm}^{t \to s} + r_{nm}^{s \to t} \tag{5.5}$$

The first rate is bias-independent and describes spontaneous relaxation due to sample electrons scattering with the Ti electrons spin and returning to the sample:

$$r_{nm}^{s \to s} = \int f(\varepsilon) \left(1 - f(\varepsilon)\right) \sum_{\sigma, \sigma'} \left| \left\langle n, \sigma \left| \widehat{\mathcal{H}_s} \right| m, \sigma' \right\rangle \right|^2 d\varepsilon. \tag{5.6}$$

The second and third are bias-dependent and describe scattering of tunnelling electrons between tip and sample:

$$r_{nm}^{s \to t} = \int f(\varepsilon) \left(1 - f(\varepsilon) + V\right) \sum_{\sigma, \sigma'} \rho_\sigma^t \left| \left\langle n, \sigma \left| \widehat{\mathcal{H}_s} \right| m, \sigma' \right\rangle \right| \left| \left\langle n, \sigma \left| \widehat{\mathcal{H}_t} \right| m, \sigma' \right\rangle \right| d\varepsilon \tag{5.7}$$

$$r_{nm}^{t \to s} = \int f(\varepsilon + V) \left(1 - f(\varepsilon)\right) \sum_{\sigma, \sigma'} \rho_{\sigma'}^t \left| \left\langle n, \sigma \left| \widehat{\mathcal{H}_t} \right| m, \sigma' \right\rangle \right| \left| \left\langle n, \sigma \left| \widehat{\mathcal{H}_s} \right| m, \sigma' \right\rangle \right| d\varepsilon \tag{5.8}$$

Here, in all cases the first part concerns the Fermi statistics of the baths with $f(\varepsilon)$ being the Fermi-Dirac function and V the bias. The second term is the transition element

of each specific scattering process, where σ sums over all possible initial and final states of the scattering bath electron, which can either be +/- ½. The tip-dependent transition elements are appropriately weighted by the tip polarization η as captured in the tip spin density $\rho_\sigma^t = \frac{1}{2} + \eta\sigma$.

For each of the transition elements the governing Hamiltonians $\mathscr{H}$ are Kondo Hamiltonians

$$\widehat{\mathscr{H}}_{t/s} = J_{t/s}\widehat{\mathbf{S}} \cdot \widehat{\sigma}_{t/s} \tag{5.9}$$

Where $\widehat{\mathbf{S}}$ is the surface electron spin and $\widehat{\sigma}_{t/s}$ the local spin density of the tip or sample bath and $J_{t/s}$ the coupling between the bath and surface spin. We find the best agreement with experiment using $\varrho^s J_s = 0.1$ and $\varrho^t J_t = 10^{-5}$, with $\varrho^{t/s}$ the bath electron density, confirming it is justified to neglect $r^{t \to t}$.

5.7.3. SPIN DYNAMICS SIMULATIONS

To simulate the expected time dynamics of the coupled electron-nuclear spin system we solve the Liouville–von Neumann equation using a python package called QuTiP[30]. We solve for the Hamiltonian presented in the main text for different values of the applied tip field while keeping the experimental external field value external field constant at the experimental value of 15 mT :

$$\frac{d\widehat{\rho}(t)}{dt} = -\frac{i}{\hbar}\left[\widehat{\mathscr{H}}, \widehat{\rho}(t)\right]. \tag{5.10}$$

The density operator is constructed from the presumed initial state after the pump pulse sequence as follows:

$$\widehat{\rho} = |\downarrow, -5/2\rangle\langle\downarrow, -5/2| \tag{5.11}$$

As mentioned in the main text, the dominant source of decoherence in our experiments results from stochastic fluctuations of the magnetic field of the STM tip due to mechanical vibrations in the setup on the sub-picometer scale. To emulate this effect, we convolve the simulated data in the tip field axis with a 2 mT Gaussian.

From the match between experiment and simulation presented in Fig. 5.3 in the main text, we conclude that the initial state indeed must be dominated by the spin state $|\downarrow, -5/2\rangle$.

5.8. DATA AVAILABILITY

The raw data generated in this study as well as the analysis and simulation code have been deposited in a Zenodo database under identifier `https://doi.org/10.5281/zenodo.8316339`.

5.9. ACKNOWLEDGEMENTS

5.10. AUTHOR CONTRIBUTIONS

LMV, LF and SO conceived the experiment. LMV, MPC and EWS performed the measurements. LMV, MPC and RB performed the calculations. All authors analyzed and discussed the results. LMV, LF, PW and SO wrote the manuscript, with input from all authors. SO supervised the project.

REFERENCES

[1] Vincent, R., Klyatskaya, S., Ruben, M., Wernsdorfer, W. & Balestro, F. Electronic readout of a single nuclear spin using a molecular spin transistor. *Nature* **488**, 357–360 (2012).

[2] Thiele, S. *et al.* Electrically driven nuclear spin resonance in single-molecule magnets. *Science* **344**, 1135–1138 (2014).

[3] Neumann, P. *et al.* Single-shot readout of a single nuclear spin. *science* **329**, 542–544 (2010).

[4] Fuchs, G., Burkard, G., Klimov, P. & Awschalom, D. A quantum memory intrinsic to single nitrogen–vacancy centres in diamond. *Nature Physics* **7**, 789–793 (2011).

[5] Pla, J. J. *et al.* High-fidelity readout and control of a nuclear spin qubit in silicon. *Nature* **496**, 334–338 (2013).

[6] Randall, J. *et al.* Many-body–localized discrete time crystal with a programmable spin-based quantum simulator. *Science* **374**, 1474–1478 (2021).

[7] Maze, J. R. *et al.* Nanoscale magnetic sensing with an individual electronic spin in diamond. *Nature* **455**, 644–647 (2008).

[8] Zaiser, S. *et al.* Enhancing quantum sensing sensitivity by a quantum memory. *Nature communications* **7**, 12279 (2016).

[9] Žutić, I., Fabian, J. & Sarma, S. D. Spintronics: Fundamentals and applications. *Reviews of modern physics* **76**, 323 (2004).

[10] Wernsdorfer, W. & Ruben, M. Synthetic hilbert space engineering of molecular qudits: Isotopologue chemistry. *Advanced Materials* **31**, 1806687 (2019).

[11] Kane, B. E. A silicon-based nuclear spin quantum computer. *nature* **393**, 133–137 (1998).

[12] Yang, S. *et al.* High-fidelity transfer and storage of photon states in a single nuclear spin. *Nature Photonics* **10**, 507–511 (2016).

[13] Baumann, S. *et al.* Electron paramagnetic resonance of individual atoms on a surface. *Science* **350**, 417–420 (2015).

[14] Willke, P., Yang, K., Bae, Y., Heinrich, A. J. & Lutz, C. P. Magnetic resonance imaging of single atoms on a surface. *Nature Physics* **15**, 1005–1010 (2019).

[15] Yang, K. *et al.* Engineering the eigenstates of coupled spin-1/2 atoms on a surface. *Physical Review Letters* **119**, 227206 (2017).

[16] Steinbrecher, M. *et al.* Quantifying the interplay between fine structure and geometry of an individual molecule on a surface. *Physical Review B* **103**, 155405 (2021).

[17] Yang, K. *et al.* Coherent spin manipulation of individual atoms on a surface. *Science* **366**, 509–512 (2019).

[18] Wang, Y. *et al.* Universal quantum control of an atomic spin qubit on a surface. *npj Quantum Information* **9**, 48 (2023).

[19] Willke, P. *et al.* Hyperfine interaction of individual atoms on a surface. *Science* **362**, 336–339 (2018).

[20] Yang, K. *et al.* Electrically controlled nuclear polarization of individual atoms. *Nature nanotechnology* **13**, 1120–1125 (2018).

[21] Yang, K. *et al.* Tuning the exchange bias on a single atom from 1 mt to 10 t. *Physical Review Letters* **122**, 227203 (2019).

[22] Veldman, L. M. *et al.* Free coherent evolution of a coupled atomic spin system initialized by electron scattering. *Science* **372**, 964–968 (2021).

[23] Farinacci[†], L., Veldman[†], L. M., Willke, P. & Otte, S. Experimental determination of a single atom ground state orbital through hyperfine anisotropy. *Nano Letters* **22**, 8470–8474 (2022).

[24] Kim, J. *et al.* Anisotropic hyperfine interaction of surface-adsorbed single atoms. *Nano Letters* **22**, 9766–9772 (2022).

[25] Cassidy, M., Chan, H., Ross, B., Bhattacharya, P. & Marcus, C. In vivo magnetic resonance imaging of hyperpolarized silicon particles. *Nature nanotechnology* **8**, 363–368 (2013).

[26] Eills, J. *et al.* Spin hyperpolarization in modern magnetic resonance. *Chemical reviews* **123**, 1417–1551 (2023).

[27] McMillan, S. R., Harmon, N. J. & Flatté, M. E. Image of dynamic local exchange interactions in the dc magnetoresistance of spin-polarized current through a dopant. *Physical review letters* **125**, 257203 (2020).

[28] Kot, P. *et al.* Electric control of spin transitions at the atomic scale. *Nature Communications* **14**, 6612 (2023).

[29] Loth, S., Etzkorn, M., Lutz, C. P., Eigler, D. M. & Heinrich, A. J. Measurement of fast electron spin relaxation times with atomic resolution. *Science* **329**, 1628–1630 (2010).

[30] Johansson, J. R., Nation, P. D. & Nori, F. Qutip: An open-source python framework for the dynamics of open quantum systems. *Computer Physics Communications* **183**, 1760–1772 (2012).

[31] Degen, C. L., Reinhard, F. & Cappellaro, P. Quantum sensing. *Reviews of modern physics* **89**, 035002 (2017).

[32] Savytskyy, R. *et al.* An electrically driven single-atom "flip-flop" qubit. *Science Advances* **9**, eadd9408 (2023).

[33] Bae, Y. *et al.* Enhanced quantum coherence in exchange coupled spins via singlet-triplet transitions. *Science Advances* **4**, eaau4159 (2018).

[34] Shiddiq, M. *et al.* Enhancing coherence in molecular spin qubits via atomic clock transitions. *Nature* **531**, 348–351 (2016).

[35] Yang, K. *et al.* Probing resonating valence bond states in artificial quantum magnets. *Nature communications* **12**, 993 (2021).

[36] Loth, S. *et al.* Controlling the state of quantum spins with electric currents. *Nature Physics* **6**, 340–344 (2010).

5

6

PROTOCOL FOR CERTIFYING ENTANGLEMENT IN SURFACE SPIN SYSTEMS USING A SCANNING TUNNELING MICROSCOPE

A true gentleman leaves no puzzle unsolved

Professor Layton

Rik Broekhoven, Curie Lee, Soo-Hyon Phark, Sander Otte, Christoph Wolf

Certifying quantum entanglement is a critical step toward realizing quantum-coherent applications. In this work, we show that entanglement of spins can be unambiguously evidenced in a scanning tunneling microscope with electron spin resonance by exploiting the fact that entangled states undergo a free time evolution with a distinct characteristic time constant that clearly distinguishes it from the time evolution of non-entangled states. By implementing a phase control scheme, the phase of this time evolution can be mapped back onto the population of one entangled spin, which can then be read out reliably using a weakly coupled sensor spin in the junction of the scanning tunneling microscope. We demonstrate through open quantum system simulations with currently available spin coherence times of $T_2 \approx 300$ ns, that a signal directly correlated with the degree of entanglement can be measured at temperatures of 100–400 mK accessible in sub-Kelvin scanning tunneling microscopes.

6.1. INTRODUCTION

Recent advances in quantum control of surface spin systems have shown that this platform can be used to design quantum-coherent systems by tailoring the interaction of individual spins using the scanning tunneling microscope (STM) and atom manipulation.[1, 2] In such a system, quantum coherent control of single and multiple spins has been achieved by electron spin resonance (ESR), which is facilitated by resonant electric fields in the STM. [3–8] When combining the atomic manipulation aspect and quantum coherent control, one can envision that this platform can be used to implement a reconfigurable quantum simulator in hardware using only a few atoms and an ESR-STM. By utilizing up to three titanium (Ti) atomic spins, some of us have demonstrated fundamental quantum gate operations such as controlled-NOT (CNOT) and controlled-controlled-NOT (CC-NOT) gates on two layers of magnesium oxide (MgO) [9]. The next logical step is to certify entanglement in this atomic qubit platform, which is a strong prerequisite for studying quantum-coherent phenomena beyond individual quantum gate operations[10]. This, however, is not straightforward in the ESR-STM since it only allowsfor time-averaged single spin readout with long measurement times (ms or kHz),[11] compared to the typical time-scale for coherence time (T_2) of only several hundred nanoseconds.[4, 12] Previous works [13] have suggested to use the magnetic susceptibility as entanglement witness, however no experimental realization of this idea has yet been shown. Alternatively, one could exploit the fact that states that are not eigenstates of the system undergo a time evolution that can be probed by the time-averaging measurement of the STM as previously shown for the free time-evolution of spins initialized by bias voltage pulses in a system tuned to singlet-triplet eigenstates.[14] In a similar manner one can use radio-frequency pulses in an ESR-STM to create entangled states that are no longer eigenstates in the Zeeman basis of the constituent spins, and therefore will undergo a time evolution that is distinctively different from the evolution of non-entangled states. This approach, also called phase reversal tomography,[15] has been previously applied to phosphorous donor semiconductor qubits[16]. Here, we present how to adapt and optimize this method for ESR-STM, which relies on the fact that ESR-STM has highly sensitive population read out[6]. By using open quantum systems simulations and parameters compatible with typical experiments we demonstrate that surface spins can be entangled with high fidelity at sufficiently low temperature.

6.2. CREATING AND MEASURING ENTANGLEMENT

It has been established that ESR-STM provides a universal gate set based on single-spin (or qubit) phase control [17] and controlled-NOT gates.[9] In the following, we will discuss how to create entanglement in a surface spin system and subsequently measure it. We start from two weakly interacting spins, which can be realized in the experiment by using two Ti atoms.[2, 6] We require that the interaction between these spins is sufficiently weak so that their combined eigenstates can be written in good approximation as Zeeman product states, e.g. $|\uparrow\rangle_A \otimes |\uparrow\rangle_B = |\uparrow\uparrow\rangle$, where $\uparrow$ ($\downarrow$) denotes the ground (excited state) of each spin, the subscripts A, B label the two spins, and $\otimes$ denotes the tensor product. As shown in Fig. 6.1a, two spins $|\uparrow\uparrow\rangle$ can be entangled by a Hadamard gate H followed by a negative controlled-NOT gate (CNOT=$|\uparrow\rangle\langle\uparrow| \otimes \mathbb{1} + |\downarrow\rangle\langle\downarrow| \otimes \sigma_x$), resulting in an entangled

state $|\uparrow\downarrow\rangle + |\downarrow\uparrow\rangle$. In order to detect this entanglement, we can now exploit the fact that the entangled state is not an eigenstate of the Zeeman product basis and thus undergoes a free evolution.[14] During this evolution the state picks up a phase at a rate that is proportional to the energy splitting between $|\uparrow\downarrow\rangle$ and $|\downarrow\uparrow\rangle$ (Fig. 6.1b). The accumulated phase is distinct from the free evolution of any other non-entangled state and thus allows to uniquely witness the state as being entangled. In particular, states that are maximally correlated but not entangled have no accumulated phase. We can measure the phase through a Bell state disentanglement measurement, realized by a CNOT followed by a Hadamard, which projects the phase onto one of the two spins followed by read-out of that spin. To be more precise the $|\uparrow\downarrow\rangle + |\downarrow\uparrow\rangle$ is projected upon $|\uparrow\downarrow\rangle$ whereas $|\uparrow\downarrow\rangle - |\downarrow\uparrow\rangle$, which has a phase of π, is projected upon $|\uparrow\uparrow\rangle$. The full protocol is illustrated in Fig. 6.1a. By repeating the scheme with increasing delay times between the entanglement and disentanglement sequences we can probe the full phase accumulation during free evolution. For the maximally entangled state it shows up as a slow (relative to the Larmor frequencies of the individual spins) variation of $\langle S_z \rangle$ as shown in Fig. 6.1c obtained from an analytical solution of the 4x4 density matrix shown in the inset. This variation can be read-out through the sensor-spin, where $\langle S_z \rangle \propto \Delta I^{ESR}$, i.e. the change in the tunneling current at spin resonance in the ESR-STM experiment[6]. In contrast, the maximally correlated state will result in a flat signal (Fig. 6.1d). To directly and unambiguously evidence entanglement, one has to ensure that the measurement gives an oscillation of spin A whereas spin B stays constant. In a practical implementation, probing free evolution might be slightly disadvantageous when the evolution time is either very short and approaches typical rise and fall times of the signal generator, or very long and rivals the coherence times T_2. Fortunately, the effect of free evolution can also be captured by adjusting the phase ϕ on the second CNOT gate $X(\phi)$ such that $\phi = \tau/\Delta E$. In the following, we will use such as phase-sweep instead of a delay-time sweep.

6.3. IMPLEMENTATION

We will now discuss some details of the implementation. All simulations were carried out using the QuTiP package in the Lindblad formalism using collapse operators parameterized by T_1 and T_ϕ for energy relaxation and pure dephasing of each spin, respectively (see Methods) [18]. The total system consists of three spin 1/2 (labeled A, B, R in Fig. 6.2a), which are exchanged coupled to one another sufficiently weakly so that the state diagram can be written in good approximations as Zeeman product states (details of the system can be found in the methods section). We emphasize that only spins A and B will be the target of this entanglement scheme while spin R acts as sensor for the readout. The Fe atoms are added in the experiment to provide the local field gradients for driving ESR of the remote spins (A and B)[6, 9].

To achieve the desired gate sequence for entanglement, we first combine two rotations (labeled as $X_{\frac{\pi}{2}}, Y_\pi$, where X, Y denote the rotation axes and the subscript specifies the rotation angle) to perform a Hadamard gate and then a single-frequency pulse X_π to perform a CNOT (Fig. 6.2b). Note that in general in this system a single driving frequency always performs a conditional operation while an unconditional NOT gate requires multi-frequency driving [9]. We found that at low enough temperatures single-frequency driving can be used for all gates due to negligible population in the excited states (Fig. 6.2b).
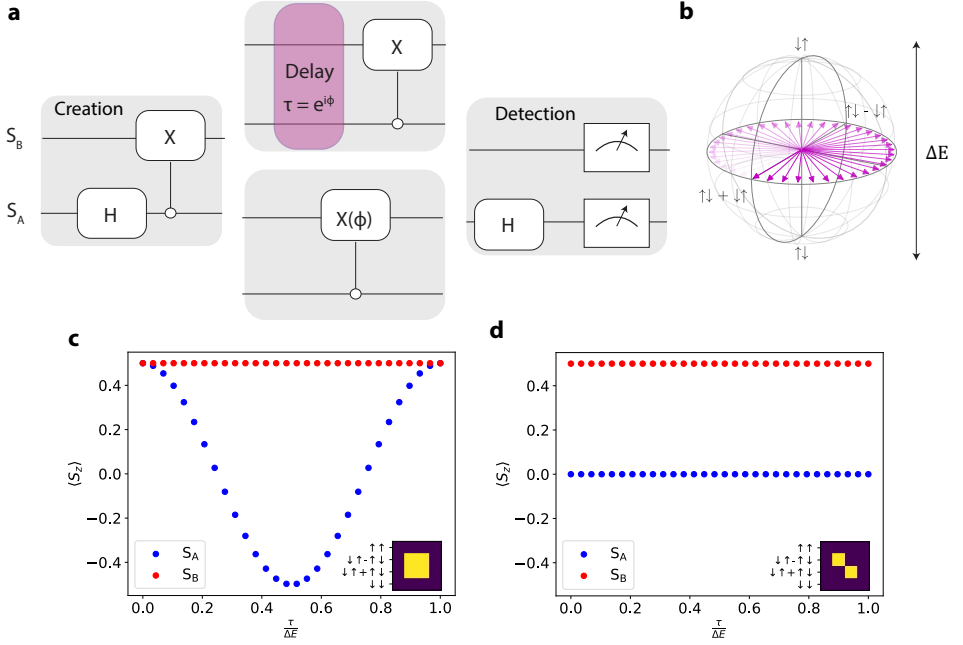
Figure 6.1: Sequence of quantum logic gates to demonstrate entanglement in ESR-STM. (a) vshows the pulse scheme using a quantum gate notation. From left to right this scheme applies a Hadamard gate to spin *A*, a negative CNOT gate, a pulse delay (or phase sweep) gate, followed by an disentangling gate scheme. Finally, both states can be measured to determine their respective populations. **(b)** the Bloch sphere shows the time-evolution of the entangled state on the equator. **(c)** expected measurement signal for spin *A* and spin *B* when entangled and, in contrast, **(d)** the same measurement for two spins that are not entangled as emphasized by the density matrix in the inset.

This no longer holds true at elevated temperatures, where excited states can have non-negligible populations. In such a case, the Hadamard gate results in an admixture of entangled states reflecting the excited state population. To avoid this, we also use single frequency driving for the Hadamard gate, which ensures that only the targeted fraction of population will be entangled, at the loss of overall signal amplitude. We have confirmed that this maximizes the readout of the sensor spin in our scheme and does not influence the outcome of the entanglement.

We drive all spins on resonance using a control field of the form $\Omega \cos(\omega_{RF} t + \phi)\hat{\sigma}_x$, with Ω the Rabi rate, ω_{RF} the angular radio-frequency resonant with a desired transition, ϕ an adjustable phase and $\hat{\sigma}_x$ the Pauli matrix. It was previously shown that this approach leads to efficient ESR in excellent agreement with the experiment [6]. For disentanglement we use the same gate sequence but in opposite order while matching the initial phase of each subsequent pulse to the phase of the previous pulse. The upper 3 panels of Fig. 6.2c show the expectation values for the spin operator $\langle S \rangle$ under these driving fields. We note that the appearance of filled areas is due to crosstalk of the driving frequencies of the pulses and the very fast Larmor precession (10-20 GHz) of each individual spin (see inset),

due to the choice that we implemented the simulation in a lab frame of reference. ϕ of the second CNOT was chosen to be π, so that it mimics half a free evolution in the entangled state resulting in a spin flip of A at the end of the scheme whereas spin B remains unchanged. At the point where the spin should be entangled the expectation value of $\langle S_z \rangle$ for A and B are 0, indicating that the spins lie at the equator of their Bloch spheres. To further confirm entanglement we also plot the concurrence $\mathscr{C}$, which is bounded by 0 for non-entangled and 1 for maximally entangled states.[19] For a bipartite qubit density matrix ρ_{AB}, $\mathscr{C}$ is straightforward to calculate and at the point of entanglement the concurrence approaches 1 for the chosen parameter set.

Read-out of the final target spin states is achieved by a long RF pulse on R conditioned on the spin state to be read out. In this part of the sequence quantum properties like the phase of the pulse play a lesser role, as the coherence of R is known to be limited by the conduction electrons.[6] Fig. 6.2b shows the transition that is driven for read-out of spin A. In the ESR-STM experiment a long DC voltage pulse could be used to measure the resulting oscillation as a change in the tunneling current ΔI^{ESR}. We set a fast decay time ($T_1 = 20$ ns) for R mimicking this DC pulse and make sure the measurement pulse is relatively long ($t_{\mathrm{meas}} = 100$ ns) such that R quickly reaches the steady state and the signal becomes only dependent on the spin which is read out. Note that we consider this relaxation only during the read-out since for the other parts of the scheme the DC pulse would not be present. The bottom panel of Fig. 6.2c shows the evolution of the sensor spin during read-out of spin A. The oscillation of A as a function of ϕ serves as a witness of entanglement and in Fig. 6.2c $\phi = \pi$ so that this oscillation is at its maximum. We refer to the maximum variation of the sensor spin as the measurement contrast $\mathscr{W}_R$. Due to the nature of the steady state it is at most half the amplitude of $\langle S_z \rangle$ of A. We see that in the present case the integrated signal of $\langle S_z \rangle$ of R approaches 0.5 within the measurement time. This shows that when the concurrence is 1 the read-out scheme gives the correct output for $\mathscr{W}_R$. A detailed discussion of the direct relation between $\mathscr{W}_R$ and $\mathscr{C}$ can be found in Sec. 6.10.1.

6.4. Results

The results in Fig. 6.3 demonstrate the concept in two ways: Fig. 6.3a shows the entire entanglement protocol while Fig. 6.3b contrasts the results for non-entangled spins. We will first consider results without any relaxation of spins A and B and at a very low temperature of 10 mK. Larmor frequencies, exchange couplings, and Rabi rates must be chosen such that we stay in the weakly coupled regime while limiting crosstalk, i.e. unwanted driving of other transitions depending on the realistic resonance line widths in the experiment. In addition, we want the Larmor frequencies to be as high as possible to ensure most of the population is in the ground state. Here, we limited the frequency range to $10-20$ GHz which is routinely achieved for single Ti spins on MgO surfaces ($S = 1/2$) in ESR-STM setups.[4, 20, 21] The system parameters are the same as in Fig. 6.2a. In Fig. 6.3c-f we show two resulting quantities: first, the variation of each target spin as directly obtained from the density matrix, which is evidence of the entanglement but is not accessible with the ESR-STM. Second, we show the expected readout signal $\mathscr{W}_R$, which is a direct observable of the experiment since for the sensor spin $\langle S_z \rangle \propto \Delta I^{\mathrm{ESR}}$. Contrasting both shows that while $\mathscr{W}_R$ is reduced, clearly the signal on the sensor spin directly reflects the spin dynamics in
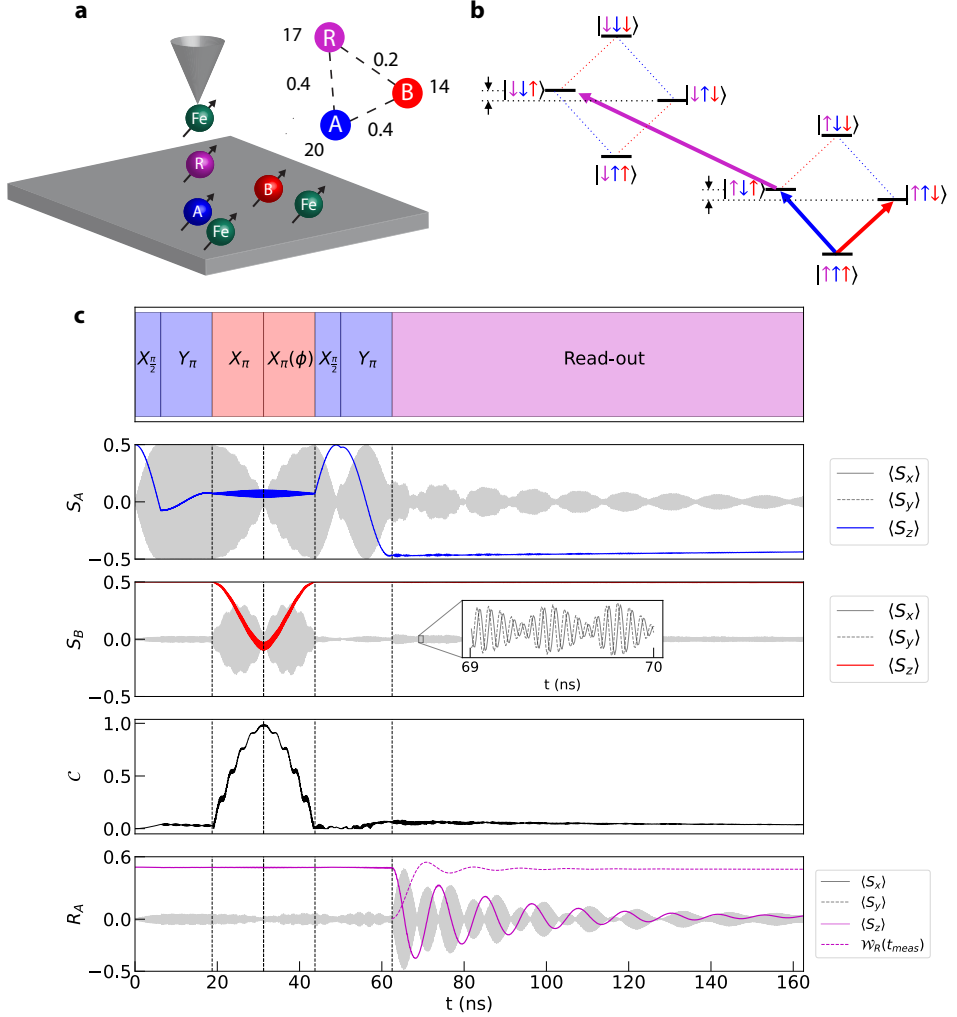
Figure 6.2: Two-spin entanglement scheme using sensor spin read-out. (a) Two relatively long-lived spins (A, B) are entangled while a third, short-lived sensor spin (*R*) is used for the read-out. Each pair of titanium and iron (Fe) atom serves as an effective qubit in the ESR-STM experiment. **(b)** energy level diagram showing CNOT (red), Hadamard (blue) spin control and read-out (purple). **(c)** actual pulse scheme as implemented in the simulations as well as expectation values along x, y, z for each spin involved in case of $\phi = \pi$. The top panel shows the implemented pulse scheme where X and Y represent the rotation axis and the subscript the rotation angle. The next two panels show the time-evolution of spins A and B under driving, followed by the concurrence $\mathscr{C}$ which serves as direct measure of entanglement in the simulation. The last panel shows the time-evolution of the sensor spin when reading out spin A as well as the corresponding time-averaged entanglement witness $\mathscr{W}_R(t_{\text{meas}})$. The entanglement witness reaches the steady state within the first ≈ 40 ns of the measurement time. Idealized parameters were used for clarity: $T = 10$ mK, $\Omega = 0.04$ GHz, $T_1^R = 20$ ns, no relaxation for A and B, and Larmor frequencies and exchange couplings are in GHz as indicated in panel (**a**)

the measurement scheme. We note that in this scheme the phase of the second Hadamard is swept by the equal amount of the free time-evolution, such that $\phi = \omega\tau$, where ω is the angular frequency associated with the entangled state. While the pulse sequence in Fig. 6.3a can be directly implemented, a real ESR-STM measurement also requires an empty cycle ('B-cycle'), which can be implemented as shown in Fig. 6.3b. In this cycle, the background current of the experiment can be measured by simply not entangling the states, which is achieved by removing the Hadamard gate during the entanglement step. We note that the choice of the B-cycle gate sequence is not unique and several different B-cycles are used in ESR-STM experiments (see also supplementary information VI). Finally, in Fig. 6.3e we show that the method is not limited to the $(|\downarrow\uparrow\rangle, |\uparrow\downarrow\rangle)$ subspace. Here, we initialize the system in $|\uparrow\downarrow\rangle$ such that the H and CNOT gate bring the overall target state to $|\uparrow\uparrow\rangle + |\downarrow\downarrow\rangle$. Note that here we drive $|\uparrow\downarrow\rangle$ to $|\downarrow\downarrow\rangle$ for H. The major difference in Fig. 6.3e when compared to Fig. 6.3c is that now the oscillation appears in the read-out of $|\uparrow_A\downarrow_B\rangle$ instead of $|\downarrow_A\uparrow_B\rangle$. This in turn allows to identify all the different Bell states in this system.
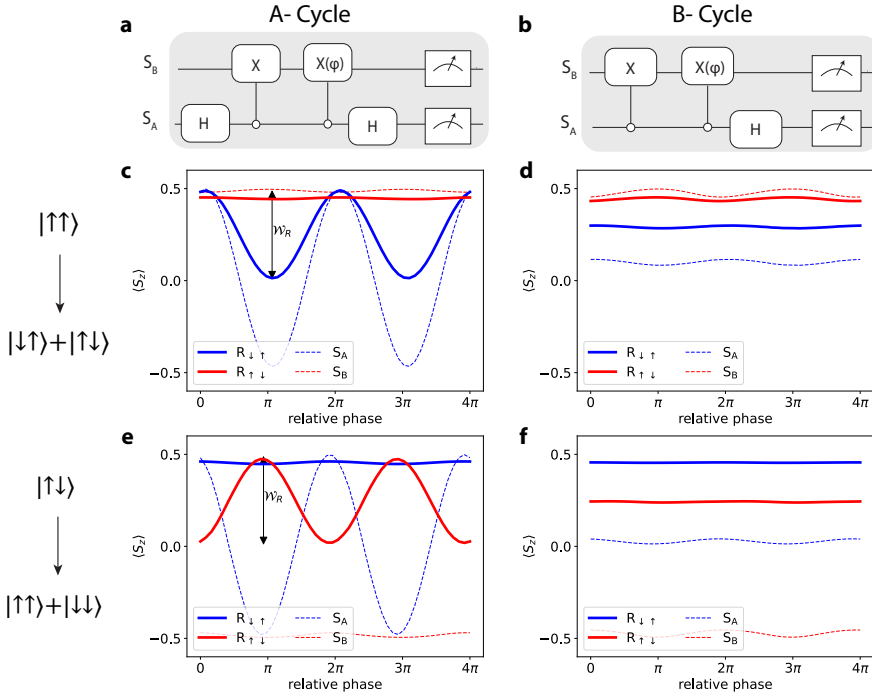
Figure 6.3: Simulations of two-qubit entanglement in ESR-STM. showing expected measurement outcomes, where we compare the expectation values $\langle S_z \rangle$ on each spin (inaccessible in the experiment) as well as the indirect readout $\mathcal{W}_R$ of these values through the sensor spin. From top to bottom (panels **a,c,e**) we compare the entangled subspace for different initial states ($|\uparrow\uparrow\rangle$, $|\uparrow\downarrow\rangle$). The panels **b, d, f** on the right side shows simulations for the same system but for not entangled states (achieved by removing the Hadamard gate), which could serve as empty cycle for the lock-in detection in the ESR-STM experiment. The system parameters are as shown in Fig. 6.2a, $T = 10$ mK, no relaxation for spins A, B, and $T_1 = 20$ ns for the sensor spin during read-out

We now turn to the effect of finite lifetime T_1 and elevated temperatures relevant to typical ESR-STM experiments. Previous works have shown that the coherence of Ti spins on two monolayers of MgO deposited on Ag is lifetime limited such that $T_2 = 2T_1$, which allows us to discuss the first results without considering additional pure dephasing [6, 9, 17]. As can be seen in Fig. 6.4a the T_2 time of the two entangled spins (taken here to be identical) has a rather modest influence in the experimentally relevant range of $T_2 > 300$ ns. This is illustrated as well by Fig. 6.4b, which shows a slice at $T = 0.1$ K. Such low temperatures are typically achieved by using a dilution refrigerator equipped ESR-STM which can reach base-temperatures close to 20 mK[22, 23]. Clearly, in all cases a T_2 of around 300 ns allows for efficient entanglement detection. Temperature is a more critical parameter since the system is initialized purely by temperature. Temperatures that are high compared to the energy splitting of the eigenstates cause excited energy states to be populated. The effect of this is twofold: i) the system is not fully initialized to the ground state which reduces $\mathscr{C}$ and $\mathscr{W}_R$. ii) parts of the population that are in excited states additionally reduce $\mathscr{C}$, but do not participate in $\mathscr{W}_R$. Though this effect is in general small at elevated temperatures it is non-negligible. This becomes apparent in Fig. 6.4c where we show another slice of Fig. 6.4a but now for $T_2 = 300$ ns. Above 300 mK the concurrence as well as $\mathscr{W}_R$ drastically drop and the concurrences reaches 0 at 700 mK. At the same time, $\mathscr{W}_R$ seems to have a non-zero value, indicating entanglement in a not-entangled system. For $\mathscr{W}_R$ to stay an appropriate witness of entanglement we need to subtract an offset with upper bound $O = \sqrt{p_{\uparrow\uparrow} p_{\downarrow\uparrow}}$ where p are the eigenstate populations in thermal equilibrium (see supplementary information IV). The offset can be calculated straightforwardly from the initial populations and is defined such that $\mathscr{W}_R - O$ cannot be negative, resulting in a reliable witness of entanglement for all temperatures. This is why for all simulations, including Fig. 6.4a and b we report $\mathscr{W}_R - O$.

The same physical principles apply to all systems purely initialized by temperature. To avoid these limitations, alternative systems where the initialization is achieved by e.g. pumping and independent of system temperature should be used.

We now investigate the relation between $\mathscr{C}$ and $\mathscr{W}_R - O$ in Fig. 6.4d where we plot $\mathscr{W}_R - O$ against $\mathscr{C}$ for T sweeps at various T_2. The underlying relation is linear as in the ideal zero temperature limit(see supplementary information I, III and V). The solid lines in Fig. 6.4d are the linear dependencies that best match the data (details are in Table 6.1). The dashed line is the analytic solution in the limit of infinite T_2 (see supplementary information III). Finally, in Fig. 6.4e we plot $\mathscr{W}_R - O$ against $\mathscr{C}$ for T_2 sweeps at various temperatures. We see here that the dependence can best be fitted with a logarithmic scaled power law, which reflects that for lower T_2 there is more decay of the read-out than of the concurrence (see supplementary information II and V). Solid lines in Fig. 6.4e represent fits of the form $\mathscr{W}_R - O = \frac{\mathscr{C}^2}{2a\ln\mathscr{C}}(\mathscr{C}^a - 1)$ (details are in Table 6.2). The dashed line is the analytic solution in the limit of zero T (see supplementary information II). Deviations from the fits can be attributed to missing terms in O (see supplementary information IV), additional remaining cross-talk in the driving pulse scheme and exchange mixing terms between spin eigenstates causing a more complicated relation between driving strengths and Rabi times.
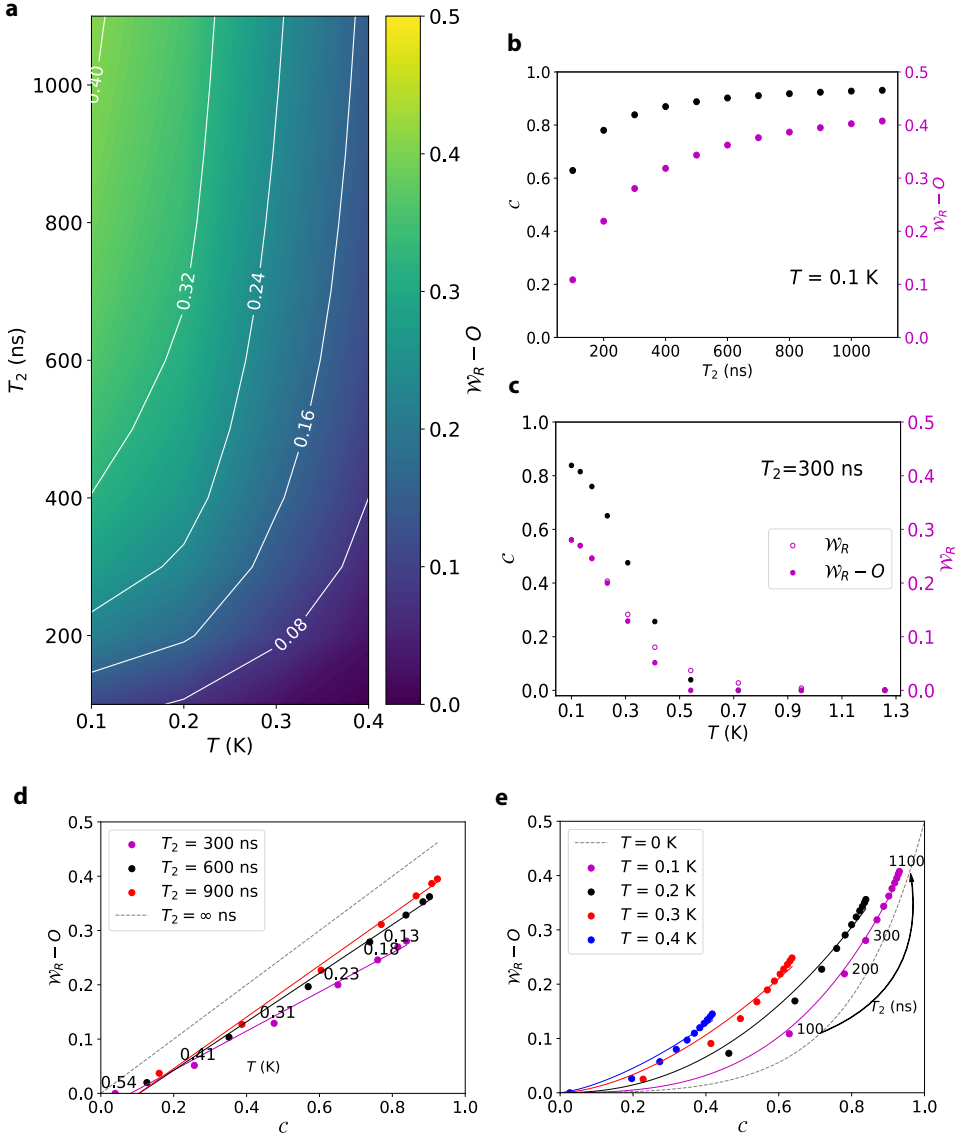
Figure 6.4: Influence of finite lifetime and temperature on the entanglement. (a) shows $\mathcal{W}_R - O$ as function of temperature and decoherence time T_2 (where $T_2 = 2 \cdot T_1$) **(b)** slice of (a) showing $\mathcal{W}_R - O$ together with the concurrence $\mathcal{C}$ for $T = 0.1$ K as achievable by dilution refrigerators. **(c)** slice of (a) showing $\mathcal{W}_R - O$ together with $\mathcal{C}$ for $T_2 = 300$ ns. Clearly, temperature is a critical factor and the concurrence drops drastically above 0.3 K. We also plot $\mathcal{W}_R$ such that the difference of subtracting O becomes apparent. **(d)** relation of $\mathcal{C}$ and $\mathcal{W}_R - O$ for three different T_2. Solid lines are linear fits. The dashed line represents the analytical limit for $T_2 \to \infty$ **(e)** relation of $\mathcal{C}$ and $\mathcal{W}_R - O$ for four different temperatures. Solid lines are logarithmic weighted power law fits. The dashed line represents the analytical limit for $T \to 0$. The system parameters are as shown in Fig. 6.2a

Finally, we address the influence of noise on the entanglement detection. First, we consider the influence of quantum noise causing pure dephasing, such that the coherence time is no longer lifetime limited but reduced by additional processes leading to an effective coherence time of $1/T_2^* = 1/T_2 + 1/T_\phi$. T_ϕ is the time constant of the pure dephasing process. In the following, $T_2 = 2T_1 = 300$ ns as typical for the experiments.[9] As show in Fig. 6.5a and b even fast dephasing processes with a dephasing time around $T_2^* = 75$ ns still allow for sufficient concurrence and $\mathscr{W}_R - O$. It is not surprising that longer T_2^* times are desirable as this is generally the case in quantum coherent systems, but it is encouraging that in the typical experimental range of $T_2^* \approx 300$ ns [6, 9, 17] concurrence and $\mathscr{W}_R - O$ are still relatively high. Second, we consider the influence of classical noise. Experiments have indicated that despite the excellent mechanical stability of STM systems, slow variation of the tip height can occur during the measurement. In our setup, such a variation would change the local magnetic field of the sensor and thereby the resonance frequency f_0 of the sensor.[6, 24] We employ a simple noise model by imposing a Gaussian distribution ($\mu = f_0, \sigma = 30$ MHz) on the sensor and perform 100 calculations. We analyzed the resulting variation of $\mathscr{W}_R - O$ shown in Fig. 6.5c for three representative cases: The best case scenario ($T = 0.01$K, $T_2 = \infty$ for the target spins) gives the highest contrast and detection should be easy and reliable. In the intermediate case ($T = 0.1$K, $T_2 = 300$ ns) $\mathscr{W}_R - O$ is narrowly peaked around 0.28, which should still give a very reliable readout. In the case of high temperature and short T_2 ($T = 0.4$K, $T_2 = 300$ ns) $\mathscr{W}_R - O$ is small (≈ 0.045), it is, however, still very narrowly distributed which indicates that with appropriate care in the measurement this could still be measurable.

6.5. CONCLUSION

In this work we have shown by open quantum systems simulations that two exchange coupled and relatively long-lived spins can be entangled and that the entanglement can be directly measured by ESR-STM using a third, weakly coupled sensor spin. Our simulations indicate that temperature is critical to achieve high degree of entanglement and $\mathscr{W}_R$, due to the fact that the populations are initialized into thermal equilibrium. Systems that can be initialized more independently from temperature as usually done in optical qubits in trapped ion systems for example, could overcome the strict temperature requirement. For physical spins on surface systems available today, such as the widely studied Ti on MgO/Ag(001), entanglement should be achievable and in principle measurable with $T_2 = 300$ ns for the quantum spins and $T_1 \approx 20$ ns for the sensor spin at temperatures up to 400 mK. High degrees of entanglement $\mathscr{C} \approx 0.8$ and corresponding read-out can be reached when using a dilution refrigerator at $T \approx 100$ mK.

6.6. SIMULATION DETAILS

6.6.1. SYSTEM HAMILTONIAN

All calculations were performed using a converged time step depending on the pulse scheme but such that it was always smaller than 8 ps. Following previous works,[6] we modeled each spin as an on-site energy term $2\pi f_{L,i} S_{z,i}$ with $f_{L,i}$ the i-th Larmor frequency, and pairwise isotropic exchange coupling terms $J_{i,j} \boldsymbol{S}_i \cdot \boldsymbol{S}_j$. ESR driving is achieved by applying the necessary single frequency driving terms $\Omega_k \cos(\omega_k(t - t_k^{\text{start}}) + \phi_k)\sigma_{x,i}(t_k^{\text{start}} <$
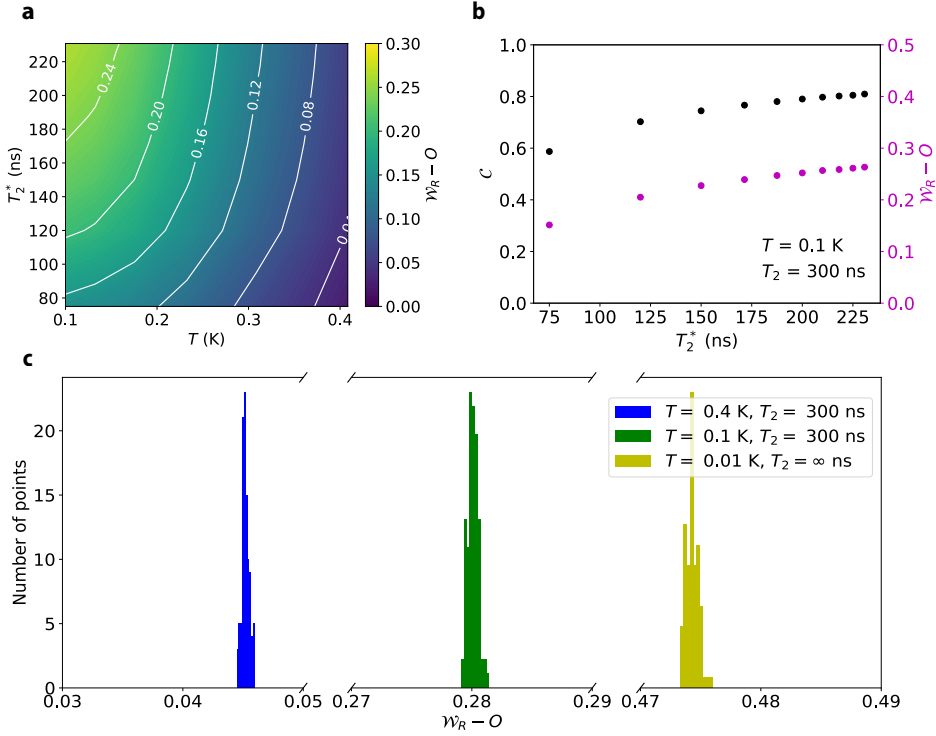
Figure 6.5: Influence of noise on the entanglement. (a) shows the achievable concurrence and $\mathcal{W}_R - O$ as function of pure dephasing time T_ϕ. (b) shows $\mathcal{C}$ and $\mathcal{W}_R - O$ as function of T_2 for a fixed $T_2 = 300$ ns for the two spins and $T = 0.1$ K. (c) achievable readout contrast $\mathcal{W}_R - O$ as function of Gaussian magnetic field noise causing fluctuations of the resonance frequency of the sensor spin with $\sigma = 30$ MHz for three representative cases characterized by T and T_2.

$t < t_k^{\text{end}}$), with ω_k the frequency the pulse is send at matching the desired energy transition, t_k^{start} and t_k^{end} the start and end times of the pulse and ϕ_k is an adjustable phase. Ω_k is the on-resonance Rabi rate, $k = 1 \dots N$ the index of driving frequency terms. The maximum number of driving terms in our simulation was $N \leq 7$. The total system Hamiltonian can be written as follows:

$$H_{tot} = \sum_{i=1}^{3} 2\pi f_{L,i} S_{z,i} + \sum_{i=1}^{3} \sum_{j>i}^{3} J_{i,j} \boldsymbol{S}_i \cdot \boldsymbol{S}_j + \sum_{k} \sum_{i=1}^{3} \Omega_k \cos\left(\omega_k(t - t_k^{\text{start}}) + \phi_k\right) \sigma_{x,i} (t_k^{\text{start}} < t < t_k^{\text{end}})$$

$$(6.1)$$

6.6.2. LINDBLAD EQUATION

We solved a Lindblad equation for the reduced density matrix ρ of the following form

$$\frac{d\rho}{dt} = -\frac{i}{\hbar}[H_{\text{tot}}, \rho] + \sum_l \left(\mathscr{L}_l \rho \mathscr{L}_l^\dagger - \frac{1}{2} \mathscr{L}_l^\dagger \mathscr{L}_l \rho - \frac{1}{2} \rho \mathscr{L}_l^\dagger \mathscr{L}_l \right) \tag{6.2}$$

The last term on the right hand side are the collapse operators for our system. We used two sets of collapse operators $\mathscr{L}^{\text{Kondo}} + \mathscr{L}^\phi$ to model spin energy relaxation as well as pure dephasing.

6.6.3. COLLAPSE OPERATORS

The first set of collapse operators was defined acting on the coupled 3 spin system in order to model Kondo spin relaxation, known to be the main source of decoherence for these system [4, 25, 26]. We arrive at these terms by writing the known rate equation (see for example Eq. 4 of supplementary of [27]) in Lindblad form. The operator acting between energy level m and n of the system is

$$\mathscr{L}^{\text{Kondo}}_{m,n} = \sqrt{\sum_l |J_l \sum_{s_i, s_f} \langle m, s_i | \boldsymbol{s} \otimes \boldsymbol{S_l} | n, s_f \rangle |^2 \frac{\epsilon_{mn}}{e^{\epsilon_{mn}/k_B T} - 1}} \, |m\rangle \langle n| . \tag{6.3}$$

Here the first sum is over the l different atomic spins and the second sum is over the initial (s_i) and final (s_f) state of the itinerant electron spin interacting with these spins. $\boldsymbol{S}$ and $\boldsymbol{s}$ are the respective spin operators. ϵ_{mn} is the energy difference between m and n of the three-spin system. Finally, J_l is the strength of the interaction with each atomic spin. In low temperature approximation it relates to the isolated l-th spin relaxation time $T_{1,l}$ and energy of its Larmor frequency ϵ_l as (see Eq. 69 of [26])

$$J_l = \sqrt{\frac{1}{\epsilon_l T_{1,l}}} . \tag{6.4}$$

The second set of operators is for pure dephasing. Here, the standard operators are used relating the pure dephasing rate to the pure dephasing time $T_{\phi,l}$ via the Pauli-z matrix for the l-th spin, i.e. $\sigma_{z,l} = \mathbb{1} \otimes_1 \mathbb{1} \ldots \mathbb{1} \otimes_l \sigma_z \otimes_{l+1} \mathbb{1} \ldots$

$$\mathscr{L}^\phi_l = \sqrt{\frac{1}{2 T_{\phi,l}}} \sigma_{z,l} . \tag{6.5}$$

6.6.4. READ OUT

For read-out long pulses were sent resonant with transitions of S_R. The expectation value of S_R was averaged in 16000 time steps for a time of 100 ns. In order to have a converged expectation value a Rabi strength was used double the other strengths used in the scheme.

T_2 (ns)	a	b
300	0.36 ± 0.03	-0.03 ± 0.02
600	0.44 ± 0.02	-0.05 ± 0.02
900	0.47 ± 0.02	-0.05 ± 0.02

Table 6.1: Fitting results of $\mathscr{W}_R - O = a + b\mathscr{C}$, for the data shown in Fig. 6.4e. Uncertainties represent the 2σ confidence interval

T (K)	a
0.1	2.43 ± 0.23
0.2	0.43 ± 0.24
0.3	-0.60 ± 0.15
0.4	-0.90 ± 0.10

Table 6.2: Fitting results of $\mathscr{W}_R - O = \frac{\mathscr{C}^2}{2a\ln\mathscr{C}}(\mathscr{C}^a - 1)$, for the data shown in Fig. 6.4e. Uncertainties represent the 2σ confidence interval

6.6.5. FITTING RESULTS
The relations between $\mathscr{W}_R - O$ and $\mathscr{C}$ in Fig. 6.4d were fit using $\mathscr{W}_R - O = a + b\mathscr{C}$ reflecting the up to first order linear dependence as derived in supplementary information III and IV. The fitting results are reported in Table 6.1. The relations between $\mathscr{W}_R$ and $\mathscr{C}$ in Fig. 6.4e were best fit using a logarithmic weighted power law function of the form $\mathscr{W}_R - O = \frac{\mathscr{C}^2}{2a\ln\mathscr{C}}(\mathscr{C}^a - 1)$. The fitting results are reported in Table 6.2. Derivations are in supplementary information II and IV.

6.6.6. CONCURRENCE
For concurrence calculation first the partial trace over S_R was taken leaving the reduced matrix in the target spin basis. Then for each entanglement scheme the maximum was reported.

6.7. CODE AND DATA AVAILABILITY
The underlying code for this study is available and can be accessed via Ref. [28]. All data generated or analyzed during this study are included in Ref. [29].

6.8. ACKNOWLEDGMENTS
The authors thank N. Lorente for his insight related to entanglement in surface spin systems. Further we thank G. Giedke, F. Donati and H. Stemp for discussions.

6.9. AUTHOR CONTRIBUTIONS
RB, SP, and CW conceived the paper, RB and CL performed numerical simulations, all authors contributed to the discussion and the writing of the manuscript.

6.10. APPENDIX
6.10.1. DERIVATION OF THE RELATION BETWEEN $\mathscr{W}_R$ AND $\mathscr{C}$
In this section we derive the analytical relation between readout contrast $\mathscr{W}_R$ and the concurrence $\mathscr{C}$ by starting from a general description of the entangled state.

DERIVATION OF $\mathscr{C}$ FOR EVERY POSSIBLE ENTANGLED STATE

Every state in the entanglement subspace can be written as:

$$\psi_{\text{ent}} = \alpha |\uparrow\downarrow\rangle + \sqrt{1-\alpha^2} |\downarrow\uparrow\rangle, \tag{6.6}$$

with $0 \le \alpha \le 1$. The corresponding density matrix is:

$$\rho_{\text{ent}} = \alpha^2 |\uparrow\downarrow\rangle\langle\uparrow\downarrow| + (1-\alpha^2)|\downarrow\uparrow\rangle\langle\downarrow\uparrow| + \alpha\sqrt{1-\alpha^2}(|\downarrow\uparrow\rangle\langle\uparrow\downarrow| + |\uparrow\downarrow\rangle\langle\downarrow\uparrow|) \tag{6.7}$$

Taking the partial trace we find the reduced density matrix is

$$\rho_1 = \alpha^2 |\uparrow\rangle\langle\downarrow| + (1-\alpha^2)|\downarrow\rangle\langle\downarrow| \tag{6.8}$$

Inserting this in the definition of the concurrence gives:

$$\mathscr{C} \equiv \sqrt{2[1-Tr(\rho_1^2)]} \tag{6.9}$$

$$= \sqrt{2[1-(\alpha^4 + (1-\alpha^2)^2]} \tag{6.10}$$

$$= \sqrt{-4\alpha^4 + 4\alpha^2} \tag{6.11}$$

$$= 2\alpha\sqrt{1-\alpha^2} \tag{6.12}$$

6

DERIVATION OF $\mathscr{W}_R$ FOR EVERY POSSIBLE ENTANGLED STATE

$\mathscr{W}_R$ is equal to the radius of the Bloch sphere corresponding to the state in the subspace. It can be expressed as

$$\mathscr{W}_R = 0.5\sin(\phi), \tag{6.13}$$

with ϕ the polar angle $[0, \pi]$.

This phase can be expressed in terms of the z-coordinate on the Bloch sphere as

$$\phi = \arccos(z/0.5), \tag{6.14}$$

which in turn be expressed in terms of α of the state in the entanglement basis as

$$z = 0.5(\alpha^2 - (1-\alpha^2)). \tag{6.15}$$

Here, α^2 is the probability to be in $|\uparrow\downarrow\rangle$. Substituting both in the expression of $\mathscr{W}_R$ yields:

$$\mathscr{W}_R = 0.5\sin(\arccos(2\alpha^2 - 1))) \tag{6.16}$$

$$= \sqrt{\alpha^2 - \alpha^4}, \tag{6.17}$$

where for the last equality we used the fact that $\sin(\arccos(x)) = \sqrt{1-x^2}$.

CONCLUSION

Looking at both results we can conclude that in the ideal case: $\mathscr{W}_R = 0.5\mathscr{C}$.

6.10.2. $\mathscr{W}_R(\mathscr{C})$ WITH T_1 DECAY

From the time stamp that maximum concurrence is reached until the read-out pulse $\mathscr{W}_R$ is already decaying with respect to the ideal $0.5\mathscr{C}$. Since $\mathscr{W}_R$ is the phase in the entanglement subspace the decay goes with $T_2 = 2T_1$ as $e^{-\frac{t_{\text{tot}}}{2T_1}}$ where t_{tot} is the total time between maximum entanglement and readout.

During the read-out time (t_{meas}) the excited-state of oscillation decays with $e^{-\frac{t_{\text{meas}}}{T_1}}$ whilst the ground state stays the same. Given that $\mathscr{W}_R$ is averaged over t_{meas} this leads to:

$$\mathscr{W}_R = \frac{C}{2t_{\text{meas}}} e^{-\frac{t_{\text{tot}}}{2T_1}} \int_0^{t_{\text{meas}}} dt \, e^{-\frac{t}{T_1}} \tag{6.18}$$

$$= \frac{\mathscr{C} T_1}{2t_{\text{meas}}} e^{-\frac{t_{\text{tot}}}{2T_1}} (1 - e^{-\frac{t_{\text{meas}}}{T_1}}) \tag{6.19}$$

In other words, one can find $\mathscr{W}_R(\mathscr{C})$ from $\mathscr{C}(T_1)$.

DERIVATION OF THE RELATION BETWEEN T_1 AND $\mathscr{C}$

Setting T_1 the same for both target spins the density matrix after the Hadamard time (t_{H}) is:

$$\rho_{\text{H}} = \begin{pmatrix} \frac{1}{2} + \frac{1}{2}(1 - e^{-\frac{t_{\text{H}}}{T_1}}) & \frac{1}{2}e^{-\frac{t_{\text{H}}}{T_2}} \\ \frac{1}{2}e^{-\frac{t_{\text{H}}}{T_2}} & \frac{1}{2}e^{-\frac{t_{\text{H}}}{T_1}} \end{pmatrix} \tag{6.20}$$

which is a general density matrix with additional relaxation to the ground state and dephasing. Next we can evaluate the density matrix after the CNOT time (t_{CNOT}):

$$\begin{pmatrix} 1 - e^{-\frac{t_{\text{CNOT}}}{T_1}} & 0 & 0 & 0 \\ 0 & \frac{1}{2}e^{-\frac{t_{\text{tot}}}{T_1}} & \frac{1}{2}e^{-\frac{t_{\text{tot}}}{T_2}} & 0 \\ 0 & \frac{1}{2}e^{-\frac{t_{\text{tot}}}{T_2}} & (\frac{1}{2} + \frac{1}{2}(1 - e^{-\frac{t_{\text{H}}}{T_1}}))e^{-\frac{t_{\text{CNOT}}}{T_1}} & 0 \\ 0 & 0 & 0 & 0 \end{pmatrix} \tag{6.21}$$

It is the effect of the CNOT with additional relaxation and dephasing. The total time t_{tot} is here equal to $t_{\text{H}} + t_{\text{CNOT}}$. The final state can be recognised as a ensemble of the ground state with population $1 - e^{-\frac{t_{\text{CNOT}}}{T_1}}$ plus a pure state with phase $\frac{1}{2}e^{-\frac{t_{\text{tot}}}{T_2}}$ and population $e^{-\frac{t_{\text{CNOT}}}{T_1}}$.

We can extract the concurrence from the fact that energy eigenstates have 0 contribution to the concurrence and for a pure state the concurrence is equal to 2 times the phase in the entanglement subspace. With that,

$$\mathscr{C} = (1 - e^{-\frac{t_{\text{CNOT}}}{T_1}}) \times 0 + e^{-\frac{t_{\text{tot}}}{T_2}} \tag{6.22}$$

From which follows:

$$-\frac{1}{T_1} = \frac{2}{t_{\text{tot}}} \ln(\mathscr{C}), \tag{6.23}$$

where we have used that $T_2 = 2T_1$.

CONCLUSION

Substituting in Eq. 6.19 we arrive at:

$$\mathcal{W}_R = \frac{\mathscr{C}^2}{2a\ln\mathscr{C}}(\mathscr{C}^a - 1),\tag{6.24}$$

where we redefined the constant as $a = 2\frac{T_{\text{meas}}}{t_{\text{tot}}}$.

6.10.3. EFFECT OF FINITE TEMPERATURE ON $\mathcal{W}_R(\mathscr{C})$

$\mathscr{C}(T)$

As a result of finite temperature the system is not fully initialized in the $|\uparrow\uparrow\uparrow\rangle$ population from the start. In the following we assume in all cases that the temperature is low enough so that only single spin excitations are populated at any temperature. This agrees with the results of our simulations. In that case the only non-zero populations are $p_{\uparrow\uparrow\uparrow}$, $p_{\downarrow\uparrow\uparrow}$, $p_{\uparrow\downarrow\uparrow}$ and $p_{\uparrow\uparrow\downarrow}$.

After the Hadamard pulse the density matrix in the reduced single spin space is

$$\rho_{\text{H}} = \begin{pmatrix} \frac{p_{\uparrow\uparrow\uparrow}+p_{\uparrow\downarrow\uparrow}}{2} & \frac{p_{\uparrow\uparrow\uparrow}-p_{\uparrow\downarrow\uparrow}}{2} \\ \frac{p_{\uparrow\uparrow\uparrow}-p_{\uparrow\downarrow\uparrow}}{2} & \frac{p_{\uparrow\uparrow\uparrow}+p_{\uparrow\downarrow\uparrow}}{2} \end{pmatrix}\tag{6.25}$$

This can be understood as the density matrix of H applied to $\uparrow\uparrow\uparrow$ plus the density matrix of H applied to $\uparrow\downarrow\uparrow$ (which have opposite phases).

Notice that as a result the total phase is the *difference* between the two populations and thus decreases with higher temperature.

Next, it can be found that after the CNOT the reduced density matrix of the target spins is

$$\begin{pmatrix} p_{\uparrow\uparrow\downarrow} & 0 & 0 & 0 \\ 0 & \frac{p_{\uparrow\uparrow\uparrow}+p_{\uparrow\downarrow\uparrow}}{2} & \frac{p_{\uparrow\uparrow\uparrow}-p_{\uparrow\downarrow\uparrow}}{2} & 0 \\ 0 & \frac{p_{\uparrow\uparrow\uparrow}-p_{\uparrow\downarrow\uparrow}}{2} & \frac{p_{\uparrow\uparrow\uparrow}+p_{\uparrow\downarrow\uparrow}}{2} & 0 \\ 0 & 0 & 0 & p_{\downarrow\uparrow\uparrow} \end{pmatrix}\tag{6.26}$$
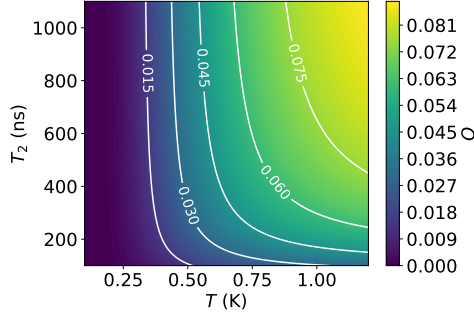
of which the total concurrence can be evaluated to be

$$\mathscr{C} = \max(p_{\uparrow\uparrow\uparrow} - p_{\uparrow\downarrow\uparrow} - 2\sqrt{p_{\uparrow\uparrow\downarrow}p_{\downarrow\uparrow\uparrow}}, 0).\tag{6.27}$$

Using the Boltzmann probability we can finally express the concurrence in terms of temperature:

$$\mathscr{C} = \max(\frac{1 - e^{-\frac{\epsilon_{\uparrow\downarrow\uparrow}}{k_B T}}}{Z} - 2\sqrt{\frac{e^{-\frac{\epsilon_{\uparrow\uparrow\downarrow}+\downarrow\uparrow\uparrow}}{k_B T}}{Z}}, 0)\tag{6.28}$$

with Z the total partition function of the 4 non-zero populations.

Figure 6.6: Readout contrast offset. Offset O of the readout contrast as a function of T_2 and T for $t_{\text{Rabi}} = 25$ ns and $t_{\text{meas}} = 100$ ns

DERIVING $\mathcal{W}_R(\mathcal{C})$

Like in the ideal case (Section I) the read-out is equal to the radius of the Bloch sphere in the singlet-triplet subspace $\mathcal{W}_R = 0.5(p_{\uparrow\uparrow\uparrow} - p_{\uparrow\downarrow\uparrow})$. However, now, due to the finite temperature, $\mathcal{C}$ has an additional term leading to an effective offset O in the relation between $\mathcal{W}_R$ and $\mathcal{C}$.

$$\mathcal{W}_R = \frac{\mathcal{C}}{2} + \sqrt{p_{\uparrow\uparrow\downarrow} p_{\downarrow\uparrow\uparrow}}. \tag{6.29}$$

Showing that we should expect an up to first order linear behavior of $\mathcal{W}_R(C)$ as a result of temperature

6.10.4. EXPLANATION OF OFFSET IN FIGURE 4C

Combining Eq. 6.19 and Eq. 6.29 we can find that given a relaxation T_1 of the target spins the total expression for $\mathcal{W}_R$ as function of T is

$$\mathcal{W}_R = \frac{(\mathcal{C} + 2\sqrt{p_{\uparrow\uparrow\downarrow} p_{\downarrow\uparrow\uparrow}}) T_1}{2 t_{\text{meas}}} e^{-\frac{t_{\text{tot}}}{2T_1}} (1 - e^{-\frac{t_{\text{meas}}}{T_1}}). \tag{6.30}$$

meaning that the offset of $\mathcal{W}_R$ is

$$O = \frac{T_1 \sqrt{p_{\uparrow\uparrow\downarrow} p_{\downarrow\uparrow\uparrow}}}{t_{\text{meas}}} e^{-\frac{5 t_{\text{Rabi}}}{8 T_1}} (1 - e^{-\frac{t_{\text{meas}}}{T_1}}), \tag{6.31}$$

where is used that $t_{\text{tot}} = \frac{5}{4} t_{\text{Rabi}}$. Since $\mathcal{C}$ cannot be negative the same holds for $\mathcal{W}_R - O$ and thus the appropriate offset corrected read-out is $\max(\mathcal{W}_R - O, 0)$

From figure 6.6 evaluated for a Rabi strength of 0.04 Ghz and a measurement time of 100 ns, it is clear that the offset is in general small compared to $\mathcal{W}_R$ and mostly T-dependent. The terms that are not T-dependent further reduce O hence $O = \sqrt{p_{\uparrow\uparrow\downarrow} p_{\downarrow\uparrow\uparrow}}$ is a good upper bound to use.

6.10.5. EXPLANATION OF THE FITS IN FIGURES 4D AND 4E

We combine all previous results in a fit function for figures 4D and 4E. For figure 4E we combine Eq. 6.24, Eq. 6.29 and Eq. 6.31 into

$$\mathscr{W}_R - O = \frac{\mathscr{C}^2}{2a\ln\mathscr{C}}(\mathscr{C}^a - 1). \tag{6.32}$$

where the temperature dependence is part of C and the rest of the function captures the T_1 dependence.

For figure 4D we combine Eq. 6.19, Eq. 6.29 and Eq. 6.31 into

$$\mathscr{W}_R - O = a + b\mathscr{C} \tag{6.33}$$

Here a is based on the equations not strictly necessary but used to make the fits converge. It can account for sources of error left outside the scope of this derivation like undesired off-resonance driving of energy transitions.

6.10.6. ALTERNATIVE CHOICES FOR B-CYCLE
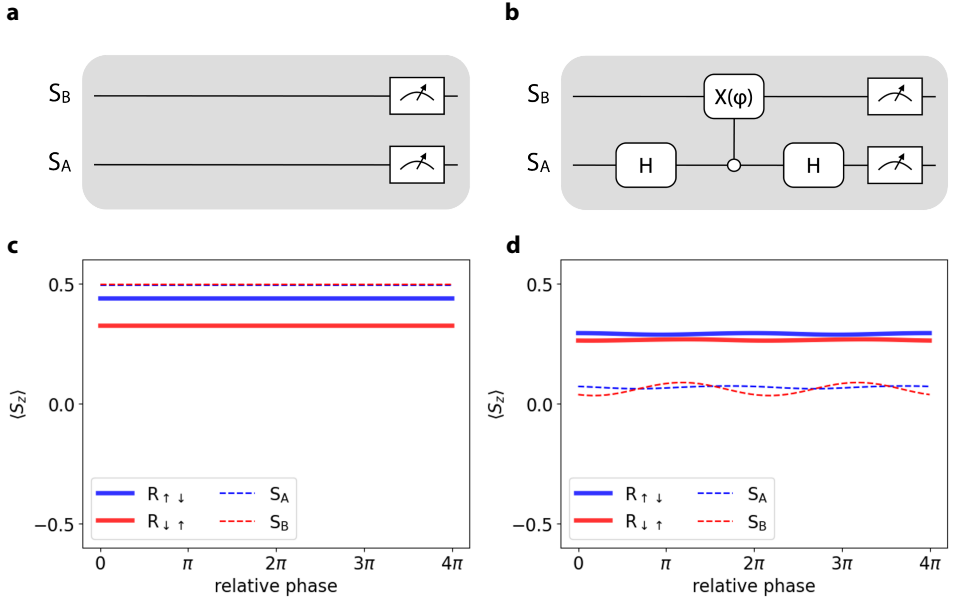
Figure 6.7: alternative choices of B-cycle. **(a)** and **(b)** show alternative pulse schemes for the B-cycle of the measurement. **(a)** does not contain any gate sequences whilst **(b)** performs some superposition (but not entanglement). The variation of the respective expectation values of $\langle S_z \rangle$ as well as the signal obtained from the sensor spin are shown in panels **(c)** and **(d)**

As discussed in the main text the choice of the empty cycle ("B-cycle") is often take such that it removes all background signal in the ESR-STM experiment. As such, the choice is not unique and as long as the background can be reliably extracted any B-cycle choice is equivalent. In Fig. 6.7, we show that alternative B-cycles used in the experimental reference by Yu Wang and coworkers can be also implemented in our protocol. For details of the experiment please refer to the supplement of Ref. [9]. We emphasize that the

readout of the ESR current in the STM gives the difference of signals in the two cycles. In all cases shown here the B-cycle leads to a reliable removal of the (flat) signal background and any B-cycle choice is valid.

References

[1] Crommie, M. F., Lutz, C. P. & Eigler, D. M. Confinement of electrons to quantum corrals on a metal surface. *Science* **262**, 218–220 (1993).

[2] Yang, K. *et al.* Engineering the eigenstates of coupled spin-1/2 atoms on a surface. *Physical Review Letters* **119**, 227206 (2017).

[3] Baumann, S. *et al.* Electron paramagnetic resonance of individual atoms on a surface. *Science* **350**, 417–420 (2015).

[4] Yang, K. *et al.* Coherent spin manipulation of individual atoms on a surface. *Science* **366**, 509–512 (2019).

[5] Phark, S.-h. *et al.* Electric-field-driven spin resonance by on-surface exchange coupling to a single-atom magnet. *Advanced Science* **10**, 2302033 (2023).

[6] Phark, S.-h. *et al.* Double-resonance spectroscopy of coupled electron spins on a surface. *ACS nano* **17**, 14144–14151 (2023).

[7] Reina-Gálvez, J., Lorente, N., Delgado, F. & Arrachea, L. All-electric electron spin resonance studied by means of floquet quantum master equations. *Physical Review B* **104**, 245435 (2021).

[8] Reina-Gálvez, J., Wolf, C. & Lorente, N. Many-body nonequilibrium effects in all-electric electron spin resonance. *Physical Review B* **107**, 235404 (2023).

[9] Wang, Y. *et al.* An atomic-scale multi-qubit platform. *Science* **382**, 87–92 (2023).

[10] Rieffel, E. G. & Polak, W. H. *Quantum computing: A gentle introduction* (MIT press, 2011).

[11] Bastiaans, K. *et al.* Amplifier for scanning tunneling microscopy at mhz frequencies. *Review of Scientific Instruments* **89** (2018).

[12] Willke, P. *et al.* Coherent spin control of single molecules on a surface. *ACS nano* **15**, 17959–17965 (2021).

[13] Del Castillo, Y. & Fernández-Rossier, J. Certifying entanglement of spins on surfaces using esr-stm. *Physical Review B* **108**, 115413 (2023).

[14] Veldman, L. M. *et al.* Free coherent evolution of a coupled atomic spin system initialized by electron scattering. *Science* **372**, 964–968 (2021).

[15] Wei, K. X. *et al.* Verifying multipartite entangled greenberger-horne-zeilinger states via multiple quantum coherences. *Physical Review A* **101**, 032343 (2020).

6

[16] Stemp, H. G. *et al.* Tomography of entangling two-qubit logic operations in exchange-coupled donor electron spin qubits. *Nature Communications* **15**, 8415 (2024).

[17] Wang, Y. *et al.* Universal quantum control of an atomic spin qubit on a surface. *npj Quantum Information* **9**, 48 (2023).

[18] Johansson, J. R., Nation, P. D. & Nori, F. Qutip: An open-source python framework for the dynamics of open quantum systems. *Computer Physics Communications* **183**, 1760–1772 (2012).

[19] Hill, S. A. & Wootters, W. K. Entanglement of a pair of quantum bits. *Physical review letters* **78**, 5022 (1997).

[20] Reale, S. *et al.* Electrically driven spin resonance of 4 f electrons in a single atom on a surface. *Nature Communications* **15**, 5289 (2024).

[21] Seifert, T. S. *et al.* Single-atom electron paramagnetic resonance in a scanning tunneling microscope driven by a radio-frequency antenna at 4 k. *Physical Review Research* **2**, 013032 (2020).

[22] Kim, J. *et al.* Spin resonance amplitude and frequency of a single atom on a surface in a vector magnetic field. *Physical Review B* **104**, 174408 (2021).

[23] van Weerdenburg, W. M. *et al.* A scanning tunneling microscope capable of electron spin resonance and pump–probe spectroscopy at mk temperature and in vector magnetic field. *Review of Scientific Instruments* **92** (2021).

[24] Willke, P. *et al.* Probing quantum coherence in single-atom electron spin resonance. *Science Advances* **4**, eaaq1543 (2018).

[25] Ternes, M. Spin excitations and correlations in scanning tunneling spectroscopy. *New Journal of Physics* **17**, 063016 (2015).

[26] Delgado, F. & Fernández-Rossier, J. Spin decoherence of magnetic atoms on surfaces. *Progress in Surface Science* **92**, 40–82 (2017).

[27] Loth, S., Lutz, C. P. & Heinrich, A. J. Spin-polarized spin excitation spectroscopy. *New Journal of Physics* **12**, 125021 (2010).

[28] Broekhoven, R., Wolf, C. & Lee, C. Module to model pulsed esr in stm experiments (2024).

[29] Broekhoven, R., Lee, C., Phark, S.-h., Otte, S. & Wolf, C. Protocol for certifying entanglement in surface spin systems using a scanning tunneling microscope (2024).

7

CONCLUSION AND OUTLOOK

7.1. Conclusion

We have presented three models for atomic systems on a metal surface and have shown that understanding the surface is essential to understand the systems and their limitations.

For chains of magnetic atoms on a superconductor we have presented a model based on short junction theory to evaluate the YSR dispersion. We have shown that we can evaluate the effective Hamiltonian of the YSR chain from just the self-energy at the Fermi level. By comparing with exact calculation of a single orbital model we have proven that our model works and has a negligible remaining error. We proceeded with a model with atomistic spin-orbit coupling and managed to evaluate the Rashba split YSR dispersion. This dispersion consists of features of the corresponding metal Fermi surface that go beyond simple toy models proving that an orbital description is essential for modeling YSR dispersion.

For field emission resonances in chlorine vacancies on vacuum we have shown that there can be a negative differential resistance, which can be attributed to the specific shape of the Fermi surface of copper and its overlap with the FER wavefunction.

For coherent spins on a surface we have shown that we can initiate a coherent flip-flop operation between a titanium nucleus and nuclear spin when we tune the spins and initialize them through spin-pumping. We can probe this flip-flop as it is faster than the decoherence by the metal free electron spins. Our model of the decoherence is in agreement with that.

Next to this, we have presented a protocol, compatible with STMs at sufficiently low and preferably mK temperatures, to coherently entangle two remote titanium spins with each other and read out the entanglement through a sensorspin. We have shown through modeling that, given the decoherence of free electrons of the metal as well as decoherence from tip shaking, this protocol still works and allows to probe whether the two remote spins have been entangled.

7.2. Outlook

7.2.1. YSR chains

The presented short junction method is expected to be especially powerful when combined with density functional theory. One would then start with a atomic orbital based slab calculation on a geometry as represented by Fig. 7.1. From this result we can extract a unit cell at the surface of the metal and in the bulk of the metal. We can combine these in Eq. 2.22 to evaluate the corresponding Fermi Level self-energy and use this as input to the short junction method to evaluate the YSR dispersion. In this way we could study the gap closing and opening when we vary parameters and compare the results with previously performed density functional theory studies. We could proceed to study chains with different orientation on the surface to see what the influence of the orientation is.

7.2.2. FER

For field emission resonances the next step has already been made. After the work that has been presented here was completed, the higher order orbital wavefunctions of the FER were studied and two FER's were coupled with each other, which was shown to map
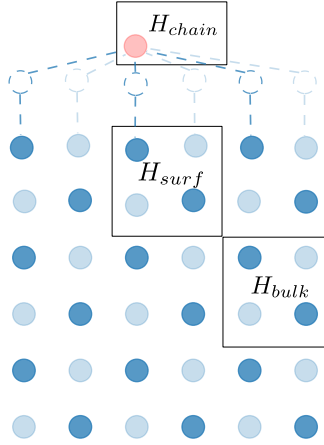
Figure 7.1: YSR DFT geometry. Geometry for the metal as could be used in DFT calculations of YSR dispersion with the bulk unitcell (H_{bulk}) and surface unitcell (H_{surf}) highlighted. The dotted circle represent the way to couple the metal through the chain (H_{chain}) through virtual leads.

well on a tight binding model.

7.2.3. COHERENT SPINS: DECOHERENCE IN EQUAL DISTANCE SPIN CHAINS

With spin flip-flop interactions experimentally confirmed between single spins on a surface [1] and between a nucleus spin and an electron spin, a natural follow-up question is whether we can exchange spins in a chain of spins and how the decoherence scales in these chains. Below we present some initial modeling results.

We start with an exchange-coupled spin-$\frac{1}{2}$ chain with all identical Larmor frequencies ω_{chain}, identical exchange coupling J_{chain} and identical Kondo coupling J_{Kondo} to the surface:

$$H_{chain} = \sum_{i=1}^{N} J_{chain} \boldsymbol{S}_i \cdot \boldsymbol{S}_{i+1} + \omega_{chain} \boldsymbol{S}_i, \tag{7.1}$$

$$H_{Kondo} = \sum_{i=1}^{N} J_{Kondo} \boldsymbol{S}_i \cdot \boldsymbol{\sigma}_i. \tag{7.2}$$

As explained in section 2.6.2, the decoherence rate γ can be divided into an inelastic contribution (γ_{inel}) and an elastic contribution(γ_{el}). These two contributions are independent of each other. γ_{inel} scales with the energy relaxation rate according to Eq. 2.51. γ_{el} is of the form of Eq. 2.52.

We evaluate the corresponding spin excitation values as a function of the time when we flip the first spin at time $t = 0$. The inset of Fig. 7.2a shows a schematic of a chain of 4 spins at a temperature of 0.4 K. The excitation will travel through the chain until it decoheres due to the spin scattering with the metal. As expected, the excitations travel

back and forth along the chain. However, we also see that the excitations increase in magnitude towards the end of the chain (purple spin). This is a result of the finite size, as the corresponding spin excitation modes have antinodes at the ends of the chain.
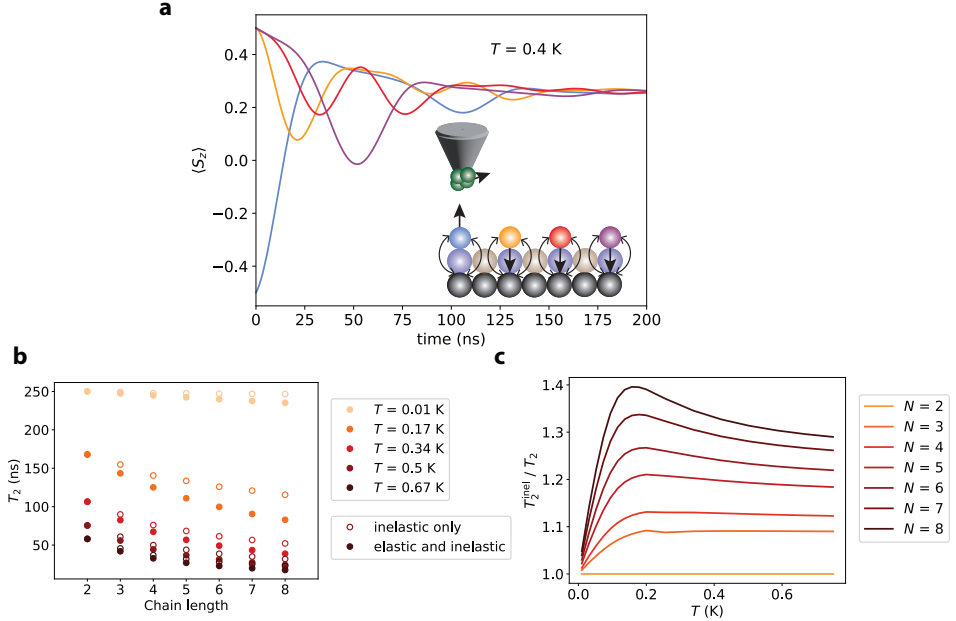
Figure 7.2: Decoherence times in equal distance spin chains. (a) Schematic of a spin chain with Kondo scattering with the surface. **(b)** Decoherence time plotted as a function of chain length for increasing temperatures. Solid dots include all decoherence channels. The unfilled dots are only for inelastic decoherence. Furthermore, $\rho J = 8 \times 10^{-3}$ and $B = 0.4$ T. **(c)** Ratio of inelastic decoherence time vs. total decoherence time for spin chains corresponding to Fig. **(b)**

We also track the total quantum coherent phase of the system with an exponential fit to extract the overall decoherence time T_2. We plot the result with solid dots for various temperatures in Fig. 7.2b as a function of the chain length. As the chains get longer, the decoherence times approach a minimum value for all temperatures. This is to be expected because, in the limit of long chains, the phase decoheres after a characteristic decoherence length, which, given a constant velocity at which the spin excitation is traveling, results in a characteristic decoherence time.

To get a better understanding of the decoherence, we also plot T_2^{inel} in Fig. 7.2b in unfilled dots. The elastic component does not exist for $N = 2$ independent of temperature. This ties in with the fact that two perfectly tuned spins form a clock transition [2]. For longer chains in the high- and low-temperature limits, T_2^{inel} coincides with T_2. In contrast, in the intermediate temperature range (≈ 0.2 K), the two decoherence times are further apart.

Though this means that in terms of decoherence time the elastic component is most significant in the (≈ 0.2 K) region, it does not mean that the elastic component is not

present at higher temperatures. This can be seen in Fig. 7.2c, where we plot the ratio T_2^{inel}/T_2 now as a function of temperature for each chain length. While it remains the case that the elastic component is the biggest at 0.2 K, it is still very much present at higher temperatures. Only in the low-temperature limit the elastic component becomes truly negligible. Still, it is remarkable that the plotted ratio does not scale monotonously when we increase the temperature. Instead, it increase towards a maximum around 0.2 K and then gradually decreases again towards the high-temperature limit. This can be attributed to the complex shapes of the decoherence rates in Eq. 2.49 and Eq. 2.52, but further research is required to understand this in more detail. We also note that the maximum gets more pronounced and shifts gradually to lower temperatures with increased chain length. Finally, in the high temperature limit, the ratio seems to show an even-odd effect as the values for increasing chain length are not evenly spaced.

Having an insight into the contribution of elastic decoherence is useful as, according to Eq. 2.52, it does not depend on the energy transitions of the system and thus can be seen as the minimum amount of decoherence that will always be present.

7.3. Code and data availability

All research data and code supporting the findings described in this chapter are available in 4TU.ResearchData at: DOI 10.4121/c773957e-b628-4962-817a-9a213bdf06db.

References

[1] Veldman, L. M. *et al.* Free coherent evolution of a coupled atomic spin system initialized by electron scattering. *Science* **372**, 964–968 (2021).

[2] Bae, Y. *et al.* Enhanced quantum coherence in exchange coupled spins via singlet-triplet transitions. *Science Advances* **4**, eaau4159 (2018).

7

LIST OF PUBLICATIONS

1. Lukas M. Veldman, Laetitia Farinacci, Rasa Rejali, **Rik Broekhoven**, Jeremie Gobeil, David Coffey, Markus Ternes, Sander Otte, *Free coherent evolution of a coupled atomic spin system initialized by electron scattering*, Science 372, 964–968(2021)

2. Rasa Rejali, Laetitia Farinacci, David Coffey, **Rik Broekhoven**, Jeremie Gobeil, Yaroslav M. Blanter, Sander Otte, *Confined vacuum resonances as artificial atoms with tunable lifetime*, ACS Nano, 16, 7(2022)

3. Lukas M. Veldman, Evert W. Stolte, Mark P. Canavan, **Rik Broekhoven**, Phillip Willke, Laetitia Farinacci, Sander Otte, *Coherent spin dynamics between electron and nucleus within a single atom*, Nature Communications, 15.1, 7951(2024)

4. **Rik Broekhoven**, Curie Lee, Soo-Hyon Phark, Sander Otte, Christoph Wolf, *Protocol for certifying entanglement in surface spin systems using a scanning tunneling microscope*, Npj Quantum Information, 10, 92(2024)

5. Evert W. Stolte, Jinwon Lee, Hester G. Vennema, **Rik Broekhoven**, Esther Teng, Allard J. Katan, Lukas M. Veldman, Philip Willke, Sander Otte, *Single-shot readout of the nuclear spin of an on-surface atom*, arXiv:2410.08704

6. **Rik Broekhoven**, Kostas Vilkelis, Artem Pulkin, Antonio Manesco, Anton Akhmerov *Short-junction theory for dispersion of a Yu-Shiba-Rusinov chain*, in preperation.